THESIS FOR THE DEGREE OF LICENTIATE OF ENGINEERING

Towards an Advanced Automotive Radar Front-end

Based on Gap Waveguide Technology

Qiannan Ren

Department of Electrical Engineering
Chalmers University of Technology
Gothenburg, Sweden, 2022

Towards an Advanced Automotive Radar Front-end
Based on Gap Waveguide Technology

Qiannan Ren

Department of Electrical Engineering
Chalmers University of Technology
SE-412 96 Gothenburg, Sweden
Phone: +46 (0)31 772 1000
www.chalmers.se

Printed by Chalmers Reproservice
Gothenburg, Sweden, September 2022

To my family

Abstract

This thesis presents the early works on dual circularly polarized array antenna based on gap waveguide, also microstrip-to-waveguide transitions for integration of automotive radar front-end. Being the most widely used radar antenna, PCB antenna suffers from dielectric loss and design flexibility. Next generation automotive radars demand sophisticated antenna systems with high efficiency, which makes waveguide antenna become a better candidate. Over the last few years, gap waveguide has shown advantages for implementation of complicated antenna systems. Ridge gap waveguides have been widely used in passive gap waveguide components design including slot arrays. In this regard, two transitions between ridge gap waveguides and microstrip lines are presented for the integration with gap waveguide antennas. The transitions are verified in both passive and active configuration. Another work on packaging techniques is presented for integration with inverted microstrip gap waveguide antennas.

Systems utilizing individual linear polarization (LP) that lack polarimetric capabilities are not capable of measuring the full scattering matrix, thus losing information about the scenery. To develop a more advanced radar system with better detectability, dual circularly polarized gap waveguide slot arrays for polarimetric radar sensing are investigated. An 8×8 planar array using double grooved circular waveguide polarizer is presented. The polarizers are compact in size and have excellent polarization properties. Multi-layer design of the array antenna benefits from the gap waveguide technology and features better performance.

The works presented in this thesis laid the foundation of future works regarding integration of the radar front end. More works on prototyping radar systems using gap waveguide technology will be presented in future publications.

Keywords: Integration, gap-waveguide, automotive, radar, antenna, packaging, MMIC, dual circular polarization, polarimetric radar.

List of Publications

This thesis is based on the following publications:

[A] **Qiannan Ren**, Ashraf Uz Zaman, Jian Yang, Vessen Vassilev, Carlo Bencivenni, "Millimeter-Wave Vertical Transitions Between Ridge Gap Waveguides and Microstrip Lines for Integration of MMIC with Slot Array". *2021 15th European Conference on Antennas and Propagation (EuCAP)*, 2021, pp. 1-4.
 DOI: 10.23919/EuCAP51087.2021.9411273 .

[B] **Qiannan Ren**, Ashraf Uz Zaman, Jian Yang, Vessen Vassilev, Carlo Bencivenni, "Novel Integration Techniques for Gap Waveguides and MMICs Suitable for Multilayer Waveguide Applications". *Accepted by IEEE Transactions on Microwave Theory and Techniques* .

[C] **Qiannan Ren**, Ashraf Uz Zaman, Jian Yang, "A Dual Circularly Polarized Array Antenna for Ka-Band Satellite Communications". *2021 International Symposium on Antennas and Propagation (ISAP)*, 2021, pp. 1-2.
 DOI: 10.23919/ISAP47258.2021.9614491 .

[D] **Qiannan Ren**, Ashraf Uz Zaman, Jian Yang, "Dual-Circularly Polarized Array Antenna Based on Gap Waveguide Utilizing Double-grooved Circular Waveguide Polarizer". *Accepted by IEEE Transactions on Antennas and Propagation* .

Acknowledgments

First and foremost, I would like to thank my supervisor, Associate Prof. Ashraf Uz Zaman, for his kind support and supervision over the past years. His creative ideas and constructive feedback help me to resolve the confusions and challenges in the research process. I would like to thank my examiner, Prof. Jian Yang, for his encouragement and patience during the project. I would like to show deep gratitude to my manager, Prof. Marianna Ivashina, for her considerate guidance during my Ph.D life. The same goes to Prof. Rob Maaskant who kept sharing his valuable experience with me in teaching. Sincerely thanks to Dr. Oleg Iupikov, Dr. Pavlo Krasov and Dr. Artem Vilenskiy for their generous support and advice over the years.

Furthermore, I would like to thank every member of the Antenna Systems Group for creating a comfortable and productive working environment. Thanks to Dr. Jinlin Liu, Dr. Madeleine Kildal, Dr. Sadegh Mansouri Moghaddam, Dr. Artem Roev, Dr. Wan-chun Liao, Dr. Navid Amani and Dr. Jonas Flygare for sharing their senior experience with me in my earlier Ph.D. I would like to thank Zhaorui, Yingqi, Dmitrii, Prabhat, Mu, Raha, Enlin and Jin for their help and support in my research and personal life as well.

Special thanks to my co-supervisor, Dr. Carlo Bencivenni from Gapwaves AB, for his patient supervision and thoughtful suggestions during the projects. Thanks to Associate Prof. Vessen Vassilev from Department of Microtechnology and Nanoscience, for his kind supervision and caring support. I would like to thank everyone involved in the FORWARD project, Marcus Hasselblad from Gapwaves, Robert Moestam from CEVT and Olof Eriksson from Veoneer, for their engagement and contributions in this project.

The greatest thanks to my family for their selfless support and endless love.

Acronyms

ADAS:	Advanced driver assistance systems
V2X:	Vehicle to everything
LiDAR:	Light detection and ranging
FoV:	Field of view
ACC:	Adaptive cruise control
LRR:	Long-range radar
MRR:	Medium-range radar
SRR:	Short-range radar
SiP:	System in package
TX:	Transmitters
RX:	Receivers
eWLB:	Embedded wafer level ball grid array
PCB:	Print circuit board
LP:	Linear polarization
CP:	Circular polarization
MIMO:	Multi input Multi output
mmWave:	millimeter wave
PEC:	Perfect electric conductor
PMC:	Perfect magnetic conductor
CNC:	Computer numerical control
EDM:	Electric discharge machining
GGW:	Groove gap waveguide
HPGGW:	Horizontally polarized gap waveguide
RGW:	Ridge gap waveguide
IMGW:	Inverted microstrip gap waveguide
MMIC:	Monolithic microwave integrated circuit
RHCP:	Right hand circular polarization
LHCP:	Left hand circular polarization

Contents

Part I

Overview

CHAPTER 1

Introduction

This chapter briefly summarizes background of the research on automotive radar front-end. Polarimetric radar sensing are briefly introduced. Antenna design and packaging techniques based on gap waveguide technology are introduced as well. Finally, outline of the thesis is presented.

1.1 Background

The Society of Automotive Engineers (SAE) proposed a scale defining six levels of autonomous driving, ranging from Level 0 (fully manual) to Level 5 (fully automated). This scale is currently used globally by regulators and manufacturers to rate autonomous driving vehicles, as listed in Table. 1.1 [1]. Adaptive cruise control (ACC), that automatically adjusts the speed to maintain a safe distance from vehicles ahead, is categorized as lowest level (Level 1) of automation. Most vehicles on the market equipped with advanced driver assistance systems (ADAS) are considered as Level 2 autonomous driving, such as Tesla's Enhanced Autopilot, Volvo's Pilot Assist, etc. Level 3 is a significant breakthrough as the system becomes the primary driver while human drivers only intervene when it requests assistance. However, due to regulatory issues, there is still a way off for L3 autonomous driving. Level 4 autonomous driving will put enormous pressure on legislation and infrastructures, as the V2X (vehicle to everything) communication is highly involved. Level 5 autonomous vehicles are fully automated. The technologies are more appealing in the area of public transportation.

Table 1.1: Automation Levels [1]

<table>
<tr><th>Level</th><th>Name</th><th colspan="2">Narrative definition</th><th>Execution of steering and acceleration/ deceleration</th><th>Monitoring of driving environment</th><th>Fallback performance of dynamic driving task</th><th>System capability (driving modes)</th></tr>
<tr><td colspan="8">Human driver monitors the driving environment</td></tr>
<tr><td>0</td><td>No automation</td><td colspan="2">The full-time performance by the human driver of all aspects of the dynamic driving task, even when "enhanced by warning or intervention systems"</td><td>Human driver</td><td rowspan="3">Human driver</td><td rowspan="3">Human driver</td><td>N/a</td></tr>
<tr><td>1</td><td>Driver assistance</td><td>The driving mode-specific execution by a driver assistance system of either steering or acceleration /deceleration</td><td rowspan="2">Using information about the driving environment and with the expectation that the human driver performs all remaining aspects of the dynamic driving task</td><td>Human driver and system</td><td rowspan="2">Some driving modes</td></tr>
<tr><td>2</td><td>Partial automation</td><td>The driving mode-specific execution by one or more driver assistance systems of both steering and acceleration/deceleration</td><td>System</td></tr>
<tr><td colspan="8">Automated driving system monitors the driving environment</td></tr>
<tr><td>3</td><td>Conditional automation</td><td rowspan="3">The driving mode-specific performance by an automated driving system of all aspects of the dynamic driving task</td><td>With the expectation that the human driver will respond appropriately to a request to intervene</td><td rowspan="3">System</td><td rowspan="3">System</td><td>Human driver</td><td>Some driving modes</td></tr>
<tr><td>4</td><td>High automation</td><td>Even if a human driver does not respond appropriately to a request to intervene the car can pull over safely by guiding system</td><td rowspan="2">System</td><td>Many driving modes</td></tr>
<tr><td>5</td><td>Full automation</td><td>Under all roadway and environmental conditions that can be managed by a human driver</td><td>All driving modes</td></tr>
</table>

Table 1.2: A comparison of the commonly employed sensors in self-driving cars: cameras, LiDAR, and radar, based on technical characteristics and other external factors. The "✓" symbol indicates that the sensor operates competently under the specific factor. The "∼" symbol indicates that the sensor performs reasonably well under the specific factor. The "✗" symbol indicates that the sensor does not operate well under the specific factor relative to other sensors [4].

Factors	**Camera**	**LiDAR**	**Radar**	**Fusion**
Range	∼	∼	✓	✓
Resolution	✓	∼	✗	✓
Distance Accuracy	∼	✓	✓	✓
Velocity	∼	✗	✓	✓
Color Perception, e.g. traffic lights	✓	✗	✗	✓
Object Detection	∼	✓	✓	✓
Object Classification	✓	∼	✗	✓
Lane Detection	✓	✗	✗	✓
Obstacle Edge Detection	✓	✓	✗	✓
Illumination Conditions	✗	✓	✓	✓
Weather Conditions	✗	∼	✓	✓

Autonomous driving vehicles demand numerous sensors to perceive their surroundings, such as video cameras, radar, light detection and ranging (LiDAR) or ultrasonic [2], [3]. The sensory information is processed to identify navigation paths, traffic sign, obstacles, etc. The variety of sensors have their strengths and weaknesses under different scenarios as shown in Table. 1.2 [4]. The most reliable solutions are the sensor fusion techniques which utilizes multiple sensors simultaneously. Sensor fusion systems are able to benefit from the strengths and reduce detection uncertainties with overlapping and redundant functions of various sensors. For instance, camera and radar fusion provides images with high resolution, meanwhile presents relative range and velocities of the detected obstacles.

Radar sensors radiate electromagnetic waves within the field of view (FoV), then receive the scattered waves of targets for further signal processing. Because electromagnetic waves are less susceptible to adverse weather conditions compared to light detection, radar sensors are able to operate in foggy, dusty, snowy or other bad lighted environments. In addition, the cost of mass-produced radar sensors is decreasing, thus making them more attractive to industrial applications. Most autonomous vehicles on the market are equipped with several radar sensors mounted in several locations, such as on the roof near the top of windshield, behind the vehicle bumpers or brand emblems. Aforementioned qualities of the

radar sensors make them indispensable in sensor fusion systems [5], [6].

Previously, automotive radars operating at 77 GHz band (76-77 GHz) were mainly for long-range radar (LRR) applications such as ACC. However, medium-range radar (MRR) and short-range radar (SRR) applications are compatible with 77 GHz band as well [7]–[9]. Works in this thesis will focus on the 77 GHz band.

1.2 Polarimetric Radar Sensing

Higher level (3-5) autonomous vehicles are capable of driving independently by heavily relying on the sensory data. This poses tremendous challenges on the perception sensors in terms of target classification, environmental adaptability, etc. It requires more sophisticated antenna systems with better detectability [10], [11]. In this respect, polarimetric radars that utilize orthogonal polarizations on transmitting and receiving have been investigated.

Polarimetric scattering matrix represents the connection between incident and scattered waves of the target:

$$\mathbf{E_s} = \frac{e^{-j\mathbf{kr}}}{\sqrt{4\pi}|\mathbf{r}|}\begin{pmatrix} S_{11} & S_{12} \\ S_{21} & S_{22} \end{pmatrix}\mathbf{E_i} \tag{1.1}$$

where $\mathbf{r}$ is the distance vector between the radar sensor and target, $\mathbf{k}$ is the electromagnetic wave number, $\mathbf{E_i}$ and $\mathbf{E_s}$ are the incident and scattered waves respectively. Entries of the scattering matrix can be defined on certain orthogonal polarization basis. If the system uses linear polarization (LP) basis:

$$\begin{pmatrix} \mathbf{E_{s,H}} \\ \mathbf{E_{s,V}} \end{pmatrix} = \frac{e^{-j\mathbf{kr}}}{\sqrt{4\pi}|\mathbf{r}|}\begin{pmatrix} S_{HH} & S_{HV} \\ S_{VH} & S_{VV} \end{pmatrix}\begin{pmatrix} \mathbf{E_{i,H}} \\ \mathbf{E_{i,V}} \end{pmatrix} \tag{1.2}$$

Subscript letters H and V represent horizontal and vertical polarization respectively. If the system uses circular polarization (CP) basis:

$$\begin{pmatrix} \mathbf{E_{s,L}} \\ \mathbf{E_{s,R}} \end{pmatrix} = \frac{e^{-j\mathbf{kr}}}{\sqrt{4\pi}|\mathbf{r}|}\begin{pmatrix} S_{LL} & S_{LR} \\ S_{RL} & S_{RR} \end{pmatrix}\begin{pmatrix} \mathbf{E_{i,L}} \\ \mathbf{E_{i,R}} \end{pmatrix} \tag{1.3}$$

Subscript letters L and R represent left hand and right hand circular polarization respectively. Three basic independent symmetric scattering objects are proposed in [12]: plate, dihedral, dipole. Scattering matrices of the three basic objects are:

$$S_{\text{plate},LP} = \begin{pmatrix} 1 & 0 \\ 0 & 1 \end{pmatrix} \quad S_{\text{plate},CP} = \begin{pmatrix} 0 & 1 \\ 1 & 0 \end{pmatrix} \tag{1.4}$$

$$S_{\text{dihedral},LP} = \begin{pmatrix} cos(2\Psi) & sin(2\Psi) \\ sin(2\Psi) & -cos(2\Psi) \end{pmatrix} \quad S_{\text{dihedral},CP} = \begin{pmatrix} e^{j2\Psi} & 0 \\ 0 & e^{-j2\Psi} \end{pmatrix} \tag{1.5}$$

$$S_{\text{dipole},LP} = \begin{pmatrix} cos^2(\Psi) & cos(\Psi)\ sin(\Psi) \\ cos(\Psi)\ sin(\Psi) & sin^2(\Psi) \end{pmatrix} \quad S_{\text{dipole},CP} = \frac{1}{2}\begin{pmatrix} e^{j2\Psi} & 1 \\ 1 & e^{-j2\Psi} \end{pmatrix} \tag{1.6}$$

where Ψ represents the inclination angle of the dihedral or dipole. Current systems utilizing single LP that lack polarimetric capabilities are not capable of measuring the full scattering matrix, thus losing information about the scenery [13]. For instance, radar systems with

horizontal polarization in both transmitting and receiving are not able to detect a dihedral with inclination angle of 45°. Moreover, polarimetric radar systems based on linear polarizations require horizontal and vertical polarization on both TX and RX sides to avoid possible blind spots. In contrast, fully polarimetric systems are not necessary with circular polarization. For example, radar systems with one CP on TX side and two CPs on RX side are capable of detecting a dipole with any inclination angle.

Polarimetric sensing is employed in synthetic aperture radar imaging, Doppler weather radar, as well as road surface monitoring. Perception of the road surface conditions is essential for autonomous driving applications. Passive radiometers with polarimetric capabilities are investigated to recognize the road condition of dry surface, liquid water and ice on asphalt [14]. Polarimetric radars are used for road recognition as well [15]–[17]. Polarimetric MIMO systems for automotive applications have been investigated recently [18], [19]. MIMO system provides a cost-effective approach to improve angular resolution of the radar by multiplexing transmissions across a number of antennas [20].

1.3 Gap Waveguide Technologies

In the history of microwave engineering, the innovation of waveguide transmission line is one of the milestones. In the very beginning, it was generally believed that two conductors were necessary for wave propagation [21]. Mathematical verification of wave propagation in waveguides with circular and rectangular cross-sections was not presented until 1897 [22]. Till 1936, experimental confirmation of the waveguide propagation were presented and waveguides start to attract more and more attention [23].

Waveguides have the advantages of high power-handling capability and are quite popular in large gain/high efficiency array antenna designs due to their low-loss properties. However, the fabrication of waveguides become more challenging at higher frequencies with shrinking wavelength. In general, the waveguide modules are manufactured in split-blocks and then connected by screwing, or in case of even higher frequency, diffusion bonding and vacuum brazing. The assembly becomes critical because it's getting difficult to achieve reliable electrical contacts of the split blocks at higher frequencies. This requires new waveguide technologies that are more cost-effective than common hollow waveguide and able to provide reliable assembly at mmWave wave frequency band.

Gap waveguide technologies are able to address the aforementioned problems and have gained enormous interests among the industrial and academic world over the last ten years. To explain the operating principles of gap waveguide, consider a parallel plate structure that consists of a upper PEC and a lower PMC, as shown is Fig. 1.1a. No wave can propagate through the plates if the air gap separation is less than quarter wavelength, unless the PMC surface incorporates guiding structures, as shown in Fig. 1.1b.

In practical applications, the PMC condition is emulated by periodic textured structures, such as metal pins or mushroom structures [24], [25]. Depending on the guiding structures, the gap waveguide transmission lines have different configurations as shown in Fig. 1.2.

Several multi-layer waveguide components based on gap waveguide, such as slot arrays, filters and diplexers, have been widely discussed [26]–[32]. It has been shown that gap waveguide based components have competitive performance compared with conventional waveguide based components. Moreover, gap waveguide technology brings more flexibility

Figure 1.1: Cross section of ideal gap waveguide.

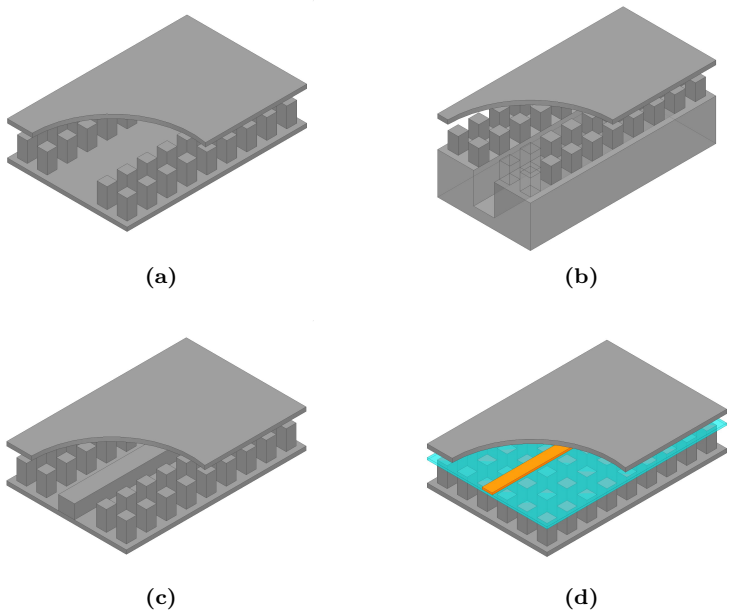

Figure 1.2: Gap waveguide configurations: (a) groove gap waveguide (GGW), (b) horizontally polarized gap waveguide (HPGGW), (c) ridge gap waveguide (RGW), (d) inverted microstrip gap waveguide (IMGW).

to the design of interconnections between the layers. Gap waveguide technology has been investigated for integration of mmWave front-end as well [33]. Gap waveguide integration is a multi-layer integration technique which features the advantages of non-galvanic contact between the layers, thereby ensure higher reliability of assembly, and robustness of the entire system[34].

Traditionally, CNC milling is used for fabrication of gap waveguide components, the

cost is increasing due to small features and time-consuming fabrication. Recently, more and more low cost techniques have been utilized for gap waveguide manufacturing, such as die-sink Electric Discharge Machining (EDM), 3D printing, plastic injection molding and micro-machining [35]–[39]. Therefore, pressure on expensive manufacturing and precise mechanical assembly are eased for gap waveguide components at mmWave frequency band.

1.4 Thesis Outline

This thesis is divided into two parts. The first part has been organized in three chapters. Chapter one briefly introduces background of the thesis work. Chapter two presents the works on dual circularly polarized array antennas using double grooved circular waveguide polarizer. Chapter three introduces the works on transitions from microstrip to gap waveguide transmission line. Additional chapters on paper summary and future possibilities are included. The author's contributions are appended in the second part of the thesis, in the form of academic research papers.

CHAPTER 2

Advanced Antenna Systems for Automotive Radar Applications

2.1 State-of-the-art Technologies

Most automotive radar sensors on the market are realized with single linear polarization (LP) for the simplest implementation. Additionally, the vast majority of them are built on highly integrated system-in-package (SiP) components featuring multiple transmitters (TXs) and receivers (RXs) with functionalities from RF front-end to IF signal processing [40], [41]. Embedded wafer level BGA (eWLB) is one of the advanced packaging technologies for such radar transceivers [42]. It can provide components with flip-chip assembly which is favorable for applications based on print circuit board (PCB). This leads logically to PCB antenna being the most widely used antenna connected to the transceiver. Fig. 2.1 shows a few off-the-shelf automotive radar sensors on the market. Microstrip patch antennas are the most popular on-board antennas due to their simplest integration with PCB. As a result of the effortless and compact feeding networks, series-fed microstrip patch arrays have been widely investigated. In [43], a series-fed patch array is presented with shaped azimuth (AZ) radiation pattern to fulfill both long-range and medium-range detection, as shown in Fig. 2.2. A 16-element phased array with $\pm 50^\circ$ beam scanning is presented in [44] based on series-fed patch array, as shown in Fig. 2.3. In general, the distance between the adjacent patches is approximately one guided wavelength. Width of the patches will be optimized to realize certain excitation distribution, while length of the patches is kept half guided wavelength. Other configurations of linearly polarized series-fed patch arrays,

such as differential patch array and comb-line patch array, have been investigated as well, as shown in Fig. 2.4 [45], [46].

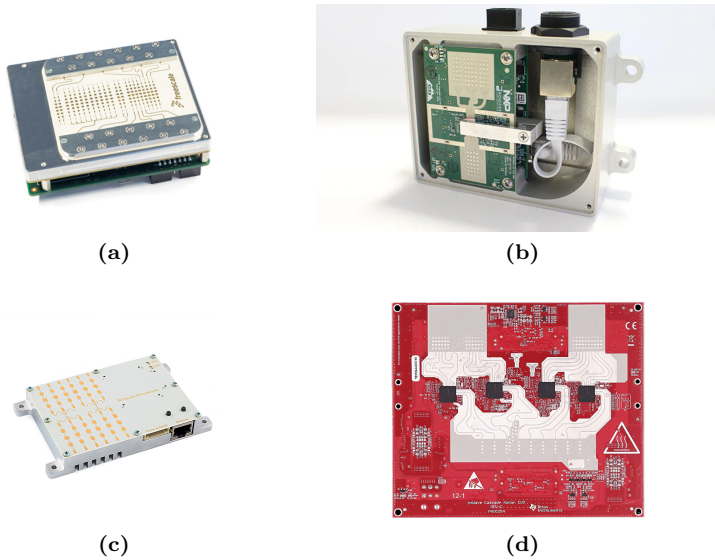

Figure 2.1: Radar sensors on the markets: (a) 76-77 GHz radar sensor with 4 TXs and 6 RXs [47], (b) 77 GHz radar sensor with 3 TXs and 4 RXs [48], (c) 24GHz FMCW radar sensor with 1 TX and 3 RXs [49], (d) 77 GHz mmWave cascade imaging radar RF evaluation module with 12 TXs and 16 RXs [50].

As demonstrated in the previous chapter, advanced radar sensors require sophisticated antenna systems with dual polarization. Substrate integrated waveguides (SIW) have been investigated for dual circularly polarized array antenna [51], [52]. The designs normally feature independent feeding networks for each polarization and rely on multi-layer PCB technology. In [51], a 8×8 dual circularly polarized planar array based on SIW is presented as shown in Fig. 2.5a. Circular polarizations are realized by orthogonal linear polarizations with 90° phase difference. In [52], a parallel plate long-slot array based on SIW is presented as shown in Fig. 2.5b. Perpendicular long slots with quadrature excitations are utilized to generate the circular polarizations. Despite that the SIW designs showed promising radiating performance regarding axial ratio, side-lobe level, etc, the expensive fabrication and space-consuming layout have been hindering the application.

In order to realize a compact and cost-effective antenna system with polarimetric capability, dual polarized microstrip patch arrays have been investigated [10], [53]. In [10], radar systems using left-hand circularly polarized TXs and dual linearly polarized RXs are

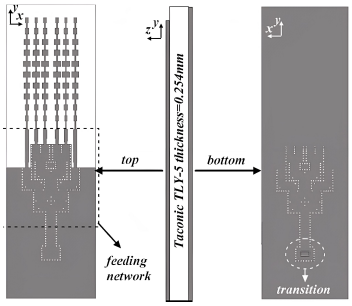

Figure 2.2: Configuration of the proposed antenna [43].

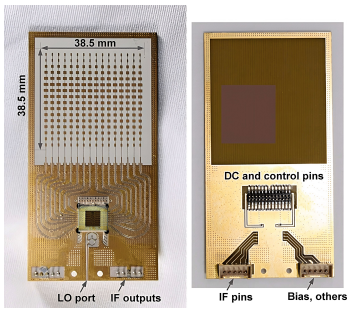

Figure 2.3: Configuration of the proposed antenna [44].

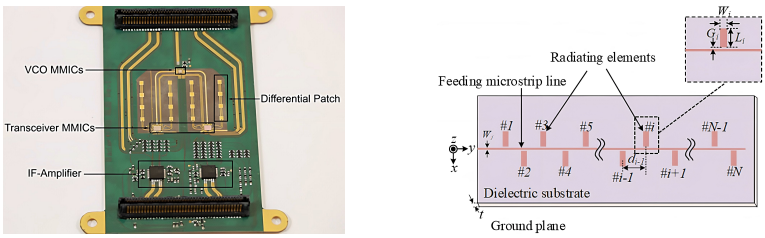

(a) **(b)**

Figure 2.4: Configuration of the proposed (a) differential patch array [45] and (b) comb-line patch array [46].

discussed. The antennas are based on square patch elements with series–parallel feeding networks and able to be realized on a single layer PCB, as shown in Fig. 2.6a. The patch

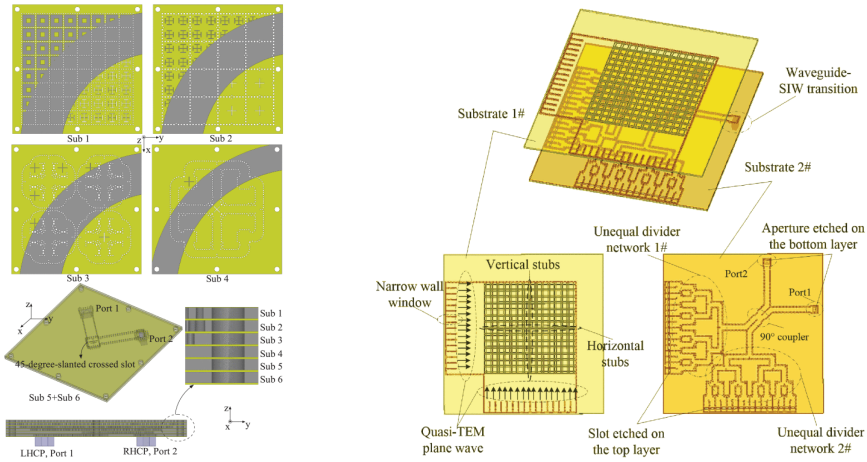

Figure 2.5: Configuration of the proposed dual circularly polarized array antenna based on SIW technology (a) at 60 GHz [51] and (b) 94 GHz [52].

elements are inclined by 45° for symmetric linear polarizations. The array has been optimized for low side-lobe level. Circularly polarized TX antenna is realized by combining the dual linearly polarized column with a 90° hybrid network, as shown in Fig. 2.6b.

Besides the aforementioned limitations, dielectric loss will deteriorate the RF performance of the PCB antenna, especially when complex antenna systems are used [10], [54]. On-board antennas also lack flexibility for routing of the feeding lines and placement of the antenna elements. Therefore, waveguide antenna placed on top of the transceivers becomes a better candidate to implement a complex antenna system with high efficiency in radar sensing applications [18], [55].

Linearly polarized waveguide slot arrays have been employed for advanced radar front-end recently. In [56], a simultaneous multi-mode imaging radar system based on waveguide slot arrays is presented. Utilizing four radar transceivers, each equipped with 3 TXs and 4 RXs, the imaging radar is able to implement high angular resolution in both azimuth (AZ) and elevation (EL). Antenna system based on complex MIMO configurations is proposed. The 16 RX antennas are placed side-by-side, while the 12 TX antennas are classified according to different operating modes. The layout of the antenna system is compact, meanwhile space-consuming. Conventional PCB antenna will lead to a cumbersome and lossy design. Therefore, waveguide slot arrays are employed to implement the antenna system with more flexibility and higher efficiency as shown in Fig. 2.7.

Fully polarimetric automotive radar systems based on waveguide antennas are discussed in [13], [57]. As depicted in Fig. 2.8, dual linearly polarized MIMO systems based on sectoral waveguide horn antennas are presented. E-plane sectoral horns are utilized for vertical

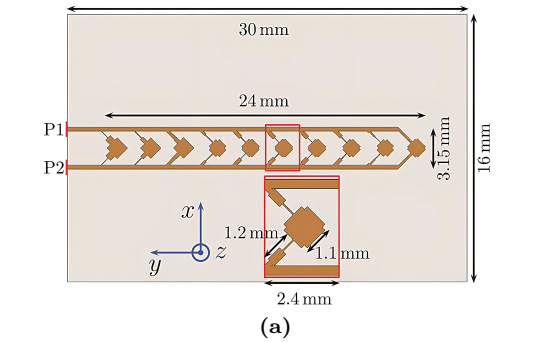

(a)

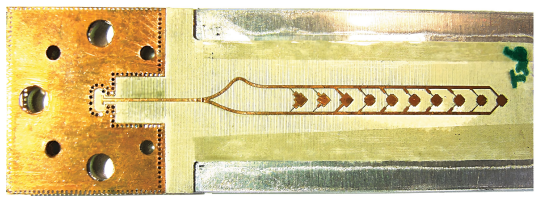

(b)

Figure 2.6: Configuration of the proposed patch array (a) dual linearly polarized and (b) left hand circularly polarized [10].

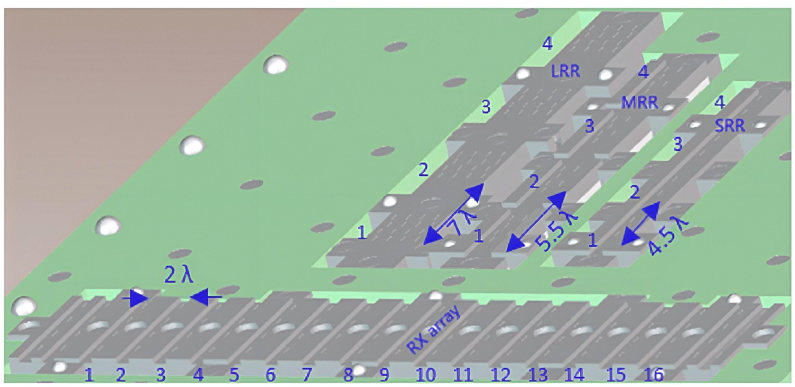

Figure 2.7: Simultaneous multi-mode automotive imaging radar system using waveguide slot arrays. [56].

polarization, while H-plane sectoral horns are utilized for horizontal polarization. Sectoral horn antennas are able to provide broad azimuth patterns and narrow elevation patterns, making them suitable for automotive applications. The systems are on the basis of TDM MIMO operation. Configuration A leads to a MIMO virtual array with angular ambiguities, while configuration B is an improved design. Despite high polarization isolation, sector horn antennas are incompetent for low-profile designs and lack scalability for high gain scenarios, such as long-range applications.

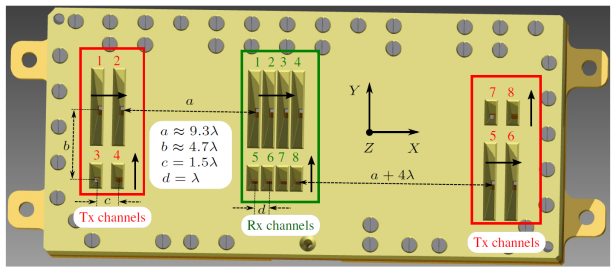

(a)

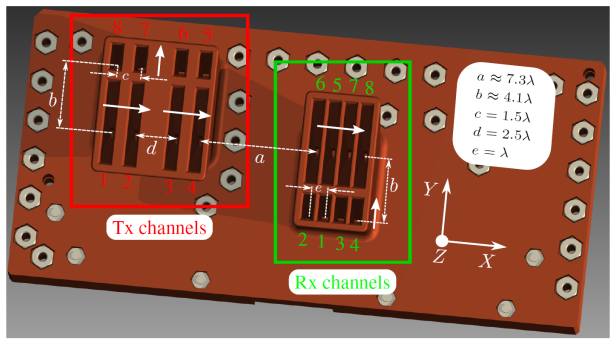

(b)

Figure 2.8: Proposed dual-polarized MIMO waveguide antenna: (a) configuration A, (b) configuration B [13].

Dual circularly polarized waveguide antennas for polarimetric radar applications are investigated as well. In [18], a polarimetric radar sensing system with 6 LHCP TXs and 16 dual circularly polarized RXs is presented as shown in Fig. 2.9. The receiving antenna array consists of 16 columns with 8 dual circularly polarized corrugated horns each. Septum polarizers fed by power splitters based on T-junctions are utilized to generate dual circular polarizations. Due to size constraints of the horns, the receiving antennas are separated by one wavelength, while the transmitting antennas are separated by 1.5 wavelength. With time division multiplexing (TDM) MIMO operation, a half wavelength spaced virtual array

is achieved. Notice that the TX array has a 3×2 lattice, it means the system is able to perform direction of arrival (DoA) estimation in both azimuth and elevation.

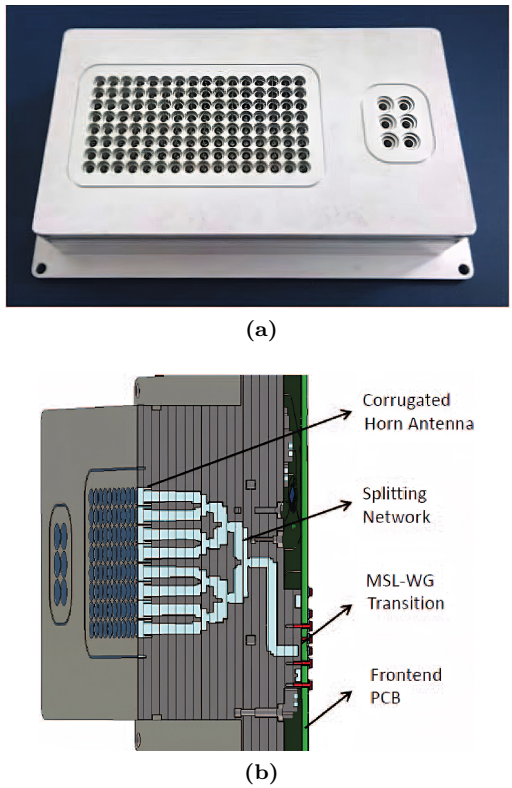

(a)

(b)

Figure 2.9: Configuration of the proposed dual circularly polarized waveguide array: (a) fully-manufactured prototype, (b) cross section of the waveguide array [18].

In a nutshell, dual polarized waveguide antennas are one of the best candidates to implement sophisticated polarimetric radar systems. Moreover, linear polarizations are more susceptible to multi-path fading and polarization rotation compared with circular polarization. In this regard, dual circularly polarized waveguide antenna are of high interest.

2.2 Dual Circularly Polarized Waveguide Antennas

Generally, circularly polarized waves can be generated by combining two orthogonal linearly-polarized waves with 90° phase difference. In this regard, dual circular polarization can be realized by putting dual linearly polarized antennas and 90° hybrid feeding networks together[58]. Another typical circularly polarized antenna is travelling wave slot array. In [59], circularly polarized rectangular waveguide slot arrays are presented as depicted in Fig. 2.10. Each radiating element consists a pair of perpendicular slots with 45° inclination. The waveguide is terminated by a matching load enabling a travelling wave propagation. For each element, the slots are approximately quarter guided-wavelength spaced, while adjacent radiating elements are one guided-wavelength spaced. The waveguide is filled with dielectric to make sure that the guided wavelength is shorter than free space wavelength. Otherwise grating lobes will appear.

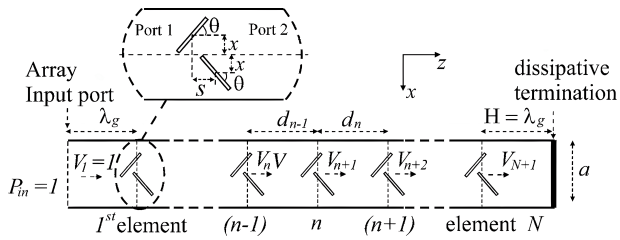

Figure 2.10: Proposed travelling wave CP linear array based on inclined waveguide slots [59].

Dual circularly polarized travelling wave slot arrays based on parallel plate are presented in [60]. Parallel plate modes are excited by alternating the feeding waveguide slots, as shown in Fig. 2.11. The parallel plates are separated by honeycomb dielectrics. Since the dominant modes of parallel plate are TEM modes, the design is even more compact with the shrinking guided wavelength. Dual polarizations are realized by exciting the parallel plate modes propagating in opposite directions. In spite of the simplest feeding networks, circularly polarized travelling wave slot arrays find limited applications due to the problems of narrow bandwidth, beam squinting, scanning capability, etc.

Waveguide polarizers are widely used in directly generating circularly polarized waves. The most popular polarizers of dual circular polarization are septum polarizers, as shown in Fig. 2.12. Two rectangular waveguide input ports are separated by a septum. Port 3 and 4 are overlapped and realized by quadratic waveguides. Assuming an ideal lossless situation, the septum polarizer is described by a scattering matrix:

$$\left[S_{ij}\right] = \frac{1}{\sqrt{2}} \begin{bmatrix} 0 & 0 & 1 & -j \\ 0 & 0 & -j & 1 \\ 1 & -j & 0 & 0 \\ -j & 1 & 0 & 0 \end{bmatrix} \tag{2.1}$$

where $S_{ij} = V_i^- / V_j^+$, V_i^- is the amplitude of the wave leaving port i, V_j^+ is the amplitude

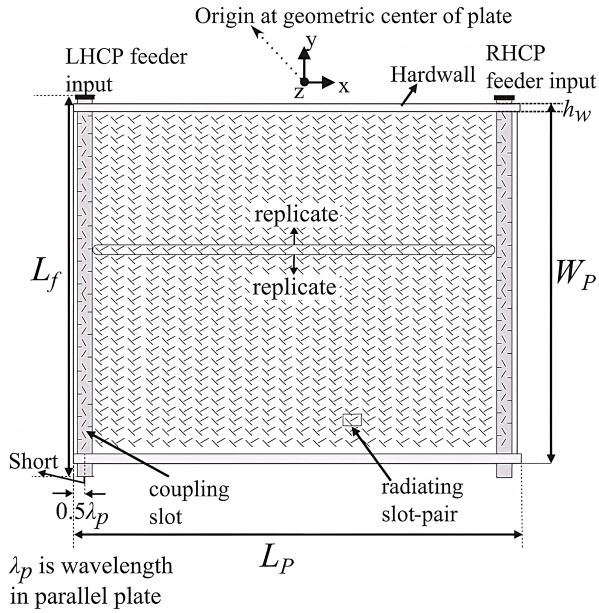

Figure 2.11: Proposed dual circularly polarized travelling-wave antenna using parallel plate slot pairs [60].

of the wave exciting port j. When port 1 is excited, electric field at the output will be:

$$\mathbf{E}_{RHCP} = S_{31}\hat{\mathbf{x}} + S_{41}\hat{\mathbf{y}} = (\hat{\mathbf{x}} - j\hat{\mathbf{y}})/\sqrt{2} \tag{2.2}$$

representing right hand circular polarization (RHCP). When port 2 is excited, electric field at the output will be:

$$\mathbf{E}_{LHCP} = S_{32}\hat{\mathbf{x}} + S_{42}\hat{\mathbf{y}} = (-j\hat{\mathbf{x}} + \hat{\mathbf{y}})/\sqrt{2} \tag{2.3}$$

representing left hand circular polarization (LHCP).

The quadratic waveguide output is extremely applicable, in particular for feeding circular waveguide horn antennas with dual circular polarization [61]. The septum polarizer has been investigated in planar array design as well. A 16×16 dual circularly polarized planar array based on septum polarizers is presented in [62]. The challenge is to implement corporate feeding networks for the dual polarization. As depicted in Fig 2.13, independent corporate feeding networks are realized by cascading E- and H-plane T junctions. Moreover, due to size constraints, the planar array is built on 2×2 sub-array with back cavity, in order to avoid grating lobes. Despite of being compact in size, septum polarizers are quite challenging from fabrication and assembly point of view at mmWave frequency range.

Recently, grooved circular waveguide polarizers have been investigated for dual circularly

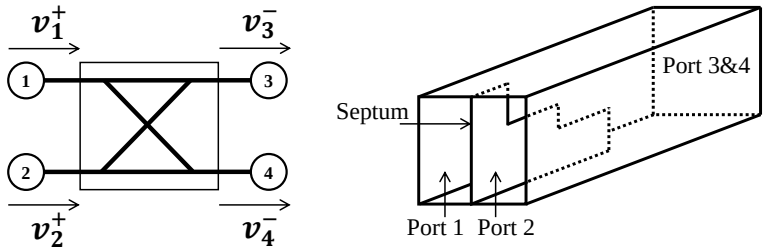

Figure 2.12: Illustration of a four-port septum polarizer.

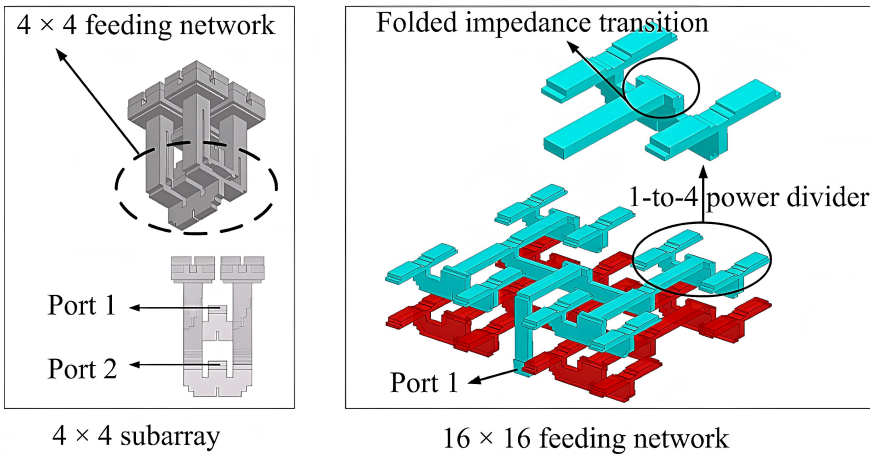

Figure 2.13: Proposed corporate-feeding network for dual circularly polarized array [62]

polarized antenna design [63]–[66]. As depicted in Fig. 2.14, circular waveguides with sector grooves are recognized as grooved circular waveguides, such as mono-grooved circular waveguide, double-grooved circular waveguide. Meanwhile, considering the configurations as circular waveguides with embedded sector ridges, the waveguides are also known as ridged circular waveguides. Rigorous analytical solutions for the wave propagation of ridged circular waveguides are presented in [67], [68].

A section of grooved circular waveguide can be used as a polarizer to generate circularly polarized waves as shown in Fig. 2.15. When the excitation field at the input is polarized in Y direction, the dominant TE_{11} mode inside the circular waveguide, annotated as $\mathbf{E_R}$, can be decomposed into two orthogonal components with the same amplitude: $\mathbf{E_{R1}}$ and $\mathbf{E_{R2}}$. When the field propagates through the double grooved circular waveguide, $\mathbf{E_{R2}}$ will

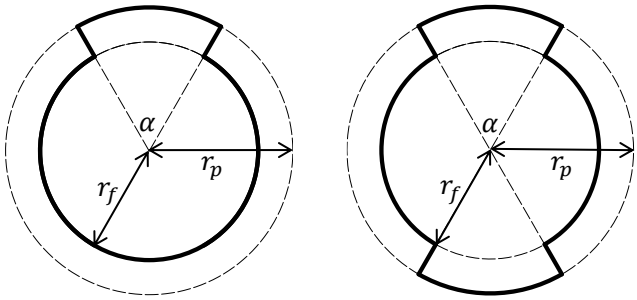

Figure 2.14: Sectional view of (left) mono-grooved circular waveguide and (right) double grooved circular waveguide.

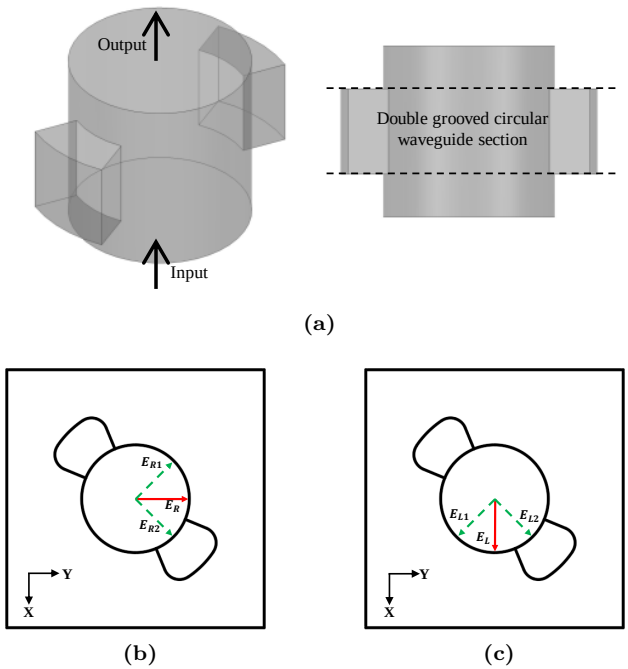

Figure 2.15: Illustration of double grooved circular waveguide polarizer.

experience a larger propagation radius than $\mathbf{E_{R1}}$. The phase difference between the two components at the output can be written as:

$$\Delta\phi = \phi_1 - \phi_2 = (\beta_1 - \beta_2)L_p \tag{2.4}$$

where

$$\beta_1 = \sqrt{k^2 - (\frac{p_{11}^{'}}{r_f})^2} \tag{2.5}$$

$$\beta_2 = \sqrt{k^2 - (\frac{p_{11}^{'}}{r_p})^2} \tag{2.6}$$

L_p is the length of the double grooved circular waveguide section, β_1 and β_2 are the wave numbers of $\mathbf{E_{R1}}$ and $\mathbf{E_{R2}}$, respectively. $p_{mn}^{'}$ is the first root of the derivative of first order Bessel function. If $\mathbf{E_{R1}}$ is delayed by 90° compared to $\mathbf{E_{R2}}$, the output field will be right hand circularly polarized. Likewise, when the excitation field at the input is polarized in X direction, left hand circularly polarized wave will be generated if $\mathbf{E_{L2}}$ is 90° phase ahead of $\mathbf{E_{L1}}$ at the output. In [64], polarizers based on mono-grooved circular waveguides are discussed. Compared with double grooved circular waveguide polarizers, mono-grooves are larger in size. In addition, the asymmetric configurations deteriorate the bandwidth of the polarizer.

However, grooved circular waveguide polarizers have never been utilized in an array configuration due to complexity of the fabrication and size constraints. In this thesis, planar arrays based on double grooved circular waveguide polarizers are presented in **Paper C** and **Paper D**. The planar arrays are built on 2×2 sub-array with back cavity, in order to eliminate grating lobes. The designs demand multi-layer feeding networks. The polarizers are implemented by stacked layer as well. Advanced designs based on gap waveguide technologies are presented in **Paper D** for fixed beam, high gain polarimetric sensing applications. Independent, highly isolated and compact feeding networks based on gap waveguide technologies are proposed. For more details of the design, please refer to the appended **Paper D**.

CHAPTER 3

Integration of Automotive Radar Front-end

3.1 State-of-the-art technologies

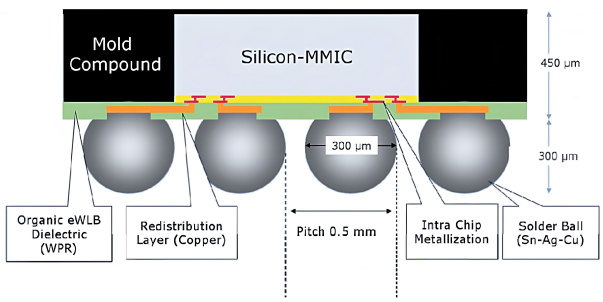

Figure 3.1: Cross section of an eWLB package [69].

As discussed in the previous chapter, automotive radar sensors on the market are always built on integrated transceivers with multiple TXs and RXs. The most popular packaging technique for the transceiver is embedded wafer level ball grid array (eWLB), as shown in Fig. 3.1. The technique is low-cost, reliable and easy to integrate with PCB. Comparison among several off-the-shelf radar transceivers operating at 76-81 GHz is given in Table.

3.1. The transceivers integrate not only RF front-end blocks, such as LNA, PA, mixer, etc, but also built-in PLL and ADC converter. More advanced designs even integrate micro-controller units (MCU) or digital signal processor (DSP) blocks for signal processing. The transceivers will be surface mounted on PCB boards, which referred to as flip-chip assembly, as shown in Fig. 3.2. To ensure reliable electrical contact between the solder balls and PCB pads, the surface mount process need to consider optimum solder paste volume, accurate component placement, proper reflow temperature [70].

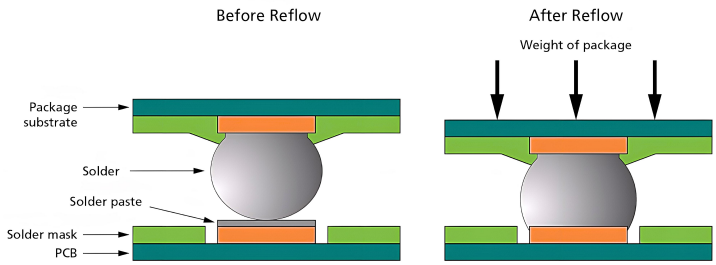

Figure 3.2: Surface mount process of the BGA components [70].

Figure 3.3: Exploded view of the Bosch RADAR sensors [71].

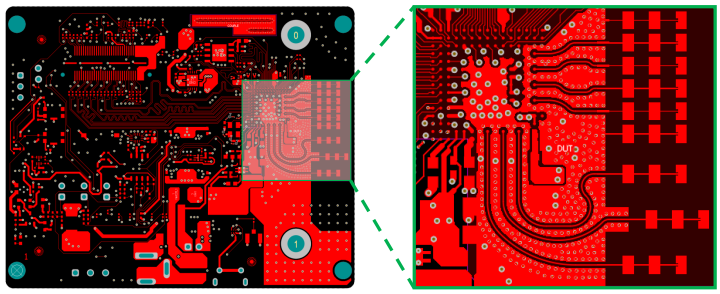

Figure 3.4: PCB layout of Texas Instruments AWR2243 evaluation module [72].

Table 3.1: Comparison among off-the-shelf radar transceivers operating at 76-81 GHz.

Transceiver	TX Qty.	RX Qty.	Noise Figure (dB)	Transmit Power (dBm)	Manufacturer
TEF82XX	3	4	11.5	13.5	NXP
TEF810X	3	4	12	12	NXP
AWR1243	3	4	14	12	TI
AWR2243	3	4	12	13	TI
RXS816xPL	3	4	∼	∼	Infineon
RXS8156PLA	2	4	∼	∼	Infineon
CAL77A4T8R	4	8	12	13	Calterah
CAL77A2T4R	2	4	12	13	Calterah

PCB-based integration is most sought-after integration technique for automotive radar sensors. Fig. 3.3 shows a couple of off-the-shelf radar sensors with exploded 3D structures. Normally, a typical radar sensor consists of a housing frame with connectors, a DSP board for signal processing, a shielding metal layer for electromagnetic compatibility consideration, a RF board for the integration of radar transceivers with on-board antennas, and finally a radom cover. The PCB antennas demand low-loss and cost-effective dielectrics. In addition, thermal expansion, moisture absorption and other factors would affect the stability of the radar systems as well. The transceivers are normally placed in close proximity with PCB antennas to avoid lossy routing of the feeding lines. This causes problems on transmitting/receiving isolation, electromagnetic compatibility of the transceiver, interference on

the radiation pattern, etc.

The transition from the eWLB solder balls to PCB antennas (most likely microstrip patch arrays) is quite straightforward, as shown in Fig. 3.4. The solder balls are mounted on grounded coplanar waveguides (GCPW) directly. GCPW is able to reduce the coupling of adjacent transmission lines. The grounded vias help with suppression of parasitic substrate modes. The transitions to microstrip lines are realized by quarter wavelength transformers.

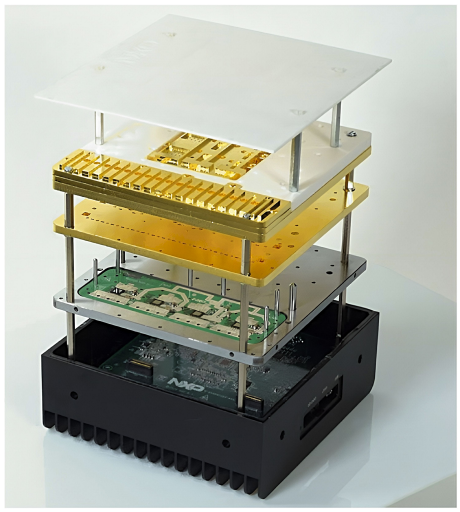

(a)

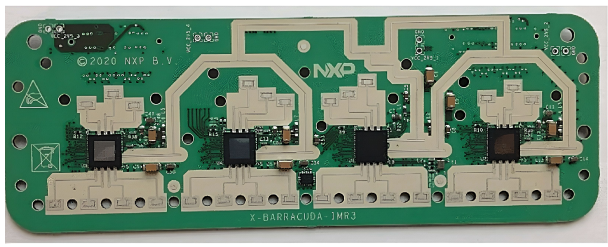

(b)

Figure 3.5: Simultaneous multi-mode automotive imaging radar system using waveguide slot arrays: (a) construction of the system, (b) RF board integrated with 4 radar transceivers [56].

Integration of RF front-end with waveguide antennas has been investigated. As discussed in **Chapter 2**, a simultaneous multi-mode imaging radar system is presented in [56]. The complex antenna system is implemented with conventional rectangular waveguide slot ar-

rays. The waveguide slot arrays are fabricated by plastic milling for a light-weight design. Construction of the imaging radar system is shown in Fig. 3.5a. The waveguide antennas are placed on top of the RF boards, providing shielding for the active circuits while saving board space. The imaging radar integrates 4 radar transceivers mounted on a RF board, as shown in Fig. 3.5b. One critical part of the integration is the transition from on-board planar transmission line to waveguide, which will be discussed in the next section. Additional transitions from differential line to microstrip are implemented on board since the transceivers have differential RF ports.

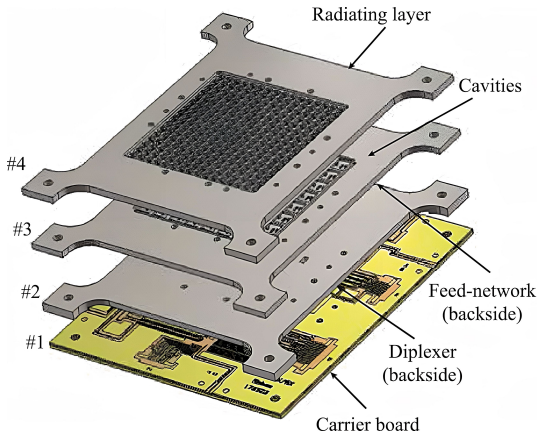

(a)

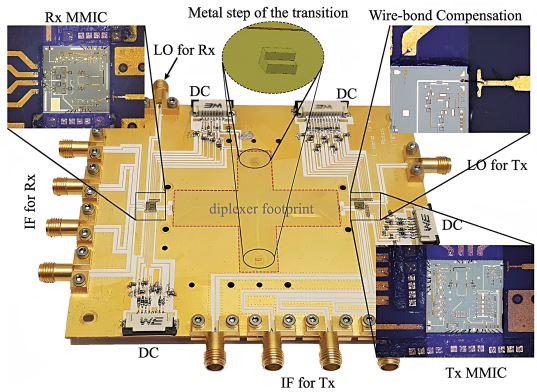

(b)

Figure 3.6: (a) Configuration of the proposed RF front-end, (b) RF board integrated with transitions and MMICs [33].

Gap waveguide technology has been investigated in integration of RF front-end recently. Not only because multi-layer gap waveguide antennas have advantages over conventional waveguide design, but also the gap waveguide packaging techniques benefit the reliability of the system. In [33], one RF front-end for high data rate communications at E band is presented utilizing gap waveguide technologies. A 16×16 gap waveguide slot array with a diplexer at the input is placed on top of the RF board, as shown in Fig. 3.6a. RX and TX MMICs are integrated with the RF board via bond-wire connection. Integration of the waveguide antenna with the RF board is realized by in-line transitions from microstrip to groove gap waveguide.

3.2 Transition from on-board planar transmission line to waveguide

As discussed in the previous section, the integration of waveguide antenna with RF board mostly relies on the transition from on-board planar transmission line to waveguide. For conventional rectangular waveguide, such transitions have been widely investigated. In general, microstrip to waveguide transitions are categorized as broadside E-plane transition and longitudinal H-plane transition, as illustrated in Fig. 3.7 [73]. In [74], two transitions from microstrip to rectangular waveguide are presented as shown in Fig. 3.8. The transitions operate from 76 to 81 GHz, suitable for automotive radar applications. The transitions are considered as H-plane transition with vertical configurations. The patch probes are offset from the central line to generate the waveguide modes. The elevated ground plane with metalized vias prevents the field from leaking through the substrate. Waveguide iris is employed to achieve broader bandwidth in the second configuration. The transitions are able to be implemented in a single-layer PCB.

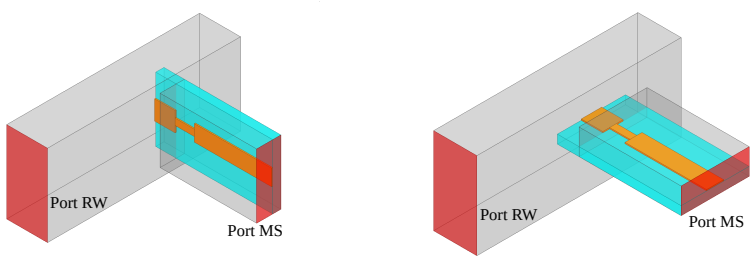

Figure 3.7: (a) broadside E-plane transition from microstrip to waveguide, (b) longitudinal H-plane transition from microstrip to waveguide [73].

In [75], a waveguide-to-microstrip transition based on a double-layer substrate is presented. The transition is considered as broadside E-plane transition. The microstrip is

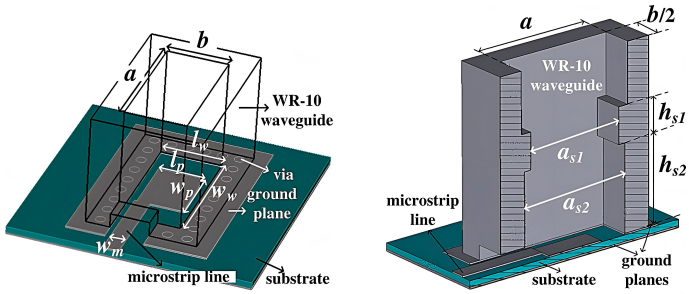

Figure 3.8: 3-D structures of the proposed vertical transitions: (a) without the waveguide iris, (b) with the waveguide iris [74].

transformed to SIW, then connected to the waveguide placed on top of the board. The input matching is tuned by the microstrip probe, as well as a coupling patch inserted in the middle. Metalized vias of the SIW prevent the field from leaking through the substrate. Similarly, a broadside E-plane microstrip-to-waveguide transition is presented in[76]. The microstrip line is transformed to GCPW in order to excite the SIW modes, as shown in Fig. 3.10. A rectangular patch is utilized to tune the matching as well.

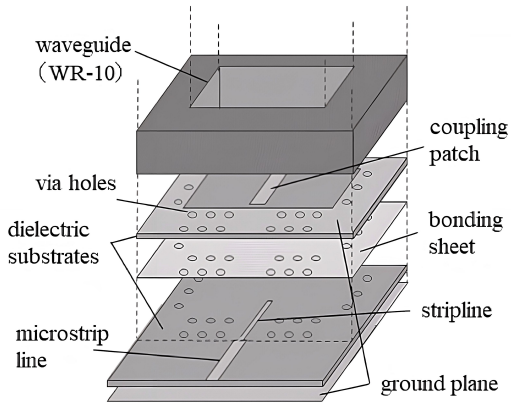

Figure 3.9: Proposed vertical transition from waveguide to microstrip [75].

Transitions from microstrip to gap waveguide transmission lines have been investigated. However, most of them are in-line transitions, not suitable for integration in vertical configuration. In [33], an in-line transition from microstrip to GGW is presented. The transition is classified as broadside E-plane transition. A back-short cavity is utilized underneath the

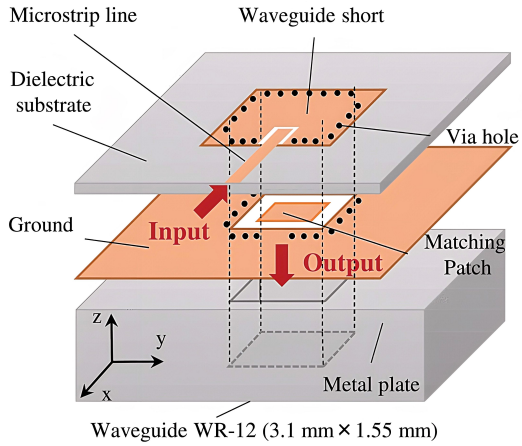

Figure 3.10: Configuration of the proposed microstrip-to-waveguide transition [76].

microstrip probe. A couple of parasitic patches are placed closely to the probe in order to achieve broadband matching.

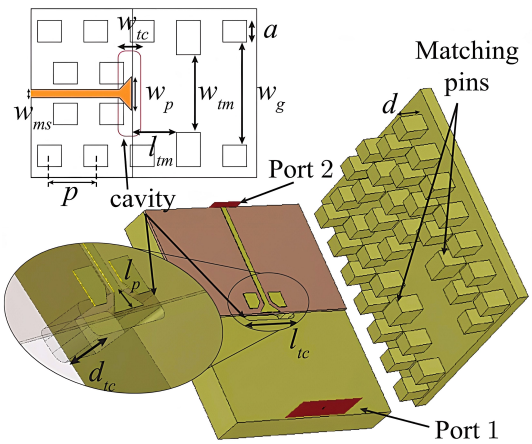

Figure 3.11: Configuration of the proposed microstrip-to-waveguide in-line transition [33].

For vertical microstrip-to-waveguide transitions, gap waveguide is able to address the severe assembly problem at mmWave frequency band. The previous discussion on vertical

transitions has shown that significant board space is occupied by metalized vias. The assembly demands electrical contact between the waveguide block and elevated ground plane. It is of high risk that EM fields are leaking through the possible air gap, particularly at mmWave frequency band. Gap waveguide features non-galvanic contact between the layers, while preventing the field from leaking through the gap. In [77], three vertical transitions from microstrip to double ridge waveguide are presented as shown in Fig. 3.12. The transitions are considered as broadside E-plane transition. The transitions are implemented by microstrip patches with double ridge sections placed on top. Fringe fields of the patches are able to be vertically coupled to the double ridge as shown in Fig. 3.13. Metalized vias no longer appear since the periodic pins are able to stop the field from propagating through the substrate. Even though the transitions are placed in close proximity, it is still able to obtain high isolation thanks to the gap waveguide packaging structure. The transitions are able to be implemented on single layer PCB.

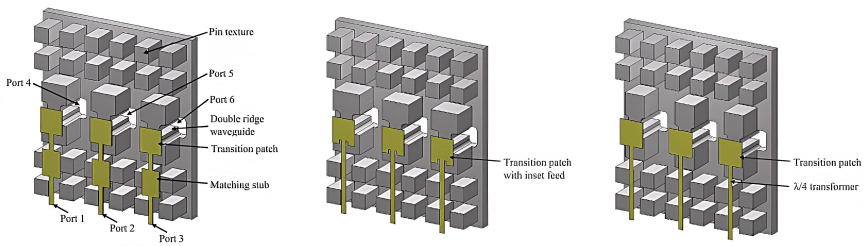

(a) Type 1 (b) Type 2 (c) Type 3

Figure 3.12: Structures of the proposed microstrip to double ridge waveguide transitions. In these figures, substrate and ground layer of microstrip lines are not shown [77].

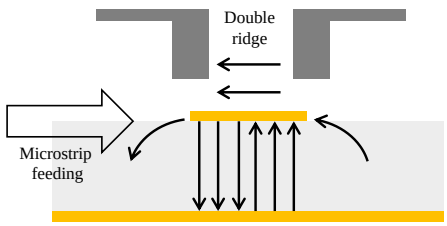

Figure 3.13: Electric field distribution surround the patch.

In [78], a vertical microstrip-to-waveguide transition based on defected ground slot is presented. The T-shape microstrip probe is able to excite ridge gap waveguide modes by a ground slot, as shown in Fig. 3.14. The proposed design features a broadband matching

due to the direct field coupling from microstrip to ridge gap waveguide. Even though the transition is able to be implemented in single layer PCB, the ridge gap waveguide is placed underneath the microstrip, makes the transition not applicable for multi-layer PCB design.

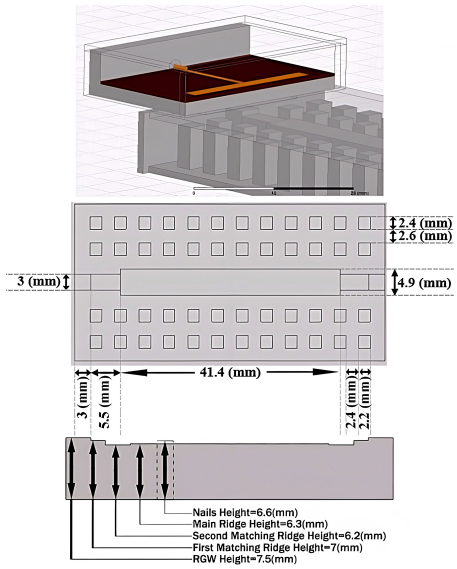

Figure 3.14: Illustration of the proposed vertical microstrip-to-waveguide transition based on defected ground slot [78].

For radar front-end integration with gap waveguide antenna, vertical transitions from microstrip line to ridge gap waveguide are of high interest. In this thesis, two such transitions have been presented. The transitions have been validated in both passive and active configuration. For more details, please refer to appended **Paper A** and **Paper B**.

CHAPTER 4

Summary of included papers

This chapter provides a summary of the included papers.

4.1 Paper A

Qiannan Ren, Ashraf Uz Zaman, Jian Yang, Vessen Vassilev, Carlo Bencivenni
Millimeter-Wave Vertical Transitions Between Ridge Gap Waveguides and Microstrip Lines for Integration of MMIC with Slot Array
2021 15th European Conference on Antennas and Propagation (EuCAP), 2021, pp. 1-4.
 DOI: 10.23919/EuCAP51087.2021.9411273.

This paper presents the simulate results of two low-loss vertical transitions between ridge gap waveguides and microstrip lines. Both vertical transitions feature microstrip lines being the bottom layer but facing opposite directions. The first vertical transition consists of a microstrip line facing upwards with a patch at the end. The second transition of microstrip line facing downwards features E-plane probe with back-short cavity surrounded by periodic pins.

4.2 Paper B

Qiannan Ren, Ashraf Uz Zaman, Jian Yang, Vessen Vassilev, Carlo Bencivenni
Novel Integration Techniques for Gap Waveguides and MMICs Suitable for Multilayer

Waveguide Applications
Accepted by IEEE Transactions on Microwave Theory and Techniques.

Two vertical transitions for integration of RGW with MMICs and one novel packaging structure for integration of IMGW with MMICs have been presented in this chapter. The first vertical transition utilizes rectangular microstrip patch to couple the signal to RGW. Measurement results of the transition in a back-to-back structure show that the reflection coefficient is better than -10 dB from 75 to 83 GHz and the insertion loss for an exclusive transition over the frequency band is 0.65 to 0.85 dB. The second vertical transition utilizes a microstrip probe with a ground slot. Measurement results of the second transition in a back-to-back structure show that the reflection coefficient is better than -10 dB from 69 to 86 GHz and the insertion loss for an exclusive transition is 0.65 to 1 dB over the frequency band. Commercial MMIC amplifiers have been integrated with the RGW using the two vertical transitions. The measured results of the integrated MMICs show good performance in terms of small signal gain and bandwidth. The integration of IMGW with MMIC has been realized by utilizing the bond wires and capacitive pads. The measured results show that the amplifier integrated with IMGW has reflection coefficient better than -10 dB and small signal gain larger than 19.5 dB from 73 to 82 GHz.

4.3 Paper C

Qiannan Ren, Ashraf Uz Zaman, Jian Yang
A Dual Circularly Polarized Array Antenna for Ka-Band Satellite Communications
2021 International Symposium on Antennas and Propagation (ISAP), 2021, pp. 1-2.
 DOI: 10.23919/ISAP47258.2021.9614491.

A dual circularly polarized 8-by-8 array antenna for satellite communications has been proposed in this work. The design consists of five metal layers, including two feeding layers and a polarizer layer that utilize two sector cavities as phase delay elements for each sub-array. Simulated results of the array antenna have shown that the axial ratios are less than 1 dB from 29 to 31 GHz for both polarizations. It also shows good performance in terms reflection coefficients and isolation.

4.4 Paper D

Qiannan Ren, Ashraf Uz Zaman, Jian Yang
Dual-Circularly Polarized Array Antenna Based on Gap Waveguide Utilizing Double-grooved Circular Waveguide Polarizer
Accepted by IEEE Transactions on Antennas and Propagation.

In this chapter, a dual-circularly polarized array antenna based on gap waveguide technology operating at E band has been introduced. The array antenna uses double-grooved circular waveguide polarizer that has two sector grooves placed at 45° and 135° offset from both excitation ports respectively. The operating principles of the polarizer have been presented. Multi-layer design using gap waveguide has been implemented based on the polarizer. A 2×2 unit cell has been presented firstly and optimized for input matching

and axial ratios. Then, a 8×8 planar array has been realized. The antenna consists of six layers, including three layers for the feeding networks, one layer for the polarizer, one layer of back cavity and another layer of radiating grid. Corporate feeding networks using folded E-plane T-junctions and H-plane T-junctions have been presented. The antenna has been fabricated and verified by measurements. The measured results of S-parameters agree well with the simulation and show that reflection coefficients are better than -10 dB for both circular polarizations from 76 to 81 GHz. The measured isolation between the input ports is larger than 25 dB from 76 to 81 GHz. The far-field measurements show that the antenna has realized gain larger than 24 dBi and axial ratios less than 1.5 dB from 76 to 81 GHz.

CHAPTER 5

Future Works

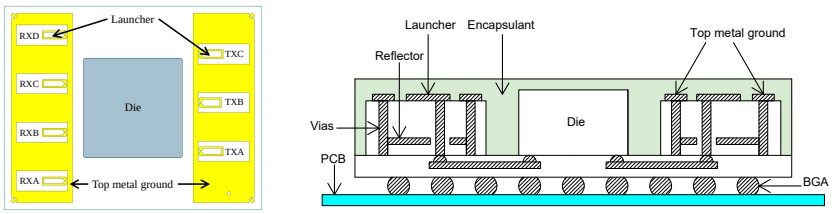

(a) **(b)**

Figure 5.1: LiP transceiver equipped with 4 RXs and 3 TXs: (a) layout of the top metal layer; (b) sectional view of the transceiver [79]

.

1. In general, to connect the radar transceivers to waveguide antennas, intermediate transitions on board are indispensable. Additional loss and board space consumption of the transitions result in a cumbersome design. Hence, SiP components with waveguide interfaces that are able to connect waveguide antennas directly have been investigated lately [80]. As depicted in Fig. 5.1, such packaging technologies are referred to as launcher in package (LiP) [79]. The waveguide transitions, here named as waveguide launchers, are realized inside the SiP component. The highly integrated

scheme of LiP leads to compact designs with low loss and high reliability by eliminating the external waveguide transitions. One of the future works will focus on automotive radar front-end with LiP technology.

2. Polarimetric MIMO systems for automotive radar applications will be investigated using commercial radar transceivers. Antenna systems using dual circular polarizations on receiving side and single circular polarization on transmitting side will be developed. The work involves antenna design, RF front-end, as well as signal processing.

References

[1] S. International, *Automated driving levels of driving automation are defined in new sae international standard j3016*, 2014.

[2] J. Steinbaeck, C. Steger, G. Holweg, and N. Druml, "Next generation radar sensors in automotive sensor fusion systems," in *2017 Sensor Data Fusion: Trends, Solutions, Applications (SDF)*, 2017, pp. 1–6.

[3] F. de Ponte Müller, "Survey on ranging sensors and cooperative techniques for relative positioning of vehicles," *Sensors*, vol. 17, no. 2, p. 271, 2017.

[4] D. J. Yeong, G. Velasco-Hernandez, J. Barry, and J. Walsh, "Sensor and sensor fusion technology in autonomous vehicles: A review," *Sensors*, vol. 21, no. 6, p. 2140, 2021.

[5] Z. Wang, Y. Wu, and Q. Niu, "Multi-sensor fusion in automated driving: A survey," *IEEE Access*, vol. 8, pp. 2847–2868, 2020.

[6] G. Velasco-Hernandez, D. J. Yeong, J. Barry, and J. Walsh, "Autonomous driving architectures, perception and data fusion: A review," in *2020 IEEE 16th International Conference on Intelligent Computer Communication and Processing (ICCP)*, 2020, pp. 315–321.

[7] Continental Automotive, *Short Range Radar – SRR520*, Accessed June 18, 2022.

[8] AutonomouStuff, *Aptiv MRR*, Accessed June 18, 2022.

[9] I. Bilik, S. Villeval, D. Brodeski, *et al.*, "Automotive multi-mode cascaded radar data processing embedded system," in *2018 IEEE Radar Conference (RadarConf18)*, 2018, pp. 0372–0376.

[10] G. F. Hamberger, S. Späth, U. Siart, and T. F. Eibert, "A mixed circular/linear dual-polarized phased array concept for automotive radar-planar antenna designs and system evaluation at 78 GHz," *IEEE Transactions on Antennas and Propagation*, vol. 67, no. 3, pp. 1562–1572, 2019.

[11] W. Menzel and A. Moebius, "Antenna concepts for millimeter-wave automotive radar sensors," *Proceedings of the IEEE*, vol. 100, no. 7, pp. 2372–2379, 2012.

[12] J. R. Huynen, "Phenomenological theory of radar targets," Ph.D. dissertation, Technische Universiteit Delft, Delft, The Netherlands, Dec. 1970.

[13] T. Visentin, "Polarimetric radar for automotive applications," Ph.D. dissertation, Karlsruher Institut für Technologie (KIT), 2019.

[14] O. Auriacombe, V. Vassilev, and N. Pinel, "Dual-polarised radiometer for road surface characterisation," *Journal of Infrared, Millimeter, and Terahertz Waves*, vol. 43, no. 1, pp. 108–124, 2022.

[15] N. Kees and J. Detlefsen, "Road surface classification by using a polarimetric coherent radar module at millimeter waves," in *Proceedings of IEEE National Telesystems Conference - NTC '94*, 1994, pp. 95–98.

[16] V. V. Viikari, T. Varpula, and M. Kantanen, "Road-condition recognition using 24-ghz automotive radar," *IEEE Transactions on Intelligent Transportation Systems*, vol. 10, no. 4, pp. 639–648, 2009.

[17] V. Vassilev, "Road surface recognition at mm-wavelengths using a polarimetric radar," *IEEE Transactions on Intelligent Transportation Systems*, vol. 23, no. 7, pp. 6985–6990, 2022.

[18] S. Trummer, G. F. Hamberger, U. Siart, and T. F. Eibert, "A polarimetrie 76–79 GHz radar-frontend for target classification in automotive use," in *2016 46th European Microwave Conference (EuMC)*, 2016, pp. 1493–1496.

[19] T. Visentin, J. Hasch, and T. Zwick, "Analysis of multipath and doa detection using a fully polarimetric automotive radar," in *2017 European Radar Conference (EURAD)*, 2017, pp. 45–48.

[20] B. J. Donnet and I. D. Longstaff, "MIMO radar, techniques and opportunities," in *2006 European Radar Conference*, 2006, pp. 112–115.

[21] O. Heaviside, *Electromagnetic theory*. Benn brothers, 1922, vol. 3.

[22] L. Rayleigh, "Xviii. on the passage of electric waves through tubes, or the vibrations of dielectric cylinders," *The London, Edinburgh, and Dublin Philosophical Magazine and Journal of Science*, vol. 43, no. 261, pp. 125–132, 1897.

[23] K. Packard, "The origin of waveguides: A case of multiple rediscovery," *IEEE Transactions on Microwave Theory and Techniques*, vol. 32, no. 9, pp. 961–969, 1984.

[24] M. G. Silveirinha, C. A. Fernandes, and J. R. Costa, "Electromagnetic characterization of textured surfaces formed by metallic pins," *IEEE Transactions on Antennas and Propagation*, vol. 56, no. 2, pp. 405–415, 2008.

[25] D. Sievenpiper, L. Zhang, R. Broas, N. Alexopolous, and E. Yablonovitch, "High-impedance electromagnetic surfaces with a forbidden frequency band," *IEEE Transactions on Microwave Theory and Techniques*, vol. 47, no. 11, pp. 2059–2074, 1999.

[26] A. Vosoogh, A. Haddadi, A. U. Zaman, J. Yang, H. Zirath, and A. A. Kishk, "W -band low-profile monopulse slot array antenna based on gap waveguide corporate-feed network," *IEEE Transactions on Antennas and Propagation*, vol. 66, no. 12, pp. 6997–7009, 2018.

[27] J. Liu, A. Vosoogh, A. U. Zaman, and J. Yang, "A slot array antenna with single-layered corporate-feed based on ridge gap waveguide in the 60 GHz band," *IEEE Transactions on Antennas and Propagation*, vol. 67, no. 3, pp. 1650–1658, 2019.

[28] M. Sharifi Sorkherizi, A. Dadgarpour, and A. A. Kishk, "Planar high-efficiency antenna array using new printed ridge gap waveguide technology," *IEEE Transactions on Antennas and Propagation*, vol. 65, no. 7, pp. 3772–3776, 2017.

[29] A. Dadgarpour, N. Bayat-Makou, M. A. Antoniades, A. A. Kishk, and A. Sebak, "A dual-polarized magnetoelectric dipole array based on printed ridge gap waveguide with dual-polarized split-ring resonator lens," *IEEE Transactions on Antennas and Propagation*, vol. 68, no. 5, pp. 3578–3585, 2020.

[30] J. Liu, A. Vosoogh, A. U. Zaman, and J. Yang, "Design and fabrication of a high-gain 60-GHz cavity-backed slot antenna array fed by inverted microstrip gap waveguide," *IEEE Transactions on Antennas and Propagation*, vol. 65, no. 4, pp. 2117–2122, 2017.

[31] A. K. Horestani and M. Shahabadi, "Balanced filter with wideband common-mode suppression in groove gap waveguide technology," *IEEE Microwave and Wireless Components Letters*, vol. 28, no. 2, pp. 132–134, 2018.

[32] A. Vosoogh, M. S. Sorkherizi, A. U. Zaman, J. Yang, and A. A. Kishk, "An integrated Ka-band diplexer-antenna array module based on gap waveguide technology with simple mechanical assembly and no electrical contact requirements," *IEEE Transactions on Microwave Theory and Techniques*, vol. 66, no. 2, pp. 962–972, 2018.

[33] A. Vosoogh, M. Sharifi Sorkherizi, V. Vassilev, *et al.*, "Compact integrated full-duplex gap waveguide-based radio front end for Multi-Gbit/s point-to-point backhaul links at E-band," *IEEE Transactions on Microwave Theory and Techniques*, vol. 67, no. 9, pp. 3783–3797, 2019.

[34] E. Rajo-Iglesias, M. Ferrando-Rocher, and A. U. Zaman, "Gap waveguide technology for millimeter-wave antenna systems," *IEEE Communications Magazine*, vol. 56, no. 7, pp. 14–20, 2018.

[35] A. Vosoogh, P.-S. Kildal, and V. Vassilev, "A multi-layer gap waveguide array antenna suitable for manufactured by die-sink EDM," in *2016 10th European Conference on Antennas and Propagation (EuCAP)*, 2016, pp. 1–4.

[36] Á. Palomares-Caballero, A. Alex-Amor, J. Valenzuela-Valdés, and P. Padilla, "Millimeter-wave 3-D-printed antenna array based on gap-waveguide technology and split E-plane waveguide," *IEEE Transactions on Antennas and Propagation*, vol. 69, no. 1, pp. 164–172, 2021.

[37] S. Farjana, M. Ghaderi, A. U. Zaman, *et al.*, "Realizing a 140 GHz gap waveguide–based array antenna by low-cost injection molding and micromachining," *Journal of Infrared, Millimeter, and Terahertz Waves*, vol. 42, no. 8, pp. 893–914, 2021, ISSN: 1866-6906.

[38] S. Farjana, M. Ghaderi, A. U. Zaman, S. Rahiminejad, P. Lundgren, and P. Enoksson, "Low-loss gap waveguide transmission line and transitions at 220–320 GHz using dry film micromachining," *IEEE Transactions on Components, Packaging and Manufacturing Technology*, vol. 11, no. 11, pp. 2012–2021, 2021.

[39] A. Tamayo-Domínguez, J.-M. Fernández-González, and M. Sierra-Pérez, "Groove gap waveguide in 3-d printed technology for low loss, weight, and cost distribution networks," *IEEE Transactions on Microwave Theory and Techniques*, vol. 65, no. 11, pp. 4138–4147, 2017.

[40] J. Hasch, E. Topak, R. Schnabel, T. Zwick, R. Weigel, and C. Waldschmidt, "Millimeter-wave technology for automotive radar sensors in the 77 ghz frequency band," *IEEE Transactions on Microwave Theory and Techniques*, vol. 60, no. 3, pp. 845–860, 2012.

[41] B.-H. Ku, O. Inac, M. Chang, H.-H. Yang, and G. M. Rebeiz, "A high-linearity 76–85-ghz 16-element 8-transmit/8-receive phased-array chip with high isolation and flip-chip packaging," *IEEE Transactions on Microwave Theory and Techniques*, vol. 62, no. 10, pp. 2337–2356, 2014.

[42] M. Shih, C.-Y. Huang, T.-H. Chen, C.-C. Wang, D. Tarng, and C. P. Hung, "Electrical, thermal, and mechanical characterization of eWLB, fully molded fan-out package, and fan-out chip last package," *IEEE Transactions on Components, Packaging and Manufacturing Technology*, vol. 9, no. 9, pp. 1765–1775, 2019.

[43] J. Xu, W. Hong, H. Zhang, G. Wang, Y. Yu, and Z. H. Jiang, "An array antenna for both long- and medium-range 77 ghz automotive radar applications," *IEEE Transactions on Antennas and Propagation*, vol. 65, no. 12, pp. 7207–7216, 2017.

[44] B.-H. Ku, P. Schmalenberg, O. Inac, *et al.*, "A 77–81-ghz 16-element phased-array receiver with $\pm 50^\circ$ beam scanning for advanced automotive radars," *IEEE Transactions on Microwave Theory and Techniques*, vol. 62, no. 11, pp. 2823–2832, 2014.

[45] J. Schoepfel, S. Kueppers, K. Aufinger, and N. Pohl, "A sige transceiver chipset for automotive radar applications using wideband modulation sequences," *International Journal of Microwave and Wireless Technologies*, vol. 11, no. 7, pp. 676–685, 2019.

[46] J.-H. Lee, J. M. Lee, K. C. Hwang, D.-W. Seo, D. Shin, and C. Lee, "Capacitively coupled microstrip comb-line array antennas for millimeter-wave applications," *IEEE Antennas and Wireless Propagation Letters*, vol. 19, no. 8, pp. 1336–1339, 2020.

[47] RFbeam Microwave Gmbh, *MR2001_RD Radar Transceiver*, Accessed June 30, 2022.

[48] NXP Semiconductors, *S32R274 End-to-End Reference Design Kit*, Accessed June 18, 2022.

[49] RFbeam Microwave Gmbh, *K-MD2 Engineering Sample*, Accessed June 30, 2022.

[50] Texas Instruments, *MMWCAS-RF-EVM mmWave cascade imaging radar RF evaluation module*, Accessed June 18, 2022.

[51] Y. Zhao and K.-M. Luk, "Dual circular-polarized SIW-fed high-gain scalable antenna array for 60 GHz applications," *IEEE Transactions on Antennas and Propagation*, vol. 66, no. 3, pp. 1288–1298, 2018.

[52] Y. J. Cheng, J. Wang, and X. L. Liu, "94 GHz substrate integrated waveguide dual-circular-polarization shared-aperture parallel-plate long-slot array antenna with low sidelobe level," *IEEE Transactions on Antennas and Propagation*, vol. 65, no. 11, pp. 5855–5861, 2017.

[53] G. F. Hamberger, U. Siart, and T. F. Eibert, "A dual-linearly polarized receive antenna array for digital beamforming in automotive use," in *2017 IEEE Asia Pacific Microwave Conference (APMC)*, 2017, pp. 17–20.

[54] W. Zhang, N. Li, J. Yu, and E. Kasper, "A compact single-board solution for commercializing cost-effective 77 GHz automotive front radar," in *2020 IEEE Asia-Pacific Microwave Conference (APMC)*, 2020, pp. 1098–1100.

[55] A. Haddadi, C. Bencivenni, and T. Emanuelsson, "Gap waveguide slot array antenna for automotive applications at E-band," in *2019 13th European Conference on Antennas and Propagation (EuCAP)*, 2019, pp. 1–4.

[56] F. Jansen, F. Laghezza, S. Alhasson, *et al.*, "Simultaneous multi-mode automotive imaging radar using cascaded transceivers," in *2021 18th European Radar Conference (EuRAD)*, 2022, pp. 441–444.

[57] T. Visentin, J. Hasch, and T. Zwick, "Calibration of a fully polarimetric 8×8 mimo fmcw radar system at 77 ghz," in *2017 11th European Conference on Antennas and Propagation (EUCAP)*, 2017, pp. 2530–2534.

[58] M. Ferrando-Rocher, J. I. Herranz-Herruzo, A. Valero-Nogueira, and B. Bernardo-Clemente, "Dual circularly polarized aperture array antenna in gap waveguide for high-efficiency Ka-band satellite communications," *IEEE Open Journal of Antennas and Propagation*, vol. 1, pp. 283–289, 2020.

[59] G. Montisci, "Design of circularly polarized waveguide slot linear arrays," *IEEE Transactions on Antennas and Propagation*, vol. 54, no. 10, pp. 3025–3029, 2006.

[60] V. Ravindra, P. R. Akbar, M. Zhang, J. Hirokawa, H. Saito, and A. Oyama, "A dual-polarization X -band traveling-wave antenna panel for small-satellite synthetic aperture radar," *IEEE Transactions on Antennas and Propagation*, vol. 65, no. 5, pp. 2144–2156, 2017.

[61] C. Shu, J. Wang, S. Hu, *et al.*, "A wideband dual-circular-polarization horn antenna for mmWave wireless communications," *IEEE Antennas and Wireless Propagation Letters*, vol. 18, no. 9, pp. 1726–1730, 2019.

[62] J. Wu, Y. J. Cheng, H. B. Wang, Y. C. Zhong, D. Ma, and Y. Fan, "A wideband dual circularly polarized full-corporate waveguide array antenna fed by triple-resonant cavities," *IEEE Transactions on Antennas and Propagation*, vol. 65, no. 4, pp. 2135–2139, 2017.

[63] N. Yoneda, R. Miyazaki, I. Matsumura, and M. Yamato, "A design of novel grooved circular waveguide polarizers," *IEEE Transactions on Microwave Theory and Techniques*, vol. 48, no. 12, pp. 2446–2452, 2000.

[64] N. Luo, X. Yu, G. Mishra, and S. K. Sharma, "A millimeter-wave (V-band) dual-circular-polarized horn antenna based on an inbuilt monogroove polarizer," *IEEE Antennas and Wireless Propagation Letters*, vol. 19, no. 11, pp. 1933–1937, 2020.

[65] I. Agnihotri and S. K. Sharma, "Design of a compact 3-D metal printed Ka-band waveguide polarizer," *IEEE Antennas and Wireless Propagation Letters*, vol. 18, no. 12, pp. 2726–2730, 2019.

[66] C. Shu, S. Hu, X. Cheng, *et al.*, "Wideband dual-circular-polarization antenna with high isolation for millimeter-wave wireless communications," *IEEE Transactions on Antennas and Propagation*, vol. 70, no. 3, pp. 1750–1763, 2022.

[67] U. Balaji and Vahldieck, "Radial mode matching analysis of ridged circular waveguides," *IEEE Transactions on Microwave Theory and Techniques*, vol. 44, no. 7, pp. 1183–1186, 1996.

[68] U. Balaji and R. Vahldieck, "Radial mode matching analysis of ridged circular waveguide," in *Proceedings of 1995 IEEE MTT-S International Microwave Symposium*, 1995, 637–640 vol.2.

[69] J. Böck, M. Wojnowski, C. Wagner, *et al.*, "Low-cost ewlb packaging for automotive radar mmics in the 76–81 ghz range," *International Journal of Microwave and Wireless Technologies*, vol. 5, no. 1, pp. 25–34, 2013.

[70] M. Technology, *Micron BGA manufacturer's user guide*, Accessed June 18, 2022.

[71] H. Winner, S. Hakuli, F. Lotz, and C. Singer, "Handbook of driver assistance systems: Basic information, components and systems for active safety and comfort," *Springer reference*, 2015.

[72] Texas Instruments, *AWR2243BOOST AWR2243 second-generation 76-GHz to 81-GHz high-performance automotive MMIC evaluation module*, Accessed June 18, 2022.

[73] Y.-C. Leong and S. Weinreb, "Full band waveguide-to-microstrip probe transitions," in *1999 IEEE MTT-S International Microwave Symposium Digest (Cat. No.99CH36282)*, vol. 4, 1999, 1435–1438 vol.4.

[74] E. Topak, J. Hasch, and T. Zwick, "Compact topside millimeter-wave waveguide-to-microstrip transitions," *IEEE Microwave and Wireless Components Letters*, vol. 23, no. 12, pp. 641–643, 2013.

[75] Y. Ishikawa, K. Sakakibara, Y. Suzuki, and N. Kikuma, "Millimeter-wave topside waveguide-to-microstrip transition in multilayer substrate," *IEEE Microwave and Wireless Components Letters*, vol. 28, no. 5, pp. 380–382, 2018.

[76] N. Thanh Tuan, K. Sakakibara, and N. Kikuma, "Bandwidth extension of planar microstrip-to-waveguide transition by controlling transmission modes through via-hole positioning in millimeter-wave band," *IEEE Access*, vol. 7, pp. 161 385–161 393, 2019.

[77] A. Bagheri, H. Karlsson, C. Bencivenni, A. Haddadi, T. Emanuelsson, and A. A. Glazunov, "Microstrip to ridge gap waveguide transition for 28 GHz steerable slot array antennas," in *2020 14th European Conference on Antennas and Propagation (EuCAP)*, 2020, pp. 1–4.

[78] B. Molaei and A. Khaleghi, "A novel wideband microstrip line to ridge gap waveguide transition using defected ground slot," *IEEE Microwave and Wireless Components Letters*, vol. 25, no. 2, pp. 91–93, 2015.

[79] G. Carluccio, M. B. Vincent, M. Spella, G. A. J. M. De, and S. H. Thippur, "Package," US20220231408A1, 2022.

[80] E. Seler, M. Wojnowski, W. Hartner, *et al.*, "Chip-to-rectangular waveguide transition realized in embedded wafer level ball grid array (eWLB) package," in *WAMICON 2014*, 2014, pp. 1–4.

Part II

Papers

PAPER A

Millimeter-Wave Vertical Transitions Between Ridge Gap Waveguides and Microstrip Lines for Integration of MMIC with Slot Array

Qiannan Ren, Ashraf Uz Zaman, Jian Yang, Vessen Vassilev, Carlo Bencivenni

2021 15th European Conference on Antennas and Propagation (EuCAP), 2021, pp. 1-4.
 DOI: 10.23919/EuCAP51087.2021.9411273

The layout has been revised.

Abstract

This paper presents two low-loss vertical transitions between ridge gap waveguides and microstrip lines. The transitions can be utilized as packaging techniques for system level integration of MMICs with waveguide components such as slot array antennas. Both vertical transitions feature microstrip lines being the bottom layer but facing opposite directions. The first vertical transition consists of a microstrip line facing upwards with a patch in the end. Simulation results show that the reflection coefficient is better than -15 dB from 74 to 82 GHz. The second transition of microstrip line facing downwards features E-plane probe with back-short cavity surrounded by periodic pins. Simulation results show that the reflection coefficient is better than -15 dB from 71 to 86 GHz. Comparing with other same layer transitions, the vertical solutions provide more flexibility for the routing of antenna feeding line and have the ability of implementing a more compact design.

1 Introduction

Gap wave technology has the potential to become more cost-effective than conventional rectangular waveguide and more power-efficient than PCB-based microstrip and coplanar waveguide for communication and radar applications in mm-wave frequency bands [1], [2]. Passive gap waveguide components, like filters and diplexers, have been realized successfully [3], [4]. Also, several low-loss and high-gain gap waveguide based planar antennas have been demonstrated at mm-wave frequency [5]–[6]. Moreover, system-level packaging solutions based on gap waveguide technology have been investigated in [7]. It has been shown that gap waveguide technology has promising performance in antennas and mm-wave passive networks, as well as system-level packaging. In most cases, gap waveguide antennas consist of feeding layer and radiating layer, and microstrip lines are commonly used for integration of active components. Thus, a direct transition from microstrip to the antenna feeding layer is of high interest. The integration of active components with passive gap waveguide devices has been introduced in [7]–[8]. However, such integrations are within the scope of same-layer solution, which makes the layout of active components, as well as the routing of antenna feeding line more challenging and complex. To have a more compact and efficient solution, especially for mm-wave automotive radar system-level integration, this paper presents two cross-layer vertical transitions between microstrip and gap waveguide transmission line.

2 Design of the transitions

Two configurations of vertical transitions between ridge gap waveguide and microstrip line have been proposed in this work, as shown in Fig. 1. Both configurations feature bottom layer being microstrip line but towards opposite directions.

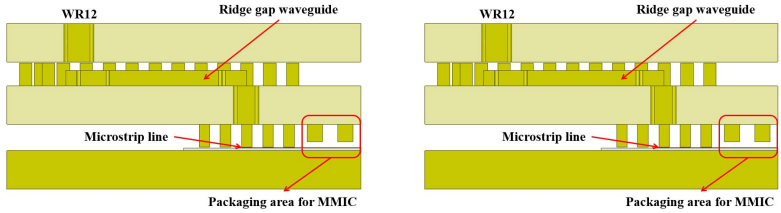

(a) Configuration A: microstrip line facing upwards

(b) Configuration B: microstrip line facing downwards

Figure 1: Configurations of vertical transitions between ridge gap waveguide and microstrip line.

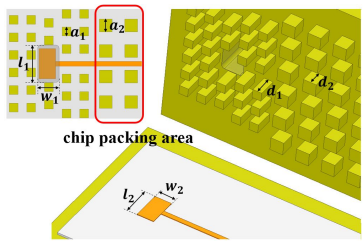

Figure 2: Vertical transition between packaged microstrip and rectangular waveguide in configuration A. ($a_1 = 0.55$ mm, $d_1 = 1.2$ mm, $a_2 = 0.8$ mm, $d_2 = 0.9$ mm, $l_1 = 2.33$ mm, $w_1 = 1.34$ mm, $l_2 = 1.89$ mm, $w_2 = 1.04$ mm)

2.1 Configuration A

Vertical transition between microstrip line and waveguide is one of the candidates for integration of slot array with MMICs which have microstrip outputs. Conventionally, a back-short cavity is necessary for the typical vertical transition between microstrip line and waveguide. This brings complexity for manufacturing in mm-wave frequency band. Instead of using E-plane probe, resonant patch coupling has been proposed in this work without the presence of back-short cavity, as shown in Fig. 2. Periodic pins on the top plate have formed a specific cavity above the patch fed by input microstrip line. The resonance from the cavity and the resonance from the microstrip patch have been carefully optimized for efficient coupling of EM signal from the microstrip line to the top cavity. The MMICs will be packaged by pins with different dimensions which are able to block interference signals and bring favorable space for assembly. To reduce the sensitivity of resonance resulting from manufacturing and assembly tolerance, zero-gap waveguide has been utilized in this work [9].

Ridge gap waveguide is more commonly used than groove gap waveguide in mm-wave

antenna design as a result of more wideband and compact properties. A probe transition between ridge gap waveguide and conventional rectangular waveguide has been proposed, as shown in Fig. 3.

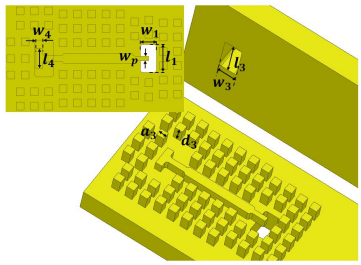

Figure 3: Vertical transition between ridge gap waveguide and rectangular waveguide in configuration A. ($w_3 = 1.55$ mm, $l_3 = 3.1$ mm, $a_3 = 0.65$ mm, $d_3 = 1.2$ mm, $w_4 = 0.57$ mm, $l_4 = 1.7$ mm, $w_p = 0.39$ mm)

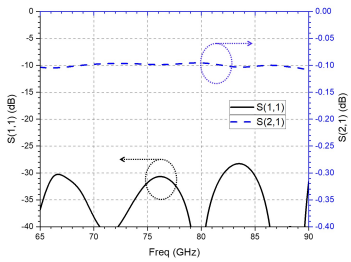

Figure 4: Simulation results of vertical transition between ridge gap waveguide and standard WR12 rectangular waveguide.

A transition between standard WR12 rectangular waveguide and ridge gap waveguide is necessary as well in practice, as shown in Fig. 3. The simulation results of this transition implemented in a back-to-back structure is shown in Fig. 4. The reflection coefficient is around -30 dB from 65 to 90 GHz.

The microstrip line used in this design is based on 0.127 mm Rogers 3003 substrate and length of the line is 6.1 mm. The simulation results of configuration A are shown in Fig. 5. The reflection coefficient is better than -15 dB from 74 to 82 GHz. The insertion loss, including the piece of microstrip line and a piece of ridge gap waveguide with length of 5.7 mm, is around 0.5 dB from 74 to 82 GHz.

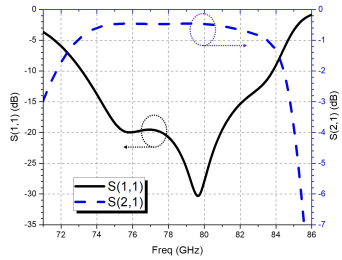

Figure 5: Simulation results of the vertical transition of configuration A.

2.2 Configuration B

In the previous section, the vertical transition of microstrip line facing upwards has been introduced. However, due to the patch resonance, the transition of configuration A is inherently narrow band. In this section, a broadband solution of microstrip line facing downwards is presented.

A probe transition between microstrip line and rectangular waveguide is shown in Fig. 6. Utilizing the packaging pins on top of the microstrip line, a back-short cavity has been employed for the broadside probe transition. By the ground slot of the microstrip line, EM signal could be coupled vertically up to the rectangular waveguide. The same transition that couples the EM signal from the rectangular waveguide to the ridge gap waveguide has been utilized here, as shown in Fig. 7.

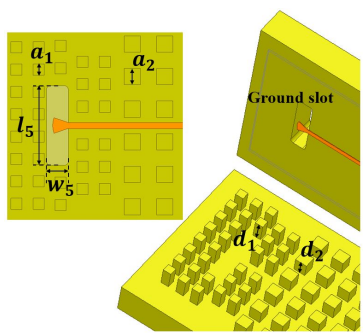

Figure 6: Probe transition between microstrip and rectangular waveguide in configuration B. ($w_5 = 1.08$ mm, $l_5 = 3.92$ mm)

The simulation results of configuration B are shown in Fig. 8. The length of the microstrip line utilized in the transition is 5.57 mm. The transition features a reflection coefficient better than -15 dB and an insertion loss approximately 0.4 dB, including the piece of microstrip line and a piece of ridge gap waveguide with length of 5 mm, over the frequency

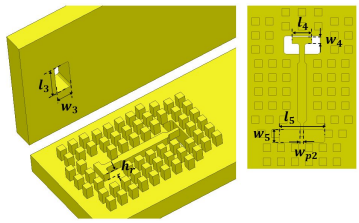

Figure 7: Vertical transition between ridge gap waveguide and rectangular waveguide in configuration B. ($w_{p2} = 0.3$ mm, $h_r = 0.8$ mm)

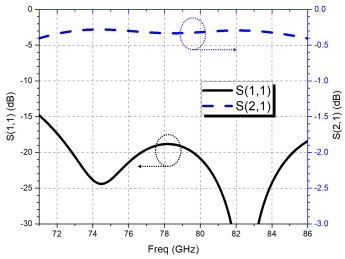

Figure 8: Simulation results of the vertical transition of configuration B.

band from 71 to 86 GHz.

Comparing with the transition of configuration A, the transition of configuration B has advantages of wider bandwidth and lower insertion loss. However, in system-level design, if the PCB board to be integrated is of multi-layer, it would be difficult to have a waveguide window underneath the RF layer. This makes the vertical transition of configuration A, a transition without the presence of back short cavity, a better candidate for integration of multi-layer PCB boards.

3 Conclusion

Two vertical transitions between microstrip line and ridge gap waveguide have been presented in this paper. The first transition design with microstrip line facing upwards utilizes resonant patch to couple the signal from microstrip to the ridge gap waveguide. It can be observed from the simulation results that the reflection coefficient is better than -15 dB from 74 to 82 GHz and the insertion loss is around 0.5 dB from 74 to 82 GHz. The second transition design with microstrip line facing downwards utilizes microstrip probe in the presence of back-short cavity. The simulation results show that the reflection coefficient is better than -15 dB from 71 to 86 GHz and insertion loss is approximately 0.4 dB from 71 to 86 GHz. The two proposed transitions have novel vertical structures that will make

the integration of gap waveguide slot array with MMICs more compact and more flexible for the system layout.

Acknowledgment

The authors would like to thank Olof Eriksson and Konstantinos Konstantinidis from Veoneer Sweden, Robert Moestam and Bo Wendemo from CEVT for their support and discussion during this project. This work is supported by Swedish Strategic Vehicle Research and Innovation FFI grant 2018-02707.

References

[1] E. Rajo-Iglesias, M. Ferrando-Rocher, and A. U. Zaman, "Gap waveguide technology for millimeter-wave antenna systems," *IEEE Communications Magazine*, vol. 56, no. 7, pp. 14–20, 2018.

[2] E. Rajo-Iglesias, Z. Sipus, and A. U. Zaman, "Gap waveguide technology," in *Surface electromagnetics : with applications in antenna, microwave, and optical engineering*, F. Yang and Y. Rahmat-Samii, Eds., Cambridge University Press, 2019, pp. 198–230.

[3] A. Vosoogh, M. S. Sorkherizi, A. U. Zaman, J. Yang, and A. A. Kishk, "An integrated Ka-band diplexer-antenna array module based on gap waveguide technology with simple mechanical assembly and no electrical contact requirements," *IEEE Transactions on Microwave Theory and Techniques*, vol. 66, no. 2, pp. 962–972, 2018.

[4] M. Rezaee, A. U. Zaman, and P.-S. Kildal, "V-band groove gap waveguide diplexer," in *2015 9th European Conference on Antennas and Propagation (EuCAP)*, 2015, pp. 1–4.

[5] A. Vosoogh, A. Haddadi, A. U. Zaman, J. Yang, H. Zirath, and A. A. Kishk, "W -band low-profile monopulse slot array antenna based on gap waveguide corporate-feed network," *IEEE Transactions on Antennas and Propagation*, vol. 66, no. 12, pp. 6997–7009, 2018.

[6] J. Liu, A. Vosoogh, A. U. Zaman, and J. Yang, "Design and fabrication of a high-gain 60-GHz cavity-backed slot antenna array fed by inverted microstrip gap waveguide," *IEEE Transactions on Antennas and Propagation*, vol. 65, no. 4, pp. 2117–2122, 2017.

[7] A. Vosoogh, M. Sharifi Sorkherizi, V. Vassilev, *et al.*, "Compact integrated full-duplex gap waveguide-based radio front end for Multi-Gbit/s point-to-point backhaul links at E-band," *IEEE Transactions on Microwave Theory and Techniques*, vol. 67, no. 9, pp. 3783–3797, 2019.

[8] U. Nandi, A. U. Zaman, A. Vosoogh, and J. Yang, "Novel millimeter wave transition from microstrip line to groove gap waveguide for MMIC packaging and antenna integration," *IEEE Microwave and Wireless Components Letters*, vol. 27, no. 8, pp. 691–693, 2017.

[9] A. Vosoogh, A. Uz Zaman, V. Vassilev, and J. Yang, "Zero-gap waveguide: A parallel plate waveguide with flexible mechanical assembly for mm-Wave antenna applications," *IEEE Transactions on Components, Packaging and Manufacturing Technology*, vol. 8, no. 12, pp. 2052–2059, 2018.

PAPER B

Novel Integration Techniques for Gap Waveguides and MMICs Suitable for Multilayer Waveguide Applications

Qiannan Ren, Ashraf Uz Zaman, Jian Yang, Vessen Vassilev, Carlo Bencivenni

Accepted by IEEE Transactions on Microwave Theory and Techniques

The layout has been revised.

Abstract

This paper discusses three integration and packaging techniques for gap waveguides and MMICs suitable for multilayer waveguide applications. Two vertical transitions between microstrips and ridge gap waveguides are presented. The first vertical transition connects ridge gap waveguide to a microstrip line from the top where a rectangular patch has been used. Measured results of the transition in a back-to-back structure show that the reflection coefficient is better than -10 dB from 75 to 83 GHz and the insertion loss for a single transition over the frequency band is 0.65 to 0.85 dB. The second vertical transition connects ridge gap waveguide to a microstrip line from the back by a slot in the ground plane. Measured results of the transition in a back-to-back structure show that the reflection coefficient is better than -10 dB from 69 to 86 GHz and the insertion loss for a single transition is 0.65 to 1 dB over the frequency band. Commercially available E-band MMIC amplifiers are integrated with ridge gap waveguides using the two proposed transitions. Moreover, for the very first time, the integration of MMIC with inverted microstrip gap waveguide is realized by a compact packaging structure that utilizes bond wires and capacitive pads. All the three active integrations are consistent with the passive measurements in terms of operational bandwidth, losses, amplifier gain flatness and unwanted resonance suppression.

Index Terms: ridge gap waveguide, inverted microstrip gap waveguide, millimeter wave, MMIC, integration, packaging, transition.

1 Introduction

Integration of passive waveguide components with active circuits plays an important role in system level integration of millimeter wave front-end. For conventional circuits that demand bond wires for assembly, such integrations are typically realized by using substrate based planar transmission lines as intermediate transitions. For integrations with conventional waveguide components, these intermediate transitions tend to be bulky and lack of compatibility for multi-layer designs [1]–[4]. One of the reasons is that the necessity of electrical contact between the layers bring about challenges in the assembly. Besides, significant board areas are needed to accommodate rows of metalized vias and copper strips around the transition area in the substrate to make sure that the waveguide block comes in perfect contact with the elevated substrate ground plane, as shown in Fig. 1. Otherwise, EM wave will start leaking from the discontinuity area. However, this electric contact is very tricky at mmWave frequency range. Unwanted leakage due to imperfect electric contact is even more critical in case of waveguide based active beam scanning antenna array or multi-layer MIMO array where several such transitions are used in close proximity and this can degrade the electrical performance of the array due to significantly higher level of mutual coupling among adjacent chains [5]. To overcome such integration challenges, new types of microstrip to waveguide transitions need to be investigated.

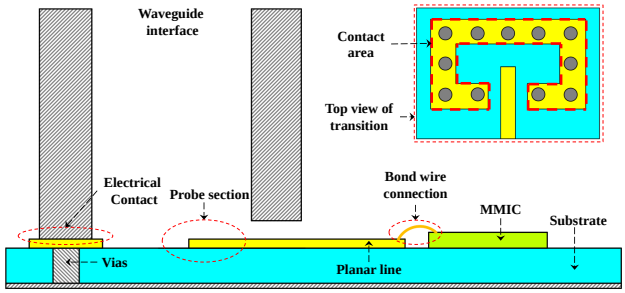

Figure 1: Typical integration of active circuits with conventional waveguide

In this respect, several integration techniques based on gap waveguide technology are presented in this work. The proposed transitions do not suffer from the above mentioned electric contact issues. Several multi-layer waveguide components based on gap waveguide such as slot arrays, filters and diplexers, have been widely discussed [6]–[12]. It has been shown that gap waveguide based components have competitive performance compared with conventional waveguide based components. Moreover, gap waveguide technology brings more flexibility to the design of interconnections between the layers, as well as the ability of integration with other components. Gap waveguide technology has been investigated for system level integration of millimeter wave front-end as well [13]. Gap waveguide integration is a multi-layer integration technique which features the advantages of non-galvanic contact between the layers, thereby ensure higher reliability of assembly, and robustness of the entire system[14].

Automotive radar systems have been widely investigated for driving assistance applications [15], [16]. In general, there are two main frequency bands for automotive radars, 24-GHz band and 77-GHz band. Due to the larger bandwidth and smaller antenna size, 76 to 81 GHz is a better option despite the difficulties of antenna fabrication at higher frequencies. Microstrip patch arrays and substrate integrated waveguide (SIW) are the most commonly used antennas for automotive radar systems [17], [18]. However, the dielectric losses in the substrate cause deterioration of the radiation efficiency. In addition, material properties along with the environment condition, such as temperature and humidity, are critical for the functionality and reliability of systems [19]. Therefore, gap waveguide based solutions for such radar front-ends are getting more and more attention, as a result of the antenna with high efficiency and the ability for integration [20].

Traditionally, CNC milling is used for the fabrication of the gap waveguide components, the manufacturing cost is increasing due to the small features and time-consuming fabrication. Recently, more and more low cost techniques have been adopted for gap waveguide manufacturing, such as die-sink Electric Discharge Machining (EDM), 3D printing, plastic injection molding and micro-machining [21]–[23]. Therefore, needs for expensive manufacturing and precise mechanical assembly are avoided for gap waveguide components at millimeter wave frequency band.

Most of the commercial monolithic microwave integrated circuits (MMIC) operating at

77 GHz band have microstrip line outputs. The RF ports of highly integrated transceivers with ball grid arrays (BGA) need to transform from solder balls to microstrip as well. Therefore, transitions from microstrip line to gap waveguide transmission line is of high interest. Several designs have been proposed for such transitions. However, most of them are within the scope of inline transitions. In [24], an inline transition between groove gap waveguide (GGW) and microstrip line has been presented at V band. The transition uses a microstrip probe with the presence of back-short cavity. Similar transition is also utilized in [13] at E band. Another inline transition between GGW and microstrip is proposed at W band in [25]. The transition is based on a microstrip probe equipped with a shorting via. In [26], another inline transition between GGW and microstrip with an intermediate Chebyshev transformer is proposed. In [27], an inline transition between ridge gap waveguide (RGW) and microstrip is discussed with an section of SIW in the middle. The inline transitions request the MMIC and gap waveguide transmission line in the same layer, thereby leave limited space for bias signal and LO/IF signal routing. In [28], a vertical transition from RGW to microstrip line using the ground slot of the microstrip has been proposed. In [29], one example of vertical transitions from microstrip lines to double ridge waveguides has been presented for 5G millimeter wave phased arrays. In [30], a microstrip line transition to RGW has been described, also using the ground slot of microstrip but from the other side of the RGW which is different from [28].

In this work, two vertical transitions for integration of MMICs with RGW are presented in both passive and active configuration as a further work of [31]. The transitions operate at higher frequency band and have significantly better performance compared to [28]–[30] where only passive structures have been demonstrated. Unlike the inline transitions, the vertical transitions are more compact and flexible when integrating several active components as proposed in [32]. Besides, for the very first time, one novel packaging structure for integration of MMICs with inverted microstrip gap waveguides (IMGW) is proposed by using one wire-bonded capacitive pad to directly couple the signal, the intermediate transitions are no longer needed.

This paper is organized as follows. The two vertical transitions, as well as the integrations of MMICs with RGW are introduced in Section II. The integration of MMICs with IMGW is described in Section III. The measured results of the transitions implemented in back-to-back structures, and the MMICs integrated with RGW and IMGW, are given in Section IV. Finally, a conclusion is given in Section V.

2 Integration with RGW

As a result of wideband performance and compactness in size, RGW is more commonly used than GGW when implementing passive components. Therefore, two vertical transitions between RGW and microstrip lines have been proposed in this work, as shown in Fig. 2. Based on the proposed transitions, the integrations of MMICs with RGW have been realized.

2.1 Transition A

Instead of using conventional E-plane probes, rectangular microstrip patch has been utilized in this work to implement the transitions between microstrip and RGW without the presence

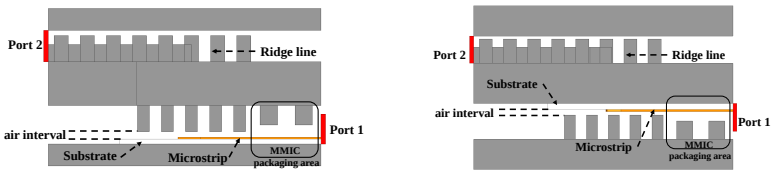

(a) Transition A: microstrip line facing upwards

(b) Transition B: microstrip line facing downwards

Figure 2: Side view of the vertical transitions between RGW and microstrip line.

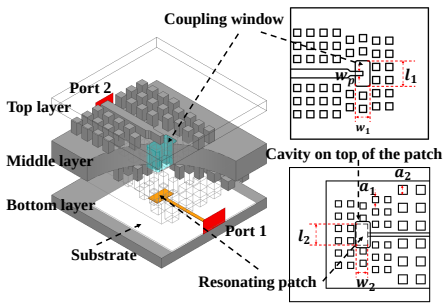

Figure 3: Vertical transition A between packaged microstrip line and RGW. (a_1 = 0.55 mm, a_2 = 0.8 mm, l_1 = 2.33 mm, w_1 = 1.34 mm, l_2 = 1.89 mm, w_2 = 1.04 mm)

of back-short cavity, as shown in Fig. 3. Periodic pins at the backside of the middle layer have formed a specific cavity above the patch fed by the input microstrip line. The electric fields inside the cavity and the substrate are depicted in Fig. 4. The length of patch in y direction (w_2) should be approximately half waveguide wavelength of the microstrip line. This leads to out of phase voltage maximums at the edges of the patch in y direction. Note that the fringe fields near the surface of the patch are both in the $-y$ direction. Hence, the electric fields add up in phase and are able to be coupled vertically up. For the design of transition A, the resonance frequency of the patch is about 83 GHz, as indicated by [33]:

$$f_c \approx \frac{c}{2w_2\epsilon_r} \tag{B.1}$$

The electrical length of the patch is approximately 180 degree at 83 GHz and 160 degree at 74 GHz. This assures that the fringe fields are in-phase in y direction and leads to a more compact design. Size of the cavity above is determined to accommodate the patch. The line impedance of the feeding microstrip line is about 50 Ohm at 77 GHz. The input matching of the ridge line is optimized by the width of the patch (l_2) and the ridge probe.

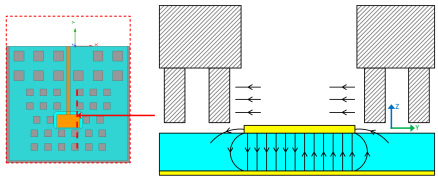

Figure 4: Electric fields inside the cavity and the substrate of vertical transition A.

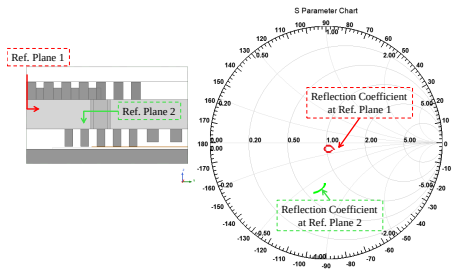

Figure 5: Smith chart of the reflection coefficient from 76 to 81 GHz for transition A.

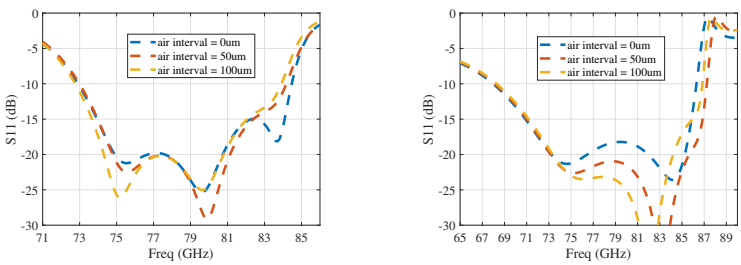

Figure 6: Air interval tolerance checking for transition A (a) and transition B (b).

To gain a better understanding of the impedance matching, the reflection coefficient is monitored at two reference planes as shown in Fig. 5. The normalized impedance of the chart in Fig. 5 is 450 Ohm, as the wave impedance of the ridge line at 78.5 GHz. It has been shown that the ridge probe can realize coupling and impedance matching at the same time. Fig. 6a shows that the simulated reflection coefficient of transition A is better than -15 dB from 74 to 83 GHz regardless of the air interval variation up to 100 μm.

The MMICs will be packaged by pins with different dimensions which are able to block interfering signals and bring favorable space for assembly, as shown in Fig. 2a. Fig. 7a shows the MMIC placed at the bottom layer and wire-bonded to the microstrip lines with transitions to RGW. The first three decoupling capacitors are single layer chip capacitors with values of 56 pF, 100 pF and 100 pF as shown in the figure. There are more decoupling capacitors on the DC board with values of 100 pF, 1 μF and 10 μF to make sure no cross talk on the board at low frequencies. The MMIC is a E-band medium power amplifier with high gain, high linearity, low input and output return loss [34]. The on-wafer measurement shows that the amplifier has small signal gain about 23 dB and reflection coefficient better than -10 dB from 71 to 86 GHz.

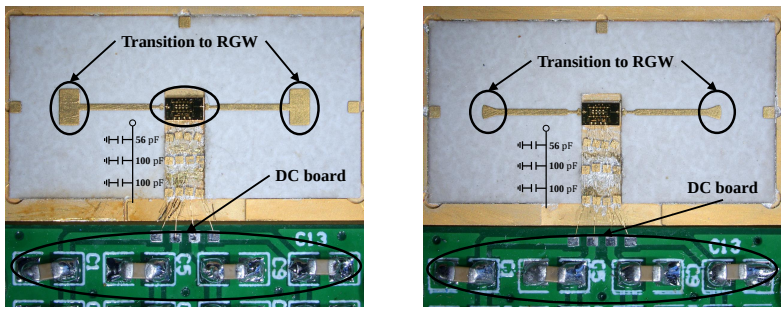

(a) **(b)**

Figure 7: MMIC wire-bonded to microstrip lines in transition A (a) and transition B (b).

2.2 Transition B

In the previous subsection, the vertical transition of microstrip placed at the bottom layer has been introduced. However, due to the patch resonance, transition A is inherently narrow band. In this section, a broadband transition with microstrip line placed at the middle layer but in the opposite side of the ridge line is presented as shown in Fig. 2b.

A radial probe for wider bandwidth has been utilized to couple the EM signal from microstrip line to RGW via a ground slot in the ground plane of the microstrip line and a ridge probe at the top side of the middle layer, as shown in Fig. 8. Utilizing the pins on top of the microstrip line, a back-short cavity has been introduced at the bottom layer as gap waveguide realization of the conventional broadside microstrip probe transition [35]. The dimensions of the microstrip probe, the ground slot and the ridge probe has been carefully optimized for a broadband matching. Likewise, the reflection coefficient of the transition has been monitored at two reference planes to get the insight of the impedance matching, as shown in Fig. 9. The normalization impedance of the chart is also 450 Ohm as the wave impedance of the ridge line at 78.5 GHz. It has been shown that both the bottom microstrip probe and the top ridge probe are wide-band and well-matched.

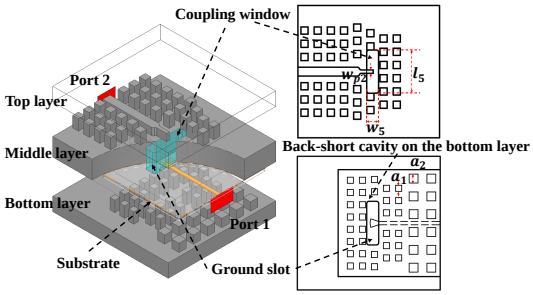

Figure 8: Vertical transition B between packaged microstrip and RGW. ($w_5 = 1.08$ mm, $l_5 = 3.92$ mm,$w_{p2} = 0.3$ mm)

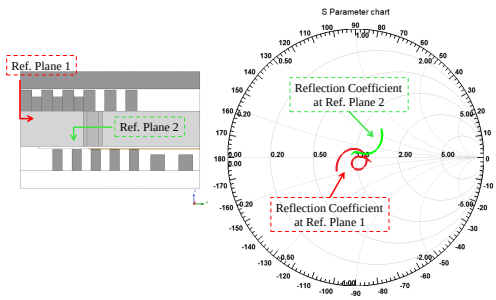

Figure 9: Smith chart of the reflection coefficient from 71 to 86 GHz for transition B.

Fig. 6b shows that the simulated reflection coefficient of transition B is better than -15 dB from 71 to 86 GHz with the air interval variation up to 100 μm. Fig. 7b shows the MMIC placed at the middle layer with transitions to RGW. The MMIC will be packaged by pins with different dimensions as shown in Fig. 2b, in order to prevent unwanted resonant modes.

Compared with the transition A, transition B has advantages of wider bandwidth. However, in system-level design, if the print circuit board (PCB) to be integrated has multi-layer structure, it would be difficult to have a waveguide window underneath the RF layer. This makes the vertical transition A, a transition without the presence of back-short cavity, a better candidate for integration of multi-layer PCB.

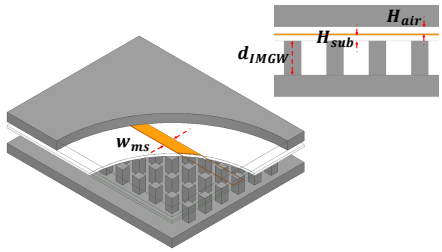

Figure 10: 3D structure of IMGW. ($d_{IMGW} = 0.8$ mm, $H_{sub} = 0.127$ mm, $H_{air} = 0.2$ mm, $w_{ms} = 0.6$ mm)

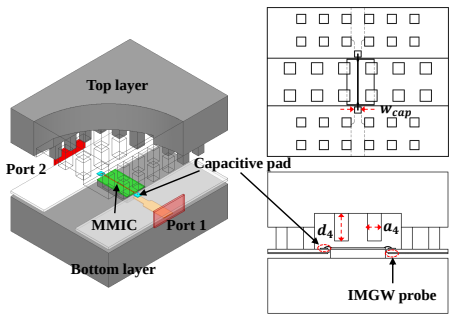

Figure 11: Packaging structure for integration of MMIC with IMGW. ($a_4 = 0.5$ mm, $d_4 = 1$ mm, $w_{cap} = 0.29$ mm)

3 Integration with IMGW

Inverted microstrip gap waveguide, as shown in Fig. 10, has been widely used as transmission line due to its low-loss and compact properties [8], [9], [12]. In spite of the same propagating modes of IMGW line and microstrip line, it is always challenging to realize the integration due to the inverted structure of the IMGW. The substrate of IMGW makes it impossible to achieve direct connection between the lines. In this work, integration of MMICs with IMGW has been realized by wire bonding and capacitive coupling, as shown in Fig. 11. The capacitive pad wire-bonded to the MMIC is working like an extended probe from the chip. This probe and the IMGW probe are facing towards each other, the capacitive coupling is realized inside the substrate, as shown in Fig. 12. The integration is compact and the intermediate transitions are no longer needed. To stop the field from propagating on top of the MMIC, two rows of periodic pins are placed between the input and output section.

To perform measurement, transitions between IMGW and standard WR12 rectangular waveguide have been realized, as shown in Fig. 13. Simulated results of the transition in a

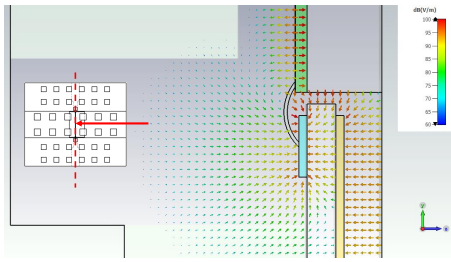

Figure 12: Electric field of capacitive coupling between the wire-bonded pad and the IMGW probe.

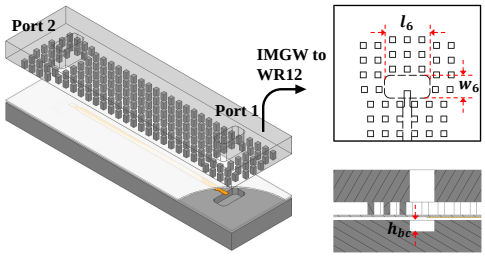

Figure 13: Transitions between IMGW and WR12 in a back-to-back structure. (w_6 = 1.55 mm, l_6 = 3.1 mm, h_{bc} = 0.71 mm)

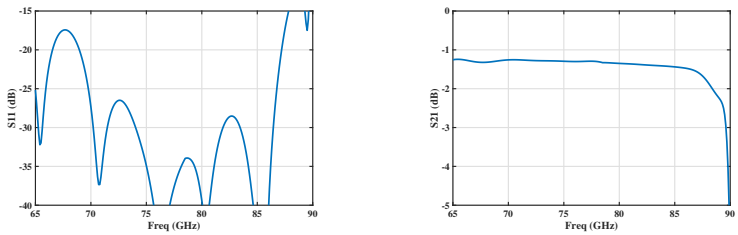

(a) S_{11} **(b)** S_{21}

Figure 14: Simulated results of the transition between IMGW and WR12 in a back-to-back structure.

back-to-back structure are shown in Fig. 14. The insertion loss is less than 1.5 dB including a IMGW line with length of 18.8 mm, and reflection coefficient is better than -25 dB from 71 to 86 GHz.

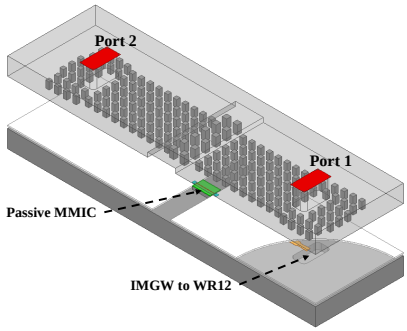

Figure 15: Passive MMIC of 50 Ohm microstrip integrated with IMGW.

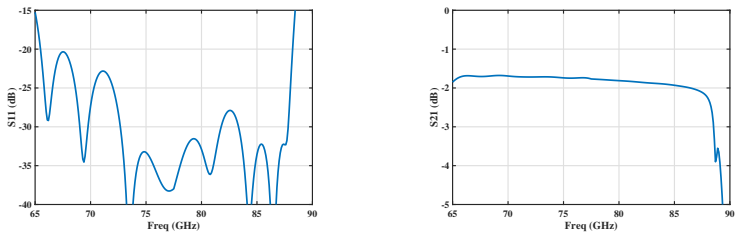

(a) S_{11} **(b)** S_{21}

Figure 16: Simulated results of the passive MMIC integrated with IMGW.

For simulation, a passive MMIC of 50 Ohm microstrip line with 50 μm GaAs substrate has been used here. The integration of the passive MMIC with IMGW is shown in Fig. 15, with transitions to standard WR12 rectangular waveguide at both ends. Good matching performance has been obtained by optimizing the capacitive pad and the IMGW probe. The simulated results in Fig. 16 shows that the reflection coefficient is better than -15 dB and the insertion loss is less than 2 dB from 65 to 88 GHz. Considering the loss of the standard waveguide transitions and IMGW lines with total length of 17.6 mm, the loss attributed to a bond wire in series with a capacitive pad is less than 0.3 dB over the frequency band. However, this is under the assumption that the 50 Ohm MMIC is lossless and the bond wires are perfectly placed. The results have been verified by measurement that will be demonstrated in the next section.

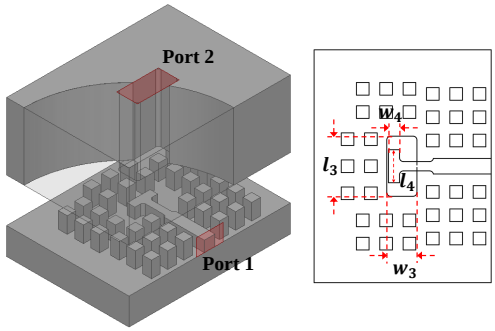

Figure 17: Transition between RGW and WR12 rectangular waveguide. (w_3 = 1.55 mm, l_3 = 3.1 mm, w_4 = 0.57 mm, l_4 = 1.7 mm)

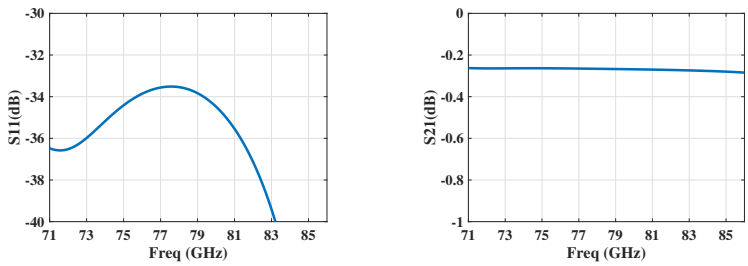

(a) S_{11} **(b)** S_{21}

Figure 18: Simulated results of the transition between WR12 rectangular waveguide and RGW.

4 Measured Results

4.1 Results of the passive back-to-back structures

For the sake of measurement, the transitions between standard WR12 rectangular waveguide and RGW are cascaded at both ends of the back-to-back structures, as shown in Fig. 17. The simulated results of the transition are shown in Fig. 18 while considering the surface roughness of the gold lamination as empirical 0.4 um in Groisse model [36]. The manufactured prototype of transition A implemented in a back-to-back structure are shown in Fig. 19. The prototype is fabricated in brass by 3-axis CNC milling with 0.5 μm gold plating and typical tolerances of $\pm$ 0.1 mm. The smallest distances between the parts of the prototype are larger than 0.5 mm considering the cost of the manufacturing process. The microstrip line used in this design is based on 0.127 mm Rogers 3003 substrate with 1

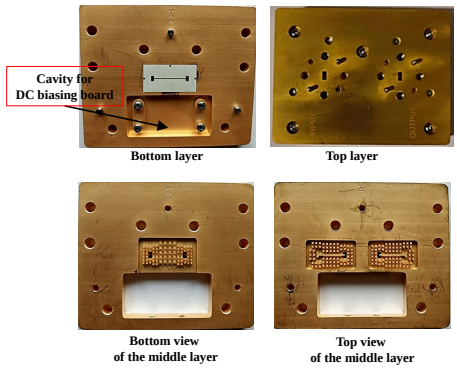

Figure 19: Manufactured prototype of transition A implemented in a back-to-back structure.

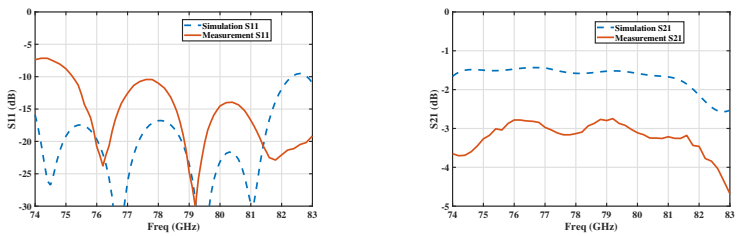

(a) S_{11} **(b)** S_{21}

Figure 20: Simulated and measured results of transition A implemented in a back-to-back structure.

oz copper and length of the line is about 11.2 mm. The substrate offers excellent stability of dielectric constant ($\epsilon_r = 3.00$) over various temperatures and frequencies, thus suitable for applications including automotive radar (77 GHz), advanced driver assistance systems (ADAS). The substrate is sticking to the metal by silver bearing solder paste. The air interval with a nominal value of 50 μm has been created by higher metal walls surrounding the pins, after considering the thickness of the solder paste. The simulated and measured results are shown in Fig. 20. The reflection coefficient is better than -10 dB from 75 to 83 GHz. Considering the microstrip line has about 0.8 dB/cm insertion loss at 79 GHz [37], also, approximately 0.3 dB loss of the standard waveguide transitions at both ends as shown in Fig. 18b, the insertion loss of a single transition A is about 0.65 to 0.85 dB over the frequency band.

The manufactured prototype of transition B implemented in a back-to-back structure are

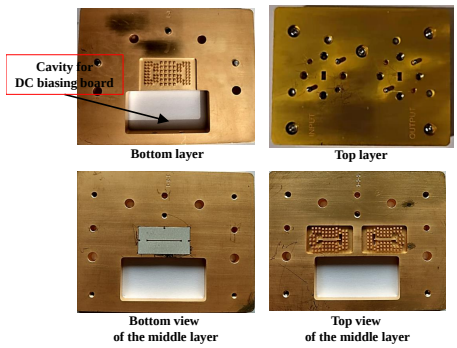

Figure 21: Manufactured prototype of transition B implemented in a back-to-back structure.

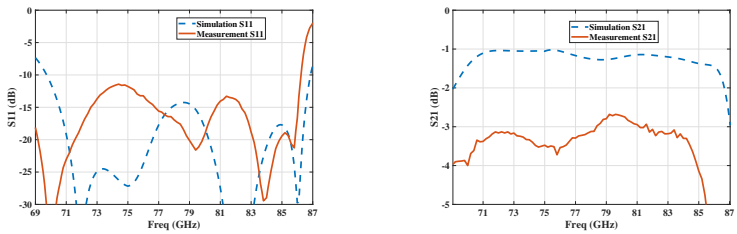

(a) S_{11} **(b)** S_{21}

Figure 22: Simulated and measured results of transition B implemented in a back-to-back structure.

shown in Fig. 21, fabricated in brass by CNC milling with 0.5 μm gold plating as well. The substrate is 0.127 mm Rogers 3003 and the length of line is about 10.6 mm. To prevent the solder paste from flowing into the coupling window, the distribution of the paste has been done carefully and checked under the microscope. The simulated and measured results are shown in Fig. 22. The reflection coefficient is better than -10 dB from 69 to 86 GHz. Considering the microstrip line has about 0.85 dB insertion loss [37] and about 0.3 dB loss for each standard waveguide transition, the insertion loss of a single transition B is approximately 0.65 to 1 dB over the frequency band.

Compared with similar transitions between microstrips and waveguides including RW, GGW and RGW presented in the literature, the proposed transitions have good performance in terms of bandwidth and insertion loss, as shown in Table 1. For the vertical transitions to RW, electrical contact is required between the substrate and the metal piece of waveguide [1], [4]. However, this is eliminated for gap waveguide based transitions as shown in the previous

Table 1: Comparison Between Different Transitions from Microstrips to Waveguides

Ref	[1]	[4]	[13]	[24]	A	B
Freq. (GHz)	54-65	75-87	69-87	54-71	75-83	69-86
10 dB B.W.%	16.6	15	23	27.2	10.1	21.9
I.L. (dB)	1	0.6 -1	0.31	0.38	0.65 -0.85	0.65 -1
Sub.	Rogers 4003	Rogers 3003	LCP	Alumina	Rogers 3003	Rogers 3003
Conf.	vertical	vertical	inline	inline	vertical	vertical
WG	RW	RW	GGW	GGW	RGW	RGW

section, also in [28]–[30]. Moreover, vertical transitions are more applicable compared with inline transitions considering the advanced features of compactness and flexibility.

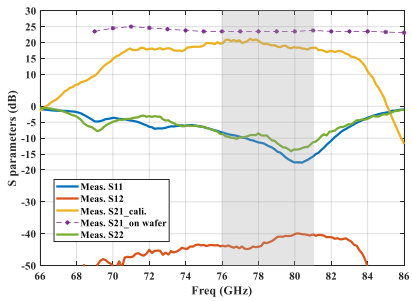

Figure 23: Measured results of the MMIC integrated with RGW using transition A (gray area is the operating frequency band).

4.2 Results of MMICs integrated with gap waveguides

MMIC integrated with RGW using transition A

Fig. 23 shows the measured results of the MMIC integrated with RGW line using transition A. From 76 GHz to 81 GHz, the integrated MMIC has small signal gain larger than 18 dB while the losses of the standard waveguide transitions at both ends and extra microstrip line of 8.9 mm have been calibrated out. The reflection coefficient is better than -9 dB within the same frequency band. Considering the loss of the bond wires and the transitions, the results show good agreement with the on-wafer measurement as shown in Fig. 23. Thanks to

the gap waveguide packaging structure, no unwanted parallel plate modes or cavity modes are induced within the frequency band.

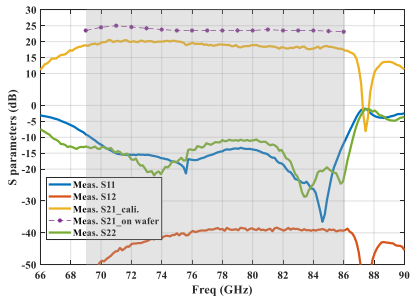

Figure 24: Measured results of the MMIC integrated with RGW using transition B (gray area is the operating frequency band).

MMIC integrated with RGW using transition B

Fig. 24 shows the measured results of the MMIC integrated with RGW line using transition B. From 69 to 86 GHz, the integrated MMIC has small signal gain larger than 18 dB while the losses of the standard waveguide transitions at both ends and extra microstrip line of 9 mm have been calibrated out. The reflection coefficient is better than -10 dB within the same frequency band. The measured results show good agreement with the on-wafer measurement considering the loss of bond wires and transitions.

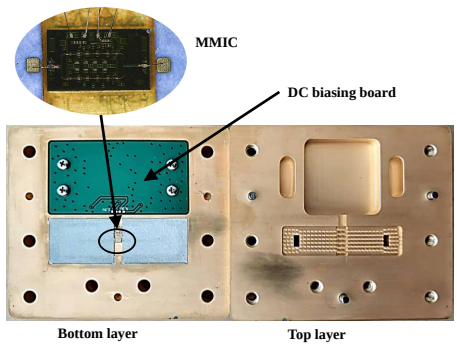

Figure 25: Manufactured prototype of the MMIC integrated with IMGW line.

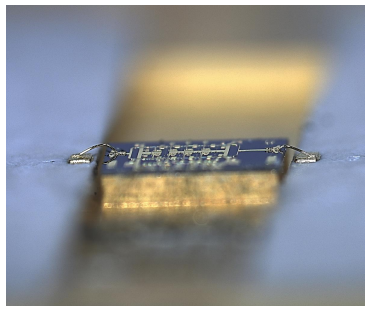

Figure 26: Side view of the MMIC integrated with IMGW line.

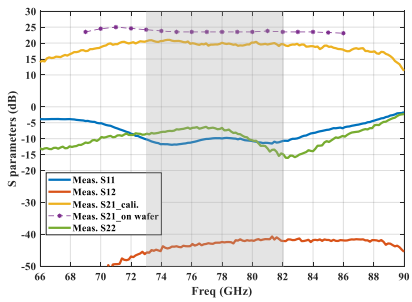

Figure 27: Measured results of the MMIC integrated with IMGW (gray area is the operating frequency band).

MMIC integrated with IMGW

The same amplifier has been used to realize the integration with IMGW line, as shown in Fig. 25. By using the bond wires and capacitive pads, the integration is compact. However, the substrate of the pad is suspended over the air, it causes difficulties for the wire bonding because of the weak support. In addition, the IMGW lines tend to have flatness problem as a result of the thin substrate, as shown in Fig. 26. The right side, which is the output of the MMIC, is clearly not even with the left side. The measured results of the MMIC integrated with IMGW line are shown in Fig. 27. The amplifier has reflection coefficient better than -10 dB and small signal gain larger than 19.5 dB from 73 to 82 GHz while the losses of standard waveguide transitions at both ends and extra IMGW line of 17.6 mm have been calibrated out. Likewise, no resonance has been induced within the frequency band, thanks to the gap waveguide packaging structure.

Unfortunately, the large signal measurements are not attainable because of the limited conditions of the lab. The small signal measurement results have shown that the reverse isolation of all three packaged amplifiers are larger than 35 dB as a result of the gap

waveguide packaging structures on top of the circuits that are able to prevent unwanted feedback between the output and input. The result can be considered as an indication that the chip will most likely not oscillate under large signal scenario.

The deviation between the gain of the amplifier integrated with gap waveguide and the on-wafer amplifier is about 5 dB maximum. The extra loss of the integrated amplifier is attributed to two main factors. One of the factor is the bond wire losses at this frequency which is found to be about 2-3 dB for two bond wire sections at the input and the output of the circuits as demonstrated in [38], [39]. The other factor is the losses of the transitions at both sides which account for about 1.5 dB for transition A, 1.7 dB for transition B as demonstrated in the passive back-to-back measurements, and 0.6 dB for the capacitive pads of IMGW packaging as verified by the simulation. However, all these factors could be eliminated or greatly reduced if the MMIC's input/output GSG (Ground-Signal-Ground) pads would be replaced with an integrated transition section already in the MMIC as demonstrated in paper [40]. For instance, the integration with IMGW could be implemented on wafer scale by using defected ground metallization. The vertical transitions with RGW probably would consume more chip space, therefore demand compromise and trade-off between the performance and cost. These are of course not possible at the moment with the off-the-shelf commercial MMICs and falls within the scope of new MMIC design and foundry tape-out which will be presented in future publications. At this point, we have demonstrated the potential of the proposed transitions which are suitable for gap waveguide integrations.

5 Conclusion

Two vertical transitions for integration of MMICs with RGW and one novel packaging structure for integration of MMICs with IMGW have been presented in this paper. The first vertical transition utilizes rectangular microstrip patch to couple the signal to the RGW. Measured results of the transition in a back-to-back structure show that the reflection coefficient is better than -10 dB from 75 to 83 GHz and the insertion loss for a single transition over the frequency band is 0.65 to 0.85 dB. The second vertical transition utilizes a radial probe with a ground slot of the microstrip. Measured results of the second transition in a back-to-back structure show that the reflection coefficient is better than -10 dB from 69 to 86 GHz and the insertion loss for a single transition is 0.65 to 1 dB over the frequency band. Commercial MMIC amplifiers have been integrated with the RGW using the two vertical transitions. The measured results of the integrated MMICs show good performance in terms of small signal gain and bandwidth. The integration of MMIC with IMGW has been realized by utilizing the bond wires and capacitive pads. The measured results show that the amplifier integrated with IMGW has reflection coefficient better than -10 dB and small signal gain larger than 19.5 dB from 73 to 82 GHz. The proposed techniques are reasonably wide-band, compact and suitable for multi-layer gap waveguide applications.

Acknowledgments

The authors would like to thank Olof Eriksson and Konstantinos Konstantinidis from Veoneer Sweden, Robert Moestam and Bo Wendemo from CEVT for their support and discussion during this project. Special thanks to Yan Yu from MC2, Chalmers, for her help with measurements and Hanna Karlsson from Gapwaves AB for her kind support and sharing her previous work with us. This work is supported by Swedish Strategic Vehicle Research and Innovation FFI grant 2018-02707.

References

[1] A. Artemenko, A. Maltsev, R. Maslennikov, A. Sevastyanov, and V. Ssorin, "Design of wideband waveguide to microstrip transition for 60 GHz frequency band," in *2011 41st European Microwave Conference*, 2011, pp. 838–841.

[2] Z. Tong and A. Stelzer, "A vertical transition between rectangular waveguide and coupled microstrip lines," *IEEE Microwave and Wireless Components Letters*, vol. 22, no. 5, pp. 251–253, 2012.

[3] E. S. Li, G.-X. Tong, and D. C. Niu, "Full W-band waveguide-to-microstrip transition with new E-plane probe," *IEEE Microwave and Wireless Components Letters*, vol. 23, no. 1, pp. 4–6, 2013.

[4] E. Topak, J. Hasch, and T. Zwick, "Compact topside millimeter-wave waveguide-to-microstrip transitions," *IEEE Microwave and Wireless Components Letters*, vol. 23, no. 12, pp. 641–643, 2013.

[5] A. U. Zaman, M. Alexanderson, T. Vukusic, and P.-S. Kildal, "Gap waveguide PMC packaging for improved isolation of circuit components in high-frequency microwave modules," *IEEE Transactions on Components, Packaging and Manufacturing Technology*, vol. 4, no. 1, pp. 16–25, 2014.

[6] A. Vosoogh, A. Haddadi, A. U. Zaman, J. Yang, H. Zirath, and A. A. Kishk, "W -band low-profile monopulse slot array antenna based on gap waveguide corporate-feed network," *IEEE Transactions on Antennas and Propagation*, vol. 66, no. 12, pp. 6997–7009, 2018.

[7] J. Liu, A. Vosoogh, A. U. Zaman, and J. Yang, "A slot array antenna with single-layered corporate-feed based on ridge gap waveguide in the 60 GHz band," *IEEE Transactions on Antennas and Propagation*, vol. 67, no. 3, pp. 1650–1658, 2019.

[8] M. Sharifi Sorkherizi, A. Dadgarpour, and A. A. Kishk, "Planar high-efficiency antenna array using new printed ridge gap waveguide technology," *IEEE Transactions on Antennas and Propagation*, vol. 65, no. 7, pp. 3772–3776, 2017.

[9] A. Dadgarpour, N. Bayat-Makou, M. A. Antoniades, A. A. Kishk, and A. Sebak, "A dual-polarized magnetoelectric dipole array based on printed ridge gap waveguide with dual-polarized split-ring resonator lens," *IEEE Transactions on Antennas and Propagation*, vol. 68, no. 5, pp. 3578–3585, 2020.

[10] A. K. Horestani and M. Shahabadi, "Balanced filter with wideband common-mode suppression in groove gap waveguide technology," *IEEE Microwave and Wireless Components Letters*, vol. 28, no. 2, pp. 132–134, 2018.

[11] A. Vosoogh, M. S. Sorkherizi, A. U. Zaman, J. Yang, and A. A. Kishk, "An integrated Ka-band diplexer-antenna array module based on gap waveguide technology with simple mechanical assembly and no electrical contact requirements," *IEEE Transactions on Microwave Theory and Techniques*, vol. 66, no. 2, pp. 962–972, 2018.

[12] J. Liu, A. Vosoogh, A. U. Zaman, and J. Yang, "Design and fabrication of a high-gain 60-GHz cavity-backed slot antenna array fed by inverted microstrip gap waveguide," *IEEE Transactions on Antennas and Propagation*, vol. 65, no. 4, pp. 2117–2122, 2017.

[13] A. Vosoogh, M. Sharifi Sorkherizi, V. Vassilev, *et al.*, "Compact integrated full-duplex gap waveguide-based radio front end for Multi-Gbit/s point-to-point backhaul links at E-band," *IEEE Transactions on Microwave Theory and Techniques*, vol. 67, no. 9, pp. 3783–3797, 2019.

[14] E. Rajo-Iglesias, M. Ferrando-Rocher, and A. U. Zaman, "Gap waveguide technology for millimeter-wave antenna systems," *IEEE Communications Magazine*, vol. 56, no. 7, pp. 14–20, 2018.

[15] J. Steinbaeck, C. Steger, G. Holweg, and N. Druml, "Next generation radar sensors in automotive sensor fusion systems," in *2017 Sensor Data Fusion: Trends, Solutions, Applications (SDF)*, 2017, pp. 1–6.

[16] W. Menzel and A. Moebius, "Antenna concepts for millimeter-wave automotive radar sensors," *Proceedings of the IEEE*, vol. 100, no. 7, pp. 2372–2379, 2012.

[17] G. F. Hamberger, S. Späth, U. Siart, and T. F. Eibert, "A mixed circular/linear dual-polarized phased array concept for automotive radar-planar antenna designs and system evaluation at 78 GHz," *IEEE Transactions on Antennas and Propagation*, vol. 67, no. 3, pp. 1562–1572, 2019.

[18] O. Khan, J. Meyer, K. Baur, and C. Waldschmidt, "Hybrid thin film antenna for automotive radar at 79 GHz," *IEEE Transactions on Antennas and Propagation*, vol. 65, no. 10, pp. 5076–5085, 2017.

[19] J. Mayer, M. Martina, T. Gottwald, and T. Zwick, "PCB laminates for automotive radar antenna modules under different environmental conditions," *IEEE Transactions on Antennas and Propagation*, vol. 67, no. 9, pp. 6051–6058, 2019.

[20] A. Haddadi, C. Bencivenni, and T. Emanuelsson, "Gap waveguide slot array antenna for automotive applications at E-band," in *2019 13th European Conference on Antennas and Propagation (EuCAP)*, 2019, pp. 1–4.

[21] A. Vosoogh, P.-S. Kildal, and V. Vassilev, "A multi-layer gap waveguide array antenna suitable for manufactured by die-sink EDM," in *2016 10th European Conference on Antennas and Propagation (EuCAP)*, 2016, pp. 1–4.

[22] S. Farjana, M. Ghaderi, A. U. Zaman, *et al.*, "Realizing a 140 GHz gap waveguide–based array antenna by low-cost injection molding and micromachining," *Journal of Infrared, Millimeter, and Terahertz Waves*, vol. 42, no. 8, pp. 893–914, 2021, ISSN: 1866-6906.

[23] S. Farjana, M. Ghaderi, A. U. Zaman, S. Rahiminejad, P. Lundgren, and P. Enoksson, "Low-loss gap waveguide transmission line and transitions at 220–320 GHz using dry film micromachining," *IEEE Transactions on Components, Packaging and Manufacturing Technology*, vol. 11, no. 11, pp. 2012–2021, 2021.

[24] U. Nandi, A. U. Zaman, A. Vosoogh, and J. Yang, "Novel millimeter wave transition from microstrip line to groove gap waveguide for MMIC packaging and antenna integration," *IEEE Microwave and Wireless Components Letters*, vol. 27, no. 8, pp. 691–693, 2017.

[25] Y. Shi, J. Zhang, S. Zeng, and M. Zhou, "Novel W -Band millimeter-wave transition from microstrip line to groove gap waveguide for MMIC integration and antenna application," *IEEE Transactions on Antennas and Propagation*, vol. 66, no. 6, pp. 3172–3176, 2018.

[26] J. M. Pérez-Escudero, A. E. Torres-García, R. Gonzalo, and I. Ederra, "A Chebyshev transformer-based microstri-to-groove-gap-waveguide inline transition for MMIC packaging," *IEEE Transactions on Components, Packaging and Manufacturing Technology*, vol. 9, no. 8, pp. 1595–1602, 2019.

[27] Y. Shi, W. Feng, H. Wang, *et al.*, "Novel W -Band LTCC transition from microstrip line to ridge gap waveguide and its application in 77/79 GHz antenna array," *IEEE Transactions on Antennas and Propagation*, vol. 67, no. 2, pp. 915–924, 2019.

[28] C. Bencivenni, A. U. Zaman, A. Haddadi, and T. Emanuelsson, "Towards integrated active antennas for 5G mm-wave applications at Gapwaves," in *2018 IEEE International Symposium on Antennas and Propagation USNC/URSI National Radio Science Meeting*, 2018, pp. 415–416.

[29] A. Bagheri, H. Karlsson, C. Bencivenni, A. Haddadi, T. Emanuelsson, and A. A. Glazunov, "Microstrip to ridge gap waveguide transition for 28 GHz steerable slot array antennas," in *2020 14th European Conference on Antennas and Propagation (EuCAP)*, 2020, pp. 1–4.

[30] B. Molaei and A. Khaleghi, "A novel wideband microstrip line to ridge gap waveguide transition using defected ground slot," *IEEE Microwave and Wireless Components Letters*, vol. 25, no. 2, pp. 91–93, 2015.

[31] Q. Ren, A. U. Zaman, J. Yang, V. Vassilev, and C. Bencivenni, "Millimeter-wave vertical transitions between ridge gap waveguides and microstrip lines for integration of MMIC with slot array," in *2021 15th European Conference on Antennas and Propagation (EuCAP)*, 2021, pp. 1–4.

[32] C. Bencivenni, M. Gustafsson, A. Haddadi, A. U. Zaman, and T. Emanuelsson, "5G mmwave beam steering antenna development and testing," in *2019 13th European Conference on Antennas and Propagation (EuCAP)*, 2019, pp. 1–4.

[33] Y. S. H. Khraisat and M. M. Olaimat, "Comparison between rectangular and triangular patch antennas array," in *2012 19th International Conference on Telecommunications (ICT)*, 2012, pp. 1–5.

[34] Gotmic AB, *E-band MPA MMIC 71-86 (68-89) GHz*, Accessed Jan. 18, 2022.

[35] Y.-C. Leong and S. Weinreb, "Full band waveguide-to-microstrip probe transitions," in *1999 IEEE MTT-S International Microwave Symposium Digest (Cat. No.99CH36282)*, vol. 4, 1999, 1435–1438 vol.4.

[36] S. Groiss, I. Bardi, O. Biro, K. Preis, and K. Richter, "Parameters of lossy cavity resonators calculated by the finite element method," *IEEE Transactions on Magnetics*, vol. 32, no. 3, pp. 894–897, 1996.

[37] R. Corp., *New laminates enable 79 GHz technology advancements*, Apr. 2018.

[38] S. Jameson and E. Socher, "A wide-band CMOS to waveguide transition at mm-wave frequencies with wire-bonds," *IEEE Transactions on Microwave Theory and Techniques*, vol. 63, no. 9, pp. 2741–2750, 2015.

[39] Y. Dong, T. K. Johansen, V. Zhurbenko, and P. J. Hanberg, "Rectangular waveguide-to-coplanar waveguide transitions at U-band using E-plane probe and wire bonding," in *2016 46th European Microwave Conference (EuMC)*, 2016, pp. 5–8.

[40] A. Hassona, V. Vassilev, A. U. Zaman, *et al.*, "Nongalvanic generic packaging solution demonstrated in a fully integrated *D*-band receiver," *IEEE Transactions on Terahertz Science and Technology*, vol. 10, no. 3, pp. 321–330, 2020.

PAPER C

A Dual Circularly Polarized Array Antenna for Ka-Band Satellite Communications

Qiannan Ren, Ashraf Uz Zaman, Jian Yang

2021 International Symposium on Antennas and Propagation (ISAP), 2021, pp. 1-2.
 DOI: 10.23919/ISAP47258.2021.9614491

The layout has been revised.

Abstract

This work presents a dual circularly polarized 8-by-8 array antenna using inbuilt polarizers for satellite communications. The design consists of five metal layers, including two feeding layers for the dual circular polarizations and a polarizer layer that utilizes a pair of sector cavities as phase delay elements for each sub-array. Two corporate feeding networks using folded E-plane and H-plane T-junctions are proposed to excite the radiating elements. Simulated results of the array antenna have shown that the axial ratios are less than 1 dB from 29 to 31 GHz for both polarizations. The realized gains for both polarizations are larger than 25 dBi at center frequency.

Index Terms: Dual circular polarization, Polarizer, Antenna array, Ka-band.

1 Introduction

With the advent of next generation high throughput satellite communication systems, dual circularly polarized antenna systems operating at Ka band have been widely investigated in recent years [1]-[2]. On the one hand, Ka band features higher throughput comparing with lower frequency bands, such as C band and Ku band. On the other hand, dual circular polarization will provide enhanced isolation between the transmitting and receiving channels. Moreover, circular polarization is more favorable than linear polarization considering the suppression of multi-path interference of satellite communication.

Normally, circularly polarized waves are realized by combining two orthogonal linearly-polarized waves with 90° phase difference. In [3], a dual-circularly polarized horn antenna operating at V-band has been proposed based on an inbuilt mono-groove polarizer. A left-hand circularly polarized horn antenna featuring internal polarizer that consists of nine pairs of circular cavities, has been designed in [4]. It has been shown that circular waveguide based polarizers have advantages of better radiation performance comparing with conventional septum polarizer [5]-[6].

The antenna proposed in this work utilizes a pair of sector cavities as phase delay elements. The simulated results show good performance regarding axial ratios over the frequency band of interest.

2 Dual-circularly Polarized Sub-array

Fig.1 shows the geometry of the dual-circularly polarized sub-array. The design consists of two feeding layers with respect to two orthogonal polarizations. The polarizer has been realized by two sector cavities that are placed 45° and 135° offset from both feeding ports respectively. The operating principle can be demonstrated using Fig.2. When port 1 is excited, the TE_{11} wave inside the circular waveguide $\vec{E_1}$ can be decomposed into two components: $\vec{E_{1x}}$ and $\vec{E_{1y}}$. $\vec{E_{1y}}$ will experience a larger propagating radius than $\vec{E_{1x}}$. When the waves go through the polarizer with specific length, $\vec{E_{1x}}$ will be 90° phase ahead

of $\vec{E_{1y}}$, thus generate RHCP waves. Similarly, when port 2 is excited, it will generate LHCP waves.

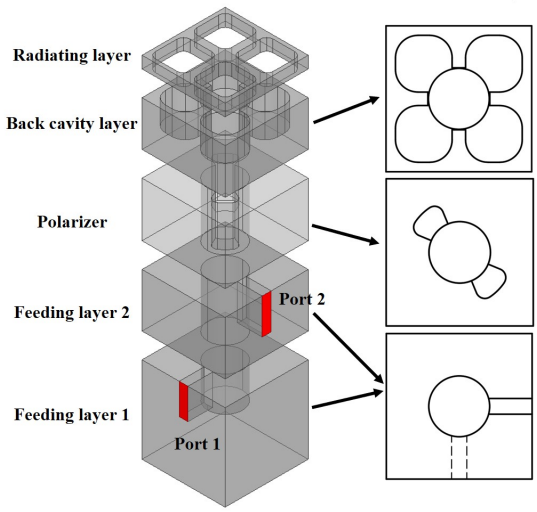

Figure 1: Overview of the sub-array consisting of 5 layers.

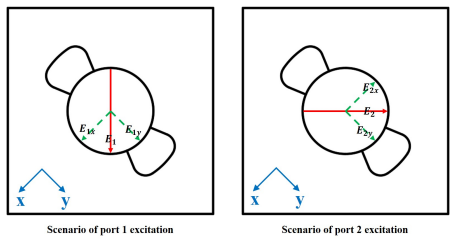

Figure 2: polarizer using a pair of circular cavities.

3 Simulation Results of the Array Antenna

A 8-by-8 antenna array has been proposed in this work utilizing the sub-array discussed in the previous section, as shown in Fig.3. Compact feeding networks have been realized by combination of folded E-plane and H-plane T-junctions. The reflection coefficient of the inputs, as well as the isolation between the two input ports are shown in Fig.4. The

radiation patterns of the array at the center frequency for both polarization are shown in Fig.5. Fig.6 shows the simulated axial ratio of both configurations. Thanks to the circular waveguide based polarizer, the array antenna shows good radiation performance.

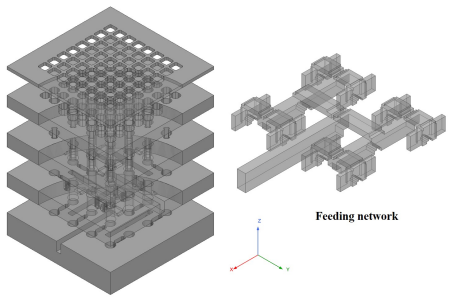

Figure 3: Overview of the 8-by-8 antenna array.

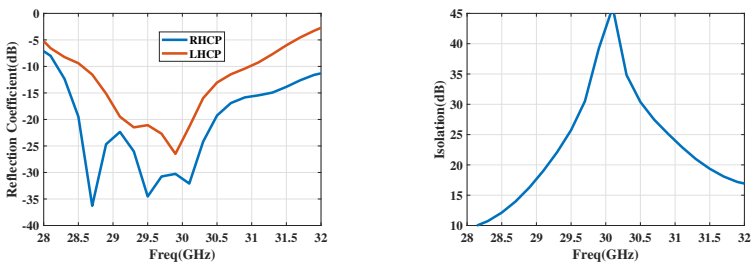

Figure 4: Reflection coefficient and isolation of the inputs.

4 Conclusion

A dual circularly polarized 8-by-8 array antenna for satellite communications has been proposed in this work. The design consists of five metal layers, including two feeding layers and a polarizer layer that utilize two sector cavities as phase delay elements for each sub-array. Simulated results of the array antenna have shown that the axial ratios are less than 1 dB from 29 to 31 GHz for both polarizations. It also shows good performance in terms reflection coefficients and isolation.

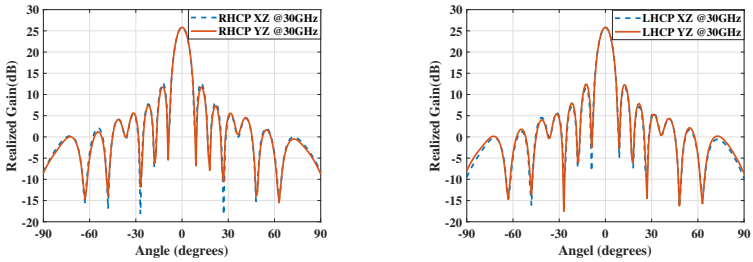

Figure 5: Simulated XZ and YZ pattern.

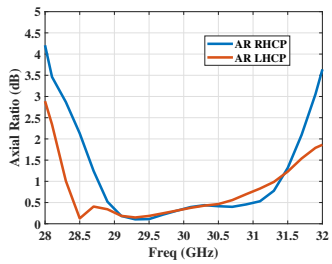

Figure 6: Simulated axial ratio of both configurations.

Acknowledgment

This work is supported by Swedish Strategic Vehicle Research and Innovation FFI grant 2018-02707.

References

[1] S. Mener, R. Gillard, and L. Roy, "A dual-band dual-circular-polarization antenna for Ka-band satellite communications," *IEEE Antennas and Wireless Propagation Letters*, vol. 16, pp. 274–277, 2017.

[2] P. Naseri, S. A. Matos, J. R. Costa, C. A. Fernandes, and N. J. G. Fonseca, "Dual-band dual-linear-to-circular polarization converter in transmission mode application to K/Ka -band satellite communications," *IEEE Transactions on Antennas and Propagation*, vol. 66, no. 12, pp. 7128–7137, 2018.

[3] N. Luo, X. Yu, G. Mishra, and S. K. Sharma, "A millimeter-wave (V-band) dual-circular-polarized horn antenna based on an inbuilt monogroove polarizer," *IEEE Antennas and Wireless Propagation Letters*, vol. 19, no. 11, pp. 1933–1937, 2020.

[4] G. Mishra, S. K. Sharma, and J.-C. S. Chieh, "A circular polarized feed horn with inbuilt polarizer for offset reflector antenna for W -band cubesat applications," *IEEE Transactions on Antennas and Propagation*, vol. 67, no. 3, pp. 1904–1909, 2019.

[5] C. Shu, J. Wang, S. Hu, *et al.*, "A wideband dual-circular-polarization horn antenna for mmWave wireless communications," *IEEE Antennas and Wireless Propagation Letters*, vol. 18, no. 9, pp. 1726–1730, 2019.

[6] C. Kumar, V. V. Srinivasan, V. K. Lakshmeesha, and S. Pal, "Novel dual circularly polarized radiating element for spherical phased-array application," *IEEE Antennas and Wireless Propagation Letters*, vol. 8, pp. 826–829, 2009.

PAPER D

Dual-Circularly Polarized Array Antenna Based on Gap Waveguide Utilizing Double-grooved Circular Waveguide Polarizer

Qiannan Ren, Ashraf Uz Zaman, Jian Yang

Accepted by IEEE Transactions on Antennas and Propagation

The layout has been revised.

Abstract

This paper presents a dual-circularly polarized array antenna based on gap waveguide technology operating at E band. Double-grooved circular waveguide polarizers that utilize two annulus grooves placed at 45° and 135° offset from both excitation ports are used in this work. The operating principles of the polarizer are analyzed. Multi-layer design using gap waveguide is implemented on the basis of the polarizer. The antenna consists of six layers, including three layers for the feeding networks, one layer for the polarizer, one layer of back cavity and another layer of radiating grid. A 2×2 unit cell is proposed firstly and employed to realize a 8×8 planar array. Corporate feeding networks that use compact E-plane T-junctions and H-plane T-junctions are proposed. The antenna has been fabricated and verified by measurements. The measured results of S-parameters agree well with the simulation and show that reflection coefficients are better than -10 dB for both circular polarizations from 76 to 81 GHz. The measured isolation between the input ports is larger than 25 dB in the operating band. The far-field measurements show that the antenna has realized gain larger than 24 dBi and axial ratios less than 1.5 dB from 76 to 81 GHz at boresight direction.

Index Terms: gap waveguide, millimeter wave, dual circular polarization, antenna array, polarizer.

1 Introduction

Millimeter wave radar sensors have advantages over other environmental perception sensors for driving assistance applications. Radar sensors are able to work in foggy, dusty, snowy and badly lighted environments [1]. And it demands more sophisticated antenna systems for better detectability [2], [3]. Current systems utilizing single linear polarization (LP) that lack polarimetric capabilities are not capable of measuring the full scattering matrix, thus losing information about the scenery [4]. In this respect, the radar front end needs antennas with orthogonal polarizations in both transmitting (Tx) and receiving (Rx) paths. The polarizations could be dual LP or dual circular polarization (CP). However, signals having LP are more susceptible to multi-path fading and polarization rotation compared with CP. In this regard, dual circularly polarized antenna systems operating at millimeter wave frequency have been widely investigated for automotive radars applications recently [5].

Generally, circularly polarized waves can be realized by combining two orthogonal linearly-polarized waves with 90° phase difference, like when using the waveguide iris polarizer [6], [7]. Recently, grooved circular waveguide polarizer has been widely investigated. In [8], a polarizer with four single-grooved circular waveguides and a polarizer with four double-grooved circular waveguides are designed in 20-GHz band with the aid of the presented design and analysis techniques. In [9], a dual circularly polarized horn antenna operating at V-band has been proposed based on an inbuilt mono-groove polarizer. In [10], a double grooved

circular waveguide polarizer with coaxial probe excitation is proposed. In [11], another dual circularly polarized horn antenna has been presented using double grooved circular waveguide polarizer. The excitations are implemented by an orthogonal mode transducer (OMT). Rigorous solutions of the fields inside the grooved circular waveguide have been investigated in [12], [13]. It has been shown that circular waveguide based polarizers have competitive polarization performance compared with conventional septum polarizer [14], [15]. However, such polarizers have never been utilized in an array configuration due to complexity of the fabrication and size constraints. In this work, we overcome the above mentioned challenges and for the first time use such polarizer in a high gain array configuration.

Gap waveguide technology has been widely used for multi-layer antenna designs [16]–[18]. It features non-galvanic contact between the layers, thereby ensure higher reliability of assembly and robustness of the design [19], [20]. As a result, gap waveguide components can be fabricated at mmWave and sub-mmWave frequency range with low cost techniques such as EDM, 3D printing and polymer micro-machining [21]–[24]. Dual circularly polarized gap waveguide antennas have been investigated by several studies. In [25], a fully-metallic dual-circularly polarized array antenna has been presented by integration of a hybrid coupler and a dual LP antenna [26]. But the antenna operates at Ka band and has 5% relative bandwidth. In [27], a E-band single-layer dual-circularly polarized antenna array that consists of eight U-shaped slots is proposed based on ridge gap waveguides (RGW). But the antenna is a linear array and demands complex feeding networks.

In this paper, a 8×8 dual-circularly polarized array antenna based on gap waveguide technology is presented, for the very first time, utilizing double-grooved circular waveguide polarizer. The polarizers implemented by gap waveguide feature high robustness in mechanical assembly and better electrical performance in terms of antenna efficiency and polarization purity. Compact E-plane and H-plane T-junctions based on horizontally polarized groove gap waveguide (GGW) and RGW are proposed to realize the feeding networks of the two orthogonal polarizations. The antenna is fabricated and verified by measurements which show good agreement with the simulation.

The paper is organized as follows. The operating principles of the double-grooved circular waveguide polarizer are introduced in Section II. The unit cell design based on gap waveguide technology is described in Section III. The array design and measurements are given in Section IV and Section V, respectively. Finally, conclusions are given in Section VI.

2 Double-grooved Circular Waveguide Polarizer

The proposed double-grooved circular waveguide polarizer with two orthogonal excitation ports is shown in Fig. 1. A circular waveguide is used as the transmission line to connect the polarizer and two feeding rectangular waveguides. Moreover, the radius of the circular waveguide transmission line is kept the same for different sections to simplify the design. Two sector grooves are placed 45° and 135° offset from port RHCP and port LHCP respectively. Compared with single-grooved circular waveguide polarizers as demonstrated in [9], using a pair of sector grooves can reduce the size of the polarizer and realize better amplitude and phase balance over the frequency range [10]. The distance between the center of the ports and the back-short plane of the circular waveguide should be $(\frac{\lambda}{4}+\frac{\lambda}{2}*\mathbb{N}, \mathbb{N}=0,1,2,\ldots)$. This is to make sure that the excitation ports are located at voltage maximum for better

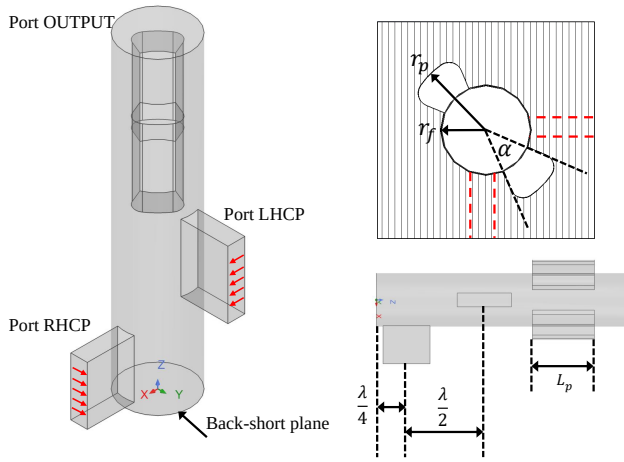

Figure 1: Double-grooved circular waveguide polarizer with two orthogonal excitation ports.

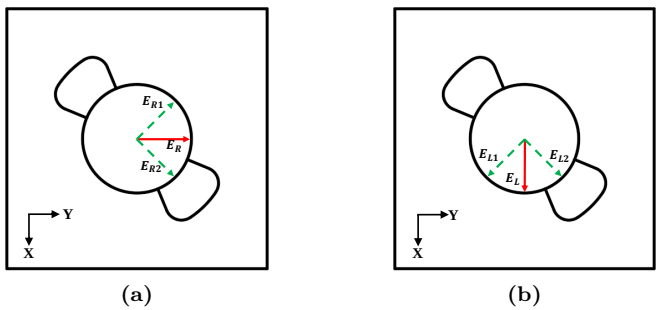

(a) **(b)**

Figure 2: Electric fields of TE_{11} wave and decomposed components inside the polarizer when (a) port RHCP and (b) port LHCP are excited.

coupling. The excitation ports are able to generate TE_{11} waves with orthogonal linear polarizations inside the circular waveguide. Therefore, it will assure good isolation between the rectangular feeding waveguides.

The operating principle of the polarizer is depicted in Fig.2. When port RHCP is excited, the dominant mode TE_{11} inside the circular waveguide $\mathbf{E_R}$ can be decomposed into two orthogonal components with the same amplitude: $\mathbf{E_{R1}}$ and $\mathbf{E_{R2}}$. $\mathbf{E_{R2}}$ will experience a larger propagation radius than $\mathbf{E_{R1}}$. When the waves propagate through the polarizer with

length of L_p, the phase difference between the two components can be written as:

$$\Delta\phi = \phi_1 - \phi_2 = (\beta_1 - \beta_2)L_p \tag{D.1}$$

where

$$\beta_1 = \sqrt{k^2 - (\frac{p'_{11}}{r_f})^2} \tag{D.2}$$

$$\beta_2 = \sqrt{k^2 - (\frac{p'_{11}}{r_p})^2} \tag{D.3}$$

β_1 and β_2 are the wave numbers of $\mathbf{E_{R1}}$ and $\mathbf{E_{R2}}$, respectively. p'_{mn} is the first root of the derivative of first order Bessel function. Because r_p is larger than r_f, β_2 is larger than β_1. With a specific length of L_p, $\Delta\phi = -90°$, which means $\mathbf{E_{R1}}$ is delayed by 90° compared to $\mathbf{E_{R2}}$, the polarizer will generate RHCP waves propagating at $+z$ direction. Similarly, when port LHCP is excited, $\mathbf{E_{L2}}$ will be 90° phase ahead of $\mathbf{E_{L1}}$, thus the polarizer will generate LHCP waves with $+z$ as the direction of propagation. r_p and r_f are chosen so that only dominant TE_{11} modes exist. α is chosen after considering the manufacturing challenges. L_p is chosen by equation D.1 after r_p and r_f. Finally, thorough optimization has been conducted.

To gain a better understanding of the polarizer, the magnitude and phase difference of two orthogonal components at port OUTPUT are shown in Fig. 3. The maximum magnitude differences are less than 0.8 dB for both polarizations within the desired 76 to 81 GHz frequency bandwidth. The maximum phase differences are less than 4 degree for port RHCP excitation and less than 2 degree for port LHCP excitation. The presented

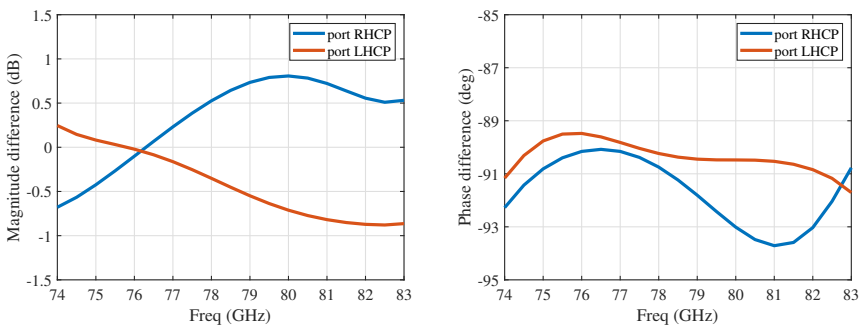

(a) **(b)**

Figure 3: (a) Magnitude difference of the orthogonal components when port RHCP ($|\mathbf{E_{R1}}| - |\mathbf{E_{R2}}|$) and port LHCP ($|\mathbf{E_{L1}}| - |\mathbf{E_{L2}}|$) are excited. (b) Phase difference of the orthogonal components when port RHCP ($phase(\mathbf{E_{R1}}) - phase(\mathbf{E_{R2}})$) and port LHCP ($phase(\mathbf{E_{L1}}) - phase(\mathbf{E_{L2}})$) are excited.

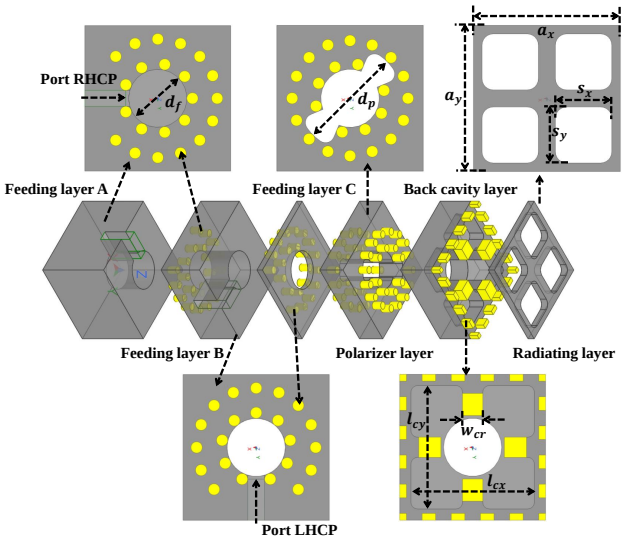

Figure 4: Multi-layer structure of the 2-by-2 unit cell

polarizer is able to realize high polarization performance at E-band.

3 Unit Cell Design Based on Gap Waveguide Technology

To realize a multi-layer planar array based on the double-grooved circular waveguide polarizer demonstrated in the previous section, a 2×2 unit cell using gap waveguide technology is proposed in this section.

The proposed unit cell is shown in Fig. 4. The design consists of 6 layers, including 3 layers for the feeding networks, one layer for the polarizer, one layer of back cavity and another layer of radiating grid. The size of the polarizer is challenging for array designs. The distance between the radiating elements need to be smaller than one wavelength in order to avoid grating lobes, thus a 1-to-4 back cavity is cascaded after the double-grooved polarizer with a radiating grid layer on top of it. The electric fields on top of the grid layer are illustrated in Fig. 5 and Fig. 6 over a duration of one period.

Periodic pins have been used for the non-galvanic connections between the layers. The dimensions of the pins have been carefully optimized to prevent the field from leaking through the gap between the layers as shown in Fig. 7a. The band gap is determined by plotting the dispersion diagram over the irreducible Brillouin zone (Γ-X-M-Γ) with periodic boundary conditions in x and y and parameter sweeps of phase$_x$ and phase$_y$. The dispersion diagram of the unit cell is shown in Fig. 7b. The band gap is from 40 to 160 GHz with air

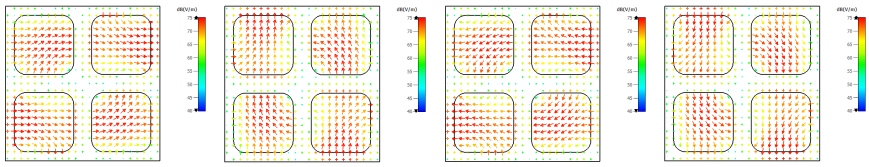

(a) $t = 0$ **(b)** $t = \frac{T}{4}$ **(c)** $t = \frac{T}{2}$ **(d)** $t = \frac{3*T}{4}$

Figure 5: Illustration of RHCP electric fields at 78 GHz on top of the grid layer over a duration of one period.

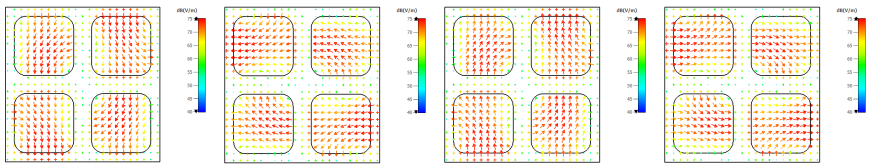

(a) $t = 0$ **(b)** $t = \frac{T}{4}$ **(c)** $t = \frac{T}{2}$ **(d)** $t = \frac{3*T}{4}$

Figure 6: Illustration of LHCP electric fields at 78 GHz on top of the grid layer over a duration of one period.

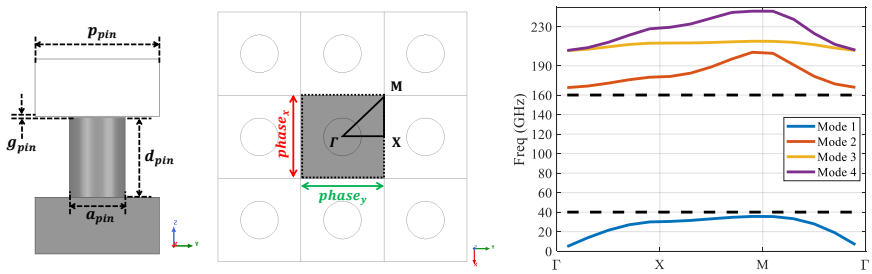

(a) **(b)**

Figure 7: Dispersion diagram (b) of the gap-waveguide pin texture (a).

gap of 15 μm. The large band gap is able to guarantee robustness of the interconnect. The substitution from metalized electric wall to periodic pins will not have significant impact on the rectangular waveguide excitations and polarizer. Thus, the previous study provides good approximations for the initial design and can be used as starting point for quick optimization with gap waveguide geometry.

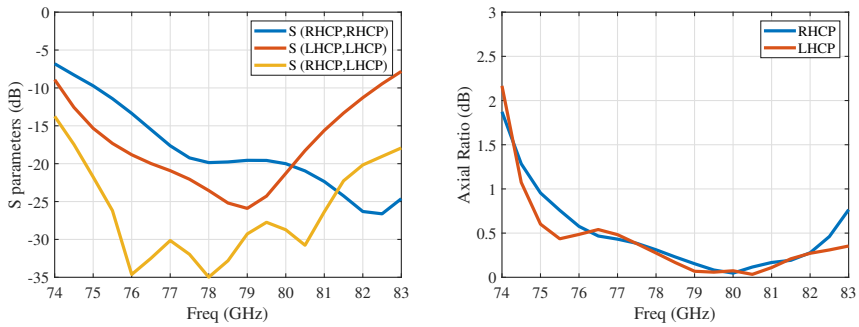

(a) (b)

Figure 8: Simulated (a) S parameters and (b) axial ratios of the unit cell.

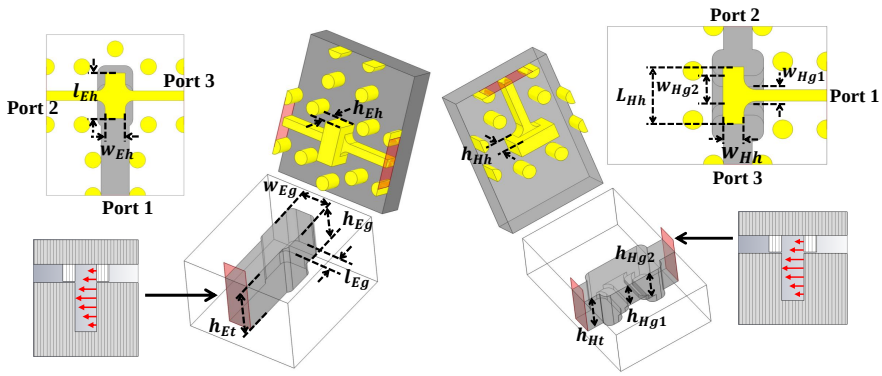

(a) (b)

Figure 9: Folded (a) E-plane T-junction and (b) H-plane T-junction based on gap waveguide.

The proposed unit cell is modeled and analyzed in ANSYS HFSS. The simulated S parameters and axial ratios are shown in Fig. 8. The reflection coefficients are better than -15 dB for both excitations and the isolation between the ports is around 30 dB from 76 to 81 GHz. The axial ratios are less than 0.5 dB for both polarizations within the frequency range. The proposed unit cell has promising radiating performance and can be used to implement the planar array.

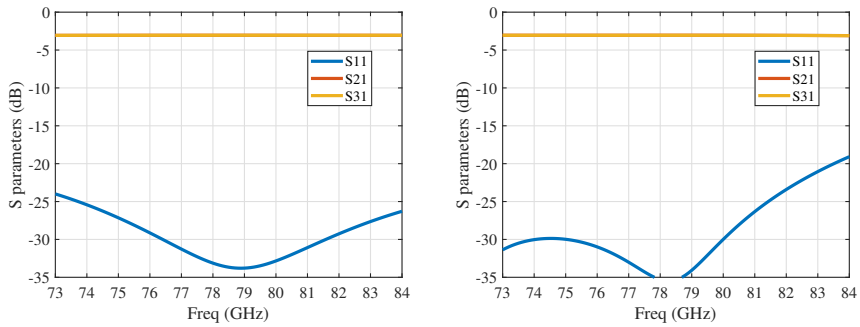

Figure 10: Simulated S parameters of the (a) E-plane T-junction and (b) H-plane T-junction power dividers.

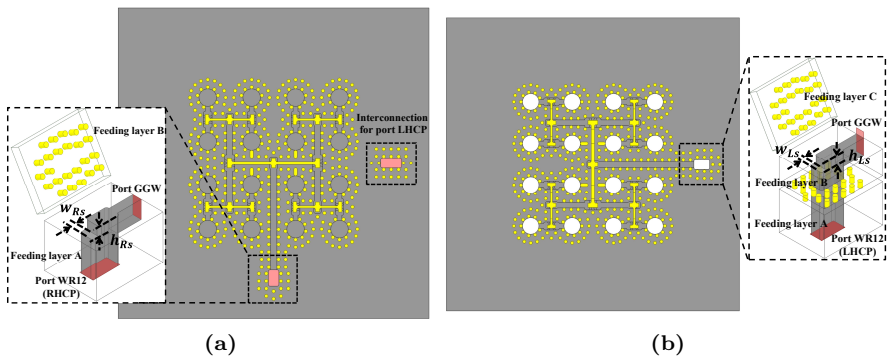

Figure 11: Corporate feeding networks for the two polarizations: (a) RHCP and (b) LHCP.

4 Array Design

To realize corporate feeding networks for the planar array, power dividers using E-plane and H-plane T-junctions based on gap waveguides are proposed in this section, as shown in Fig. 9. Horizontally polarized (HP) GGW and RGW have been utilized to implement the power dividers. Folded structures have been realized by putting 90° waveguide bends and T-junctions together. The E-plane T-junction realizes an equal power distribution from HP GGW to separated RGW lines, while the H-plane T-junction realizes a equal power

Table 1: Dimensions of designed array antenna

Parameter	value (mm)
Pin Texture	
Diameter of pin cylinder (a_{pin})	0.5
Height of pin cylinder (d_{pin})	0.7
Period of pin texture (p_{pin})	1.1
Gap of pin texture (g_{pin})	0.015
Unit Cell	
Diameter of the feeding circular waveguide (d_f)	2.59
Diameter of the grooved circular waveguide (d_p)	4.64
Length of unit cell in x and y (a_x=a_y)	6.5
Length of radiating slot in x and y (s_x=s_y)	2.49
Length of back cavity in x and y (l_{cx}=l_{cy})	5.5
Width of ridge inside the back cavity (w_{cr})	0.9
Power Dividers of the Feeding Networks	
Length of the ridge in E-T (l_{Eh})	1.41
Width of the ridge in E-T (w_{Eh})	0.62
Height of the ridge in E-T (h_{Eh})	0.90
Height of the groove in E-T (h_{Eg})	1.48
Width of the groove in E-T (w_{Eg})	1.1
Length of the groove in E-T (l_{Eg})	0.59
Height of the HP GGW in E-T (h_{Et})	1.99
Length of the ridge in H-T (l_{Hh})	1.51
Width of the ridge in H-T (w_{Hh})	0.52
Height of the ridge in H-T (h_{Hh})	0.93
Height of the groove 1 in H-T (h_{Hg1})	1.12
Width of the groove 1 in H-T (w_{Hg1})	0.34
Height of the groove 2 in H-T (h_{Hg2})	1.35
Width of the groove 2 in H-T (w_{Hg2})	1.03
Height of the HP GGW in H-T (h_{Et})	1.70
Input Transitions of the Feeding Networks	
Height of the step in RHCP input (h_{Rs})	1.00
Width of the step in RHCP input (w_{Rs})	0.70
Height of the step in LHCP input (h_{Ls})	1.04
Width of the step in LHCP input (w_{Ls})	0.63

distribution from RGW to separated HP GGW lines. Therefore, the power dividers are also transitions between HP GGW and RGW. The folded structure is suitable for cascading the power dividers, in the meantime, features compact properties. The simulated S parameters of the two power dividers are shown in Fig. 10. The reflection coefficients are better than -20 dB for both power dividers from 74 to 83 GHz.

The feeding networks for the two polarizations have been implemented on the basis of the power dividers, as shown in Fig.11. To make the input ports located at the bottom of the array, vertical transitions from WR12 to HP GGW are proposed as depicted in details in Fig. 11. Please notice that for LHCP, the transition need to pass through feeding layer A. Interconnections utilizing periodic pins between feeding layer A and B are able to guarantee no fields leaking through the gap and feature excellent transmission performance. The simulated results of the vertical transitions are shown in Fig. 12. The reflection coefficients

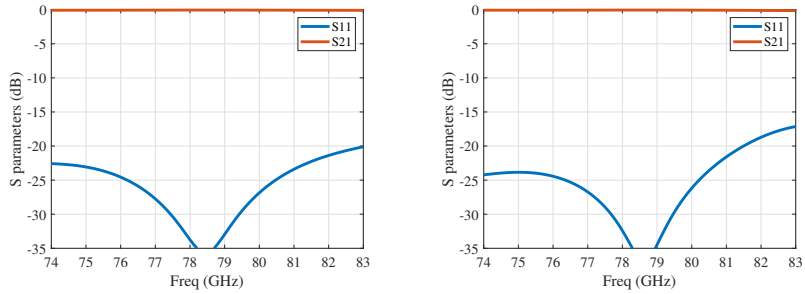

Figure 12: Simulated S parameters of the vertical transitions between WR12 and HP GGW: (a) for RHCP and (b) for LHCP.

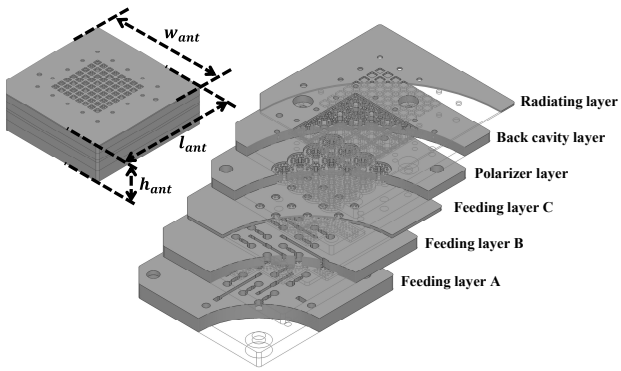

Figure 13: Multi-layer structure of the dual-circularly polarized planar array.

are better than -20 dB from 76 to 81 GHz for both vertical transitions.

The entire planar array is shown in. Fig. 13 and depicted in details in Fig. 14. The planar array has dimensions of 56 mm × 56 mm × 17 mm with 8×8 elements and standard WR12 waveguide ports at the bottom. The simulated axial ratios of the array are less than 1 dB within 3-dB beam width over the space for both polarizations from 76 to 81 GHz, as shown in Fig. 15 specifically at 76.5 and 78.5 GHz. The performance of the array antenna has been verified by measurements and will be discussed in the next section.

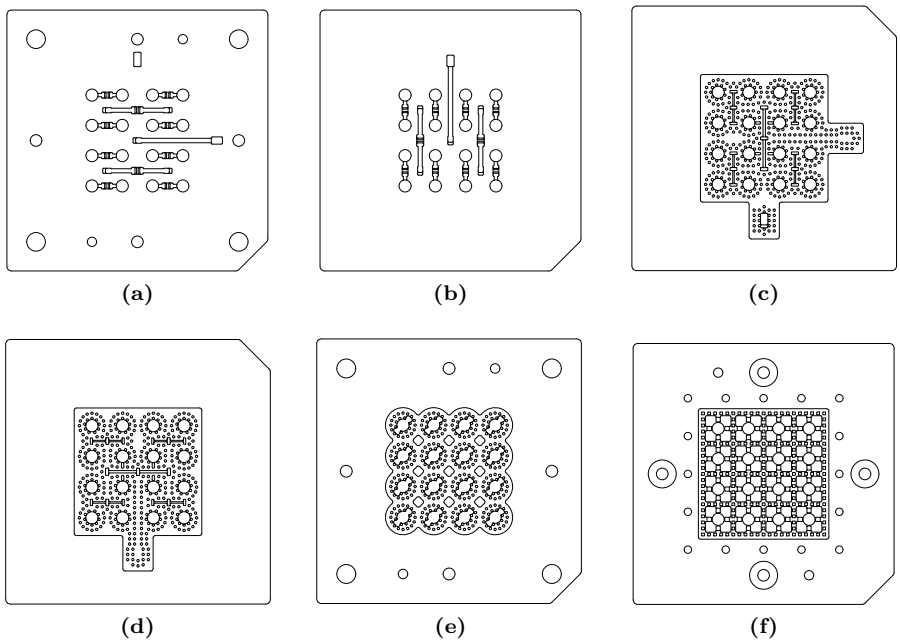

Figure 14: Views of different layers: (a) top view of feeding layer A; (b) top view of feeding layer B; (c) bottom view of feeding layer B; (d) bottom view of feeding layer C; (e) top view of polarizer layer; (f) top view of back cavity layer.

5 Measurement

The proposed antenna array has been manufactured by CNC machining in brass with 1 μm of gold plating. Photographs of the prototype are shown in Fig. 16. Metallic screws of different sizes and alignment pins have been used to assemble the layers as shown in Fig. 16. Two-ports S-parameters of the prototype have been measured by Keysight N5242A PNA-X and VDI WR-12 extenders, as shown in Fig. 17. The measured and simulated results are shown in Fig. 18. The measured results agree well with the simulated results and have shown that reflection coefficients are better than -10 dB for both circular polarizations from 76 to 81 GHz. The measured isolation between the input ports is larger than 25 dB from 76 to 81 GHz.

The far field properties of the planar array have been measured in an anechoic chamber in far-field setup as shown in Fig. 19. In order to measure the radiation patterns, standard circularly polarized conical horns have been used as receiving antennas while the planar array is placed at the positioner as transmitting antenna, as depicted in Fig. 19. Standard

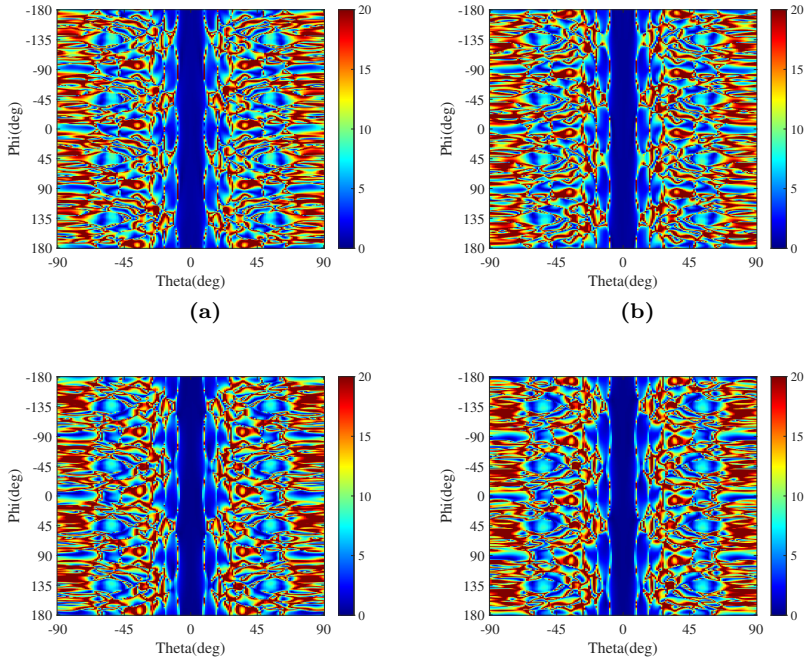

Figure 15: Simulated axial ratios of the array antenna at 76.5 GHz: (a) RHCP, (b) LHCP, and 78.5 GHz: (c) RHCP, (d) LHCP.

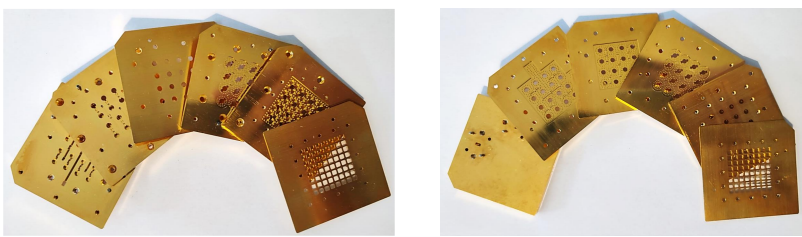

Figure 16: Top (a) and bottom (b) view of the manufactured prototype.

Figure 17: S-parameters measurement setup for the fabricated planar array.

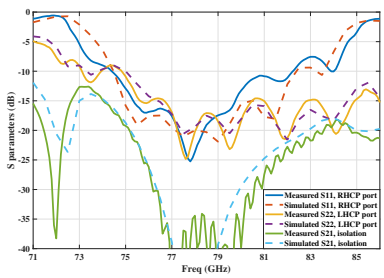

Figure 18: Measured and simulated results of the proposed planar array.

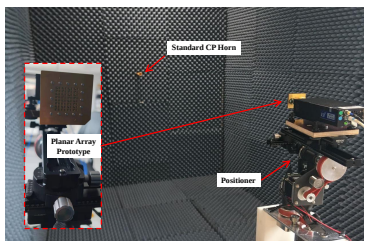

Figure 19: Far field measurement setup for the fabricated planar array.

CP antennas based measurement is capable of evaluating the far field properties of the antenna, in the meantime, more convenient and faster compared with LP antennas based

measurement. The standard CP conical horn with polarizers used in this work is from Millimeter Wave Products Inc. with axial ratios less than 1 dB over 76 to 87 GHz. Therefore, the accuracy of the measurement was guaranteed. The normalized realized gain patterns of both polarizations in $\phi = 0°$ (x-z) and $\phi = 90°$ (y-z) cut planes are shown in Fig. 20.

The realized gains at boresight direction over frequencies have been measured by replacing the planar array with a LP standard gain horn (SGH) antenna as the reference and considering 3 dB loss of polarization mismatch. The measured results are consistent with the simulation and show that the planar array has more than 24 dBi gain from 76 to 81 GHz for both polarizations, as shown in Fig. 21.

The axial ratios of both circular polarizations at boresight direction over frequencies are obtained from the measured co-polar and cross-polar patterns by:

$$AR(dB) = 20 * log_{10}(\frac{10^{XPD(dB)}/20 + 1}{10^{XPD(dB)}/20 - 1}) \tag{D.4}$$

where XPD is cross polar level in decibel. The results are shown in Fig. 22. The axial ratios are less than 1.5 dB for both circular polarizations from 76 to 81 GHz and show good agreement with the simulated results. Compared with previously published works, the proposed array antenna has good radiating performance in terms of axial ratio and efficiency as shown in Table 2.

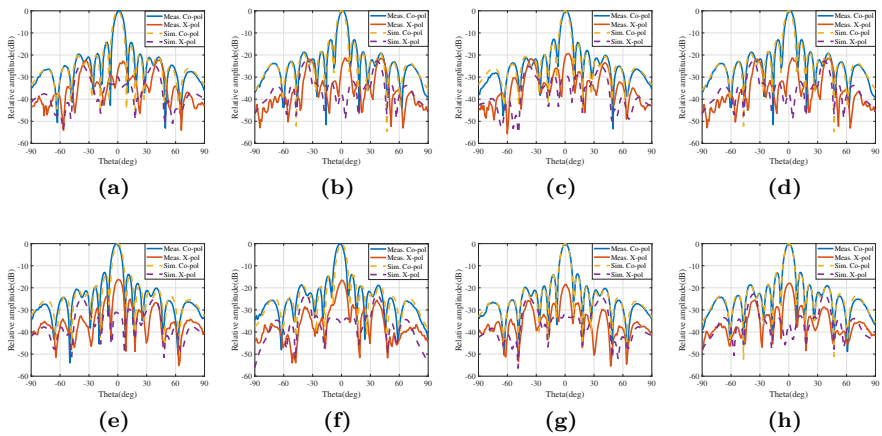

Figure 20: Simulated and measured realized gain patterns of the planar array: (a) RHCP in x-z at 76.5 GHz; (b) RHCP in x-z at 78.5 GHz; (c) RHCP in y-z at 76.5 GHz; (d) RHCP in y-z at 78.5 GHz; (e) LHCP in x-z at 76.5 GHz; (f) LHCP in x-z at 78.5 GHz; (g) LHCP in y-z at 76.5 GHz; (h) LHCP in y-z at 78.5 GHz.

Table 2: Comparison Between the Proposed Dual-Circularly Polarized Array with Previously Published Works

Dual CP Array	Layout	Center Freq. (GHz)	Technology	Gain	Aperture Efficiency	Radiation Efficiency	Port-Isolation	S11 BW (<-10 dB)	AR BW (<1.5 dB)
[25]	8×8	30	GW	27 dBi	-	75% ∼ 80%	-	≈ 6.7%	≈ 3.5%
[27]	1×8	78.5	GW	14.8 dBi	-	75% ∼ 85%	> 18.6 dB	10.9%	≈ 6%
[28]	16×16	30	RW	31 dBi	60% ∼ 90%	-	> 20 dB	16.7%	≈ 12%
[29]	8×8	60	SIW	25.8 dBi	80% ∼ 90% (sim.)	≈ 70% (sim.)	> 14 dB	23%	12%
[30]	15×15	94	SIW	25.5 dBi	-	≈ 57.5%	≈ 20 dB	≈ 1%	≈ 1%
This work	8×8	78.5	GW	24 dBi	60% ∼ 90%	70% ∼ 80%	> 25 dB	10%	6.5%

Note: Gap Waveguide (GW), Rectangular Waveguide (RW), Substrate Integrated Waveguide (SIW).

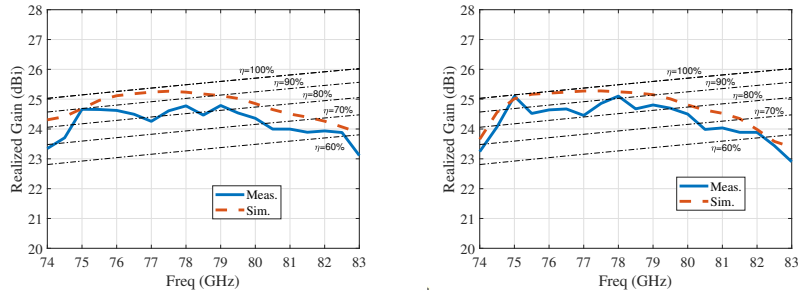

Figure 21: Simulated and measured realized gains over frequency of the planar array: (a) RHCP; (b) LHCP with aperture efficiency η.

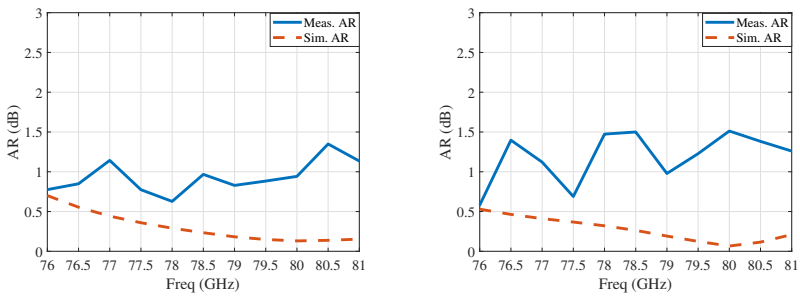

Figure 22: Simulated and derived axial ratios over frequency of the planar array: (a) RHCP; (b) LHCP.

6 Conclusion

In this work, a dual-circularly polarized array antenna based on gap waveguide technology operating at E band has been proposed. The array antenna uses double-grooved circular waveguide polarizer that has two annulus grooves placed at 45° and 135° offset from both excitation ports respectively. The operating principles of the polarizer have been presented. Multi-layer design using gap waveguide has been implemented based on the polarizer. A 2×2 unit cell has been proposed firstly and optimized for input matching and axial ratios.

Then, a 8×8 planar array has been realized. The antenna consists of six layers, including three layers for the feeding networks, one layer for the polarizer, one layer of back cavity and another layer of radiating grid. Corporate feeding networks that using folded E-plane T-junctions and H-plane T-junctions have been proposed. The antenna has been fabricated and verified by measurements. The measured results of S-parameters agree well with the simulation and show that reflection coefficients are better than -10 dB for both circular polarizations from 76 to 81 GHz. The measured isolation between the input ports is larger than 25 dB from 76 to 81 GHz. The far-field measurements show that the antenna has realized gain larger than 24 dBi and axial ratios less than 1.5 dB from 76 to 81 GHz.

Acknowledgment

The authors would like to thank Carlo Bencivenni from Gapwaves AB for his support and discussion during this work. Special thanks to Yan Yu from MC2, Chalmers, Hanna Karlsson, Julius Petersson from Gapwaves AB and Zhaorui Zang from E2, Chalmers, for their help with measurements. This work is supported by Swedish Strategic Vehicle Research and Innovation FFI grant 2018-02707.

References

[1] J. Steinbaeck, C. Steger, G. Holweg, and N. Druml, "Next generation radar sensors in automotive sensor fusion systems," in *2017 Sensor Data Fusion: Trends, Solutions, Applications (SDF)*, 2017, pp. 1–6.

[2] G. F. Hamberger, S. Späth, U. Siart, and T. F. Eibert, "A mixed circular/linear dual-polarized phased array concept for automotive radar-planar antenna designs and system evaluation at 78 GHz," *IEEE Transactions on Antennas and Propagation*, vol. 67, no. 3, pp. 1562–1572, 2019.

[3] W. Menzel and A. Moebius, "Antenna concepts for millimeter-wave automotive radar sensors," *Proceedings of the IEEE*, vol. 100, no. 7, pp. 2372–2379, 2012.

[4] T. Visentin, "Polarimetric radar for automotive applications," Ph.D. dissertation, Karlsruher Institut für Technologie (KIT), 2019.

[5] S. Trummer, G. F. Hamberger, U. Siart, and T. F. Eibert, "A polarimetrie 76–79 GHz radar-frontend for target classification in automotive use," in *2016 46th European Microwave Conference (EuMC)*, 2016, pp. 1493–1496.

[6] E. Garcia-Marin, J. L. Masa-Campos, P. Sanchez-Olivares, and J. A. Ruiz-Cruz, "Bow-tie-shaped radiating element for single and dual circular polarization," *IEEE Transactions on Antennas and Propagation*, vol. 68, no. 2, pp. 754–764, 2020.

[7] X. Cheng, Z. Liu, Y. Yao, T. Yu, J. Yu, and X. Chen, "Metasurface concept for mm-wave wideband circularly polarized horns design," *IEEE Transactions on Antennas and Propagation*, vol. 69, no. 8, pp. 4313–4322, 2021.

[8] N. Yoneda, R. Miyazaki, I. Matsumura, and M. Yamato, "A design of novel grooved circular waveguide polarizers," *IEEE Transactions on Microwave Theory and Techniques*, vol. 48, no. 12, pp. 2446–2452, 2000.

[9] N. Luo, X. Yu, G. Mishra, and S. K. Sharma, "A millimeter-wave (V-band) dual-circular-polarized horn antenna based on an inbuilt monogroove polarizer," *IEEE Antennas and Wireless Propagation Letters*, vol. 19, no. 11, pp. 1933–1937, 2020.

[10] I. Agnihotri and S. K. Sharma, "Design of a compact 3-D metal printed Ka-band waveguide polarizer," *IEEE Antennas and Wireless Propagation Letters*, vol. 18, no. 12, pp. 2726–2730, 2019.

[11] C. Shu, S. Hu, X. Cheng, *et al.*, "Wideband dual-circular-polarization antenna with high isolation for millimeter-wave wireless communications," *IEEE Transactions on Antennas and Propagation*, vol. 70, no. 3, pp. 1750–1763, 2022.

[12] U. Balaji and Vahldieck, "Radial mode matching analysis of ridged circular waveguides," *IEEE Transactions on Microwave Theory and Techniques*, vol. 44, no. 7, pp. 1183–1186, 1996.

[13] U. Balaji and R. Vahldieck, "Radial mode matching analysis of ridged circular waveguide," in *Proceedings of 1995 IEEE MTT-S International Microwave Symposium*, 1995, 637–640 vol.2.

[14] C. Shu, J. Wang, S. Hu, *et al.*, "A wideband dual-circular-polarization horn antenna for mmWave wireless communications," *IEEE Antennas and Wireless Propagation Letters*, vol. 18, no. 9, pp. 1726–1730, 2019.

[15] C. Kumar, V. V. Srinivasan, V. K. Lakshmeesha, and S. Pal, "Novel dual circularly polarized radiating element for spherical phased-array application," *IEEE Antennas and Wireless Propagation Letters*, vol. 8, pp. 826–829, 2009.

[16] A. Vosoogh, A. Haddadi, A. U. Zaman, J. Yang, H. Zirath, and A. A. Kishk, "*W* -band low-profile monopulse slot array antenna based on gap waveguide corporate-feed network," *IEEE Transactions on Antennas and Propagation*, vol. 66, no. 12, pp. 6997–7009, 2018.

[17] J. Liu, A. Vosoogh, A. U. Zaman, and J. Yang, "A slot array antenna with single-layered corporate-feed based on ridge gap waveguide in the 60 GHz band," *IEEE Transactions on Antennas and Propagation*, vol. 67, no. 3, pp. 1650–1658, 2019.

[18] A. Farahbakhsh, D. Zarifi, and A. U. Zaman, "60-GHz groove gap waveguide based wideband *H* -plane power dividers and transitions: For use in high-gain slot array antenna," *IEEE Transactions on Microwave Theory and Techniques*, vol. 65, no. 11, pp. 4111–4121, 2017.

[19] E. Rajo-Iglesias, Z. Sipus, and A. U. Zaman, "Gap waveguide technology," in *Surface electromagnetics : with applications in antenna, microwave, and optical engineering*, F. Yang and Y. Rahmat-Samii, Eds., Cambridge University Press, 2019, pp. 198–230.

[20] E. Rajo-Iglesias, M. Ferrando-Rocher, and A. U. Zaman, "Gap waveguide technology for millimeter-wave antenna systems," *IEEE Communications Magazine*, vol. 56, no. 7, pp. 14–20, 2018.

[21] A. Vosoogh, P.-S. Kildal, and V. Vassilev, "A multi-layer gap waveguide array antenna suitable for manufactured by die-sink EDM," in *2016 10th European Conference on Antennas and Propagation (EuCAP)*, 2016, pp. 1–4.

[22] Á. Palomares-Caballero, A. Alex-Amor, J. Valenzuela-Valdés, and P. Padilla, "Millimeter-wave 3-D-printed antenna array based on gap-waveguide technology and split E-plane waveguide," *IEEE Transactions on Antennas and Propagation*, vol. 69, no. 1, pp. 164–172, 2021.

[23] S. Farjana, M. Ghaderi, A. U. Zaman, *et al.*, "Realizing a 140 GHz gap waveguide–based array antenna by low-cost injection molding and micromachining," *Journal of Infrared, Millimeter, and Terahertz Waves*, vol. 42, no. 8, pp. 893–914, 2021, ISSN: 1866-6906.

[24] S. Farjana, M. Ghaderi, A. U. Zaman, S. Rahiminejad, P. Lundgren, and P. Enoksson, "Low-loss gap waveguide transmission line and transitions at 220–320 GHz using dry film micromachining," *IEEE Transactions on Components, Packaging and Manufacturing Technology*, vol. 11, no. 11, pp. 2012–2021, 2021.

[25] M. Ferrando-Rocher, J. I. Herranz-Herruzo, A. Valero-Nogueira, and B. Bernardo-Clemente, "Dual circularly polarized aperture array antenna in gap waveguide for high-efficiency Ka-band satellite communications," *IEEE Open Journal of Antennas and Propagation*, vol. 1, pp. 283–289, 2020.

[26] M. Ferrando-Rocher, J. I. Herranz-Herruzo, A. Valero-Nogueira, B. Bernardo-Clemente, A. U. Zaman, and J. Yang, "8×8 Ka -band dual-polarized array antenna based on gap waveguide technology," *IEEE Transactions on Antennas and Propagation*, vol. 67, no. 7, pp. 4579–4588, 2019.

[27] Z. Zang, A. U. Zaman, and J. Yang, "Single layer dual circularly polarized antenna array based on ridge gap waveguide for 77 GHz automotive radar," *IEEE Transactions on Antennas and Propagation*, pp. 1–1, 2022, early access.

[28] J. Wu, Y. J. Cheng, H. B. Wang, Y. C. Zhong, D. Ma, and Y. Fan, "A wideband dual circularly polarized full-corporate waveguide array antenna fed by triple-resonant cavities," *IEEE Transactions on Antennas and Propagation*, vol. 65, no. 4, pp. 2135–2139, 2017.

[29] Y. Zhao and K.-M. Luk, "Dual circular-polarized SIW-fed high-gain scalable antenna array for 60 GHz applications," *IEEE Transactions on Antennas and Propagation*, vol. 66, no. 3, pp. 1288–1298, 2018.

[30] Y. J. Cheng, J. Wang, and X. L. Liu, "94 GHz substrate integrated waveguide dual-circular-polarization shared-aperture parallel-plate long-slot array antenna with low sidelobe level," *IEEE Transactions on Antennas and Propagation*, vol. 65, no. 11, pp. 5855–5861, 2017.